Doctoral Dissertation (Censored)

博士論文（要約）

Observational characterization of protoplanetary disks, exo-rings, and Earth-twins in exoplanetary systems

(太陽系外惑星系における原始惑星系円盤、

系外惑星リング、第二の地球の観測的特徴づけ)

A Dissertation Submitted for the Degree of Doctor of
Philosophy

December 2019

令和元年 12 月 博士（理学）申請

Department of Physics, Graduate School of Science

The University of Tokyo

東京大学大学院理学系研究科物理学専攻

Masataka Aizawa

逢澤 正嵩

Abstract

Since the discovery of the first exoplanet around a Sun-like star in 1995, our understanding of planetary formation has drastically advanced, and, currently, there have been over 4000 discovered exoplanets. Most of the discovered planetary systems are significantly different from the planets in the Solar System implying the diversity of the extrasolar world as well as current observational limitations.

In this thesis, we attempt to tackle three specific themes related to the planetary formation and evolution; systematic search for exorings, observational quest for alignment among proto-planetary disks, and global mapping of an Earth analog.

In the first theme, we perform a systematic search for exoplanetary rings using the Kepler data. Signatures of transiting ringed planets are slightly different from ringless planets, and the difference between them can be exploited to search for planetary rings. Using a fast and precise algorithm for a transiting ringed planet, we search for exoplanetary rings among 168 Kepler planets, whose light curves possibly allow the detection of Saturn-like rings with the size of twice the planetary radius. We apply ringed and ringless models to phase folded light curves and compare the fitting outcomes to identify the signatures of rings. Firstly, we find 29 tentative systems, where fitting by ringed models is statistically favored compared with the ringless models. Although we examine these possible signatures in detail, we are not able to find convincing evidence of rings. In turn, we put constraints on possible planetary rings using the null results. Most of our targets have close-in orbits, so the planes of planetary rings are likely to be on the orbital planes of planets due to the tidal alignment. Based on this assumption, we conclude that the occurrence rate of rings larger than twice the planetary radius is less than 15 %. Although the majority of targets in this study are short-period planets, the null detection puts the quantitative constraint on origins, formation and evolution of planetary rings.

The second theme is to search for alignment among proto-planetary disks in nearby five star-forming regions using interferometric observations by ALMA. We analyze the directions of disks in five star-forming regions, and we find that the disk orientations projected in the sky are likely to be random in four regions out of five, which is consistent with a theory that angular momentum is generated by turbulent motions in molecular clouds. At the same time, we find the possible alignment in the Lupus III at the statistical significance of 2σ, and it might imply other mechanisms beyond turbulent motions for generating angular momentum. For the robust discussion in the Lupus region, we compare different observations and methods including sparse modeling for estimating disk's axes, and we find that all of them show consistent estimations of disk orientations. On the

other hand, we find the alignment in Orion Nebula Cluster, but it turns out to be more likely a false positive, which is produced by systematic noises during an observation.

Finally, we present a new methodology for global mapping of an Earth analog in future direct imaging missions. In the study, we introduce new regularization terms of L1-norm and Total Squared Variation to recover the two dimensional map from scattered light curves of directly imaged planets. For quantifying the potential improvement by the new method, we compare the recovered maps with the ground truth map of the Earth by varying regularization parameters. Using both simulated and real data of scattered light of the Earth for 1 or 2 years, we find that particular sets of the regularization parameters in the new method give more correct 2d map than the conventional method. In addition, we also explore the feasibility of global mapping by considering limited observational duration and noise associated with directly imaging observations for an Earth analog at distance of 10 pc. We find that observations for only the first day of the month in 2 years can roughly recover the surface distribution of the Earth. Our study shows the importance of choices of regularization terms in global mapping, and demonstrates the feasibility of recovering the surface inhomogeneity of an Earth analog in future direct imaging missions such as HabEx and LUVOIR.

In this thesis, we present methods for characterizing exoplanetary counterparts of objects in the Solar System, Saturn and Earth analogs. We also explore the applicability of sparse modeling by exploiting interferometric data and light curves of directly imaged planets. These studies open new possibility of the sparse method in astronomy, and the further investigation is rewarding. In addition, we also attempt to provide unconventional ways to unveil the architecture of planetary systems; we present the potential methods for constraining planetary spins, and explore global alignment among proto-planetary disks beyond one particular planetary system. These works would contribute to understanding the origins and formation of planetary systems including the Solar System, and the methodologies presented in this thesis can be naturally applied to the current and future observations.

Contents

Chapter 1

Introduction

Since the first discovery of the exoplanet in 1995, a bunch of detection of exoplanets have been identified, and our understanding of planetary formation has been drastically improved. Having said so, the whole exoplanetary architectures are still unexplored due to the observational limitations of current technology, and the detection of Solar-System-like systems is still observationally challenging. Additionally, it is still difficult to characterize counterparts of detailed structures in the Solar Systems, which include rings, moons, comets, and life. Their detection is challenging but indispensable for building the inclusive planetary formation theory, which still largely depends on observational facts of the Solar System.

Since all of giant planets commonly possess planetary rings, we naturally expect them to exist in exoplanetary systems. Previously, Barnes & Fortney (2004) demonstrated that signatures of exoplanetary rings are detectable around exoplanets by the current instrument e.g. Kepler satellite, which has successfully discovered a lot of transiting planets. Later, Aizawa et al. (2017) presented a systematic search for rings around long-period Kepler planets and candidates, which potentially hold icy rings like Saturn, and they discovered one possible candidate of the ring. However, the majority of the Kepler planets have been still unexplored despite the capability of the Kepler satellite. Therefore, we further search for possible exoplanetary rings around the Kepler planets in Chapter 3.

Planet formation is the consequence of the star formation. Since molecular clouds have angular momentum, their collapse inevitable leads to formation of rotationally supported structures including proto-planetary disks, and they eventually evolve to planetary systems. Henceforth, the understanding of the star formation is also important for revealing the nature of the planet formation. One of the key concepts in the planetary formation is the angular momentum of planets, and their origin date back to the cores and molecular clouds at very early phases of star formation. Generally, the turbulent motion within clouds is recognized as the source of angular momentums (e.g. Goodman et al., 1993), and this hypothesis naturally predicts the random orientations of directions of angular momentums of cores, disks, and stars. There are a few attempts to find the alignment among stellar spins (e.g. Corsaro et al., 2017), and the further exploration of the alignment among stellar angular momentum is very encouraging.

Stellar spins can be significantly perturbed during the course of the stellar evolution, and their measurement is also technically challenging. On the other hand, the proto-planetary disks reside in the middle of star and planet formation, and they are likely to preserve the information on angular momentum transfer. Currently, there are several systematic campaigns for detecting planetary disks in nearby star-forming regions by the Atacama Large Millimeter/submillimeter Array (ALMA) (Ansdell et al., 2016; Barenfeld et al., 2016; Eisner et al., 2018; Cieza et al., 2019), so we can exploit their geometry to discuss the alignment. We explore this possibility in Chapter 4.

On the other hand, faced with the big data (e.g. ALMA, Kepler), the data analysis methods and their applications to the astronomy have been developed rapidly, and one of such techniques is the sparse modeling (e.g. Honma et al., 2014; Ikeda et al., 2016; Akiyama et al., 2017b,a; Kuramochi et al., 2018; Event Horizon Telescope Collaboration et al., 2019). This technique can be used to search for optimal solutions, and it is significantly useful especially when the possible solutions have a lot of zero values, i.e. sparsity. The practical example of this technique is an image reconstruction of a shadow of a black hole from interferometric observations in global networks (Event Horizon Telescope Collaboration et al., 2019).

Since the application of the sparse modeling in astronomy has just started, we investigate the possibility of the method further. Firstly, we exploit the technique to obtain the highly resolved images of proto-planetary disks to check whether it gives the precise estimations on the disk's axes. We find that the sparse modeling does not change the significance of the alignment as discussed in Chapter 4. To investigate the possibility of the sparse modeling further, we also apply the technique to inverse modeling of global mapping of an Earth analog in the future direct imaging observations. In this problem, the surface inhomogeneity of planetary surfaces is retrieved from their reflected light curves (Ford et al., 2001), and the reconstruction is generally ill-posed, so it would require the regularization terms (Kawahara & Fujii, 2011). Instead of adopting the conventional regularization, we introduce the sparse modeling for global mapping by exploiting the particular feature that the ocean has almost zero albedo. In this way, we demonstrate the potential of the sparse modeling for global mapping in Chapter 5.

Throughout the thesis, we also attempt to shed new light on the architecture of exo-planetary systems. In the Solar System, the Sun's rotation axis is well aligned with the planetary orbital axes, but this is not the case for exoplanetary systems, some of which show large misalignment between them. Such misalignment can be unique information on the dynamical evolution of the planetary systems, and it has been extensively studied. Complementary to the misalignment between stellar axes and planetary orbital axes, one can also exploit a obliquity of planetary spin and its correlation with other angles. Although the detection of the planetary spin is currently challenging, it can be measured through the characterization of planetary rings as presented in Chapter 3 and reflectional light in direct imaging in Chapter 5. Beyond the alignment within one particular system, global correlations among planetary systems would also give unique information on the overall picture of the stellar and planetary formation. Such correlations can be indirectly studied by investigating the disk-disk alignment, which has close a relation to the alignment among planetary systems, and it is discussed in Chapter 4.

This thesis addresses observational characterizations of stellar and planetary systems in unconventional approaches. We explore the possibility of the sparse modeling in Chapter 4 and Chapter 5 by considering interferometric observations of proto-planetary disks and direct imaging of exoplanets. We also give methodologies for identifying Solar-System counterparts, specifically exorings in Chapter 3 and exoplanetary surfaces in Chapter 5. Furthermore, the methodologies presented in this thesis are potentially useful for constraining planetary spins and global correlations among planetary systems, and they are complementary to previous studies in the context of discussion on the architecture of planetary systems.

The rest of this thesis is organized as follows. In Chapter 2, we summarize the current observational knowledge on exoplanetary systems, and give the foundation for the studies in this thesis. In Chapter 3, we present the intensive search for exoplanetary rings using the Kepler data, and give the constraint on ring formation in exoplanetary systems. In Chapter 4, we discuss the disk-disk alignment using interferometric observations by ALMA, and, in doing so, we also attempt to exploit the sparse modeling in measuring the disk's axes. In Chapter 5, we develop the new methodology to retrieve two dimensional surface map of Earth analogs, and discusses the feasibility of global mapping in the future direct imaging observations. Finally, in Chapter 6, we summarize the thesis and give the future prospects.

Chapter 2

Review on Observational Characterization of Exoplanetary Systems

Since the discovery of the first exoplanetary system, our understanding of planetary formation has been drastically changed. The majority of observed exoplanets are clearly different from the Solar System, implying that previous theories of planetary systems need to be revised. Indeed, there have been intensive studies to build up consistent scenarios for the planet formation. Beyond the mere detection, the characterization of planetary systems is a key for the further understanding of the planet formation: constraints on density, chemical compositions, and atmosphere of exoplanets. Furthermore, identifications of exoplanetary structures including rings, moons, and even planetary surface structures (e.g. land, ocean) are complementary to the detection of planets themselves, providing clues toward the consistent picture of the planet formation.

The exoplanetary systems are supposed to be formed out of molecular clouds, and understanding of the star formation processes in the clouds is very important for the planet formation as well. However, it is still challenging to connect the clouds to the planetary scales due to the complexity in physical processes involved gravity, fragmentation, rotation, magnetic fields, cooling or heating, radiation, and turbulent motion. One of the key concepts, which link the small- and the large-scale of star formation, is alignment among stellar angular momentum. Recent observations (e.g. Kepler, ALMA) allow the quantitative discussion of the alignment, so the further exploration is rewarding.

This chapter briefly reviews our current understanding of exoplanetary systems, and is organized as follows. Section 2.1 summarizes the current understanding of exoplanetary systems from observations. Section 2.2 discusses observational characterizations of moons, rings, and planetary surfaces in exoplanetary systems. Section 2.3 summarizes angular momentum evolution of stellar systems, and possible implications of stellar alignment for origins of stellar angular momentum. In the last section, we present the summary of this chapter.

2.1 Observed properties of Exoplanetary Systems

The first exoplanetary system was discovered in 1992 by pulsar-timing method, which indirectly identifies the planetary signatures via precise measurements of pulsar signals (Wolszczan & Frail, 1992). The host star in this system is a pulsar PSR B1257+12, and the discovery poses a question to the formation mechanism. Later, the first exoplanetary system around a main-sequence star, 51 Pegasi, was discovered by Mayor & Queloz (1995) via the radial velocity method, which probes the small wobble of stellar motions exploiting the Doppler shift. The planetary mass was estimated to be comparable to Jupiter mass, and its orbital period is 4.23 days. This Jupiter sized planet with the extremely short orbital period is dubbed as a "Hot Jupiter", and it challenges the planetary formation theory, which assumed that giant planets form only far away form from the central star.

The subsequent observations have inflated the number of detected exoplanetary systems, and there have been the detection of over 4000 confirmed planets as of December in 2019 (http://www.exoplanet.eu/catalog/). Most of the planets have been detected via radial velocity and transit methods, which are complementary to each other. The former method probes the modified planetary mass $M_\mathrm{p} \sin i$, where M_p is the planetary mass, and i is the orbital inclination that is defined as the line-sight angle of the orbital axis. The latter transit method indirectly identifies planets using the dimming of a central due to a planet, and it presents a relative size of the planets to stars.

In addition to the transit and radial velocity methods, there are several different methods for detecting planets. Direct-imaging method is one of techniques for detecting the planetary light itself by suppressing the stellar light. Due to the nature of the technique, the method is potentially sensitive to distant planets compared with the other methods. The current technology (e.g. Gemini Planet Imager, Macintosh et al. (2014)) is still beyond the reach of cold planets in the Solar System because of the very low contrast of flux expected for such planets; 10^{-9} for Jupiter and 10^{-10} for Earth. Therefore, only young, massive and hot exoplanets have been detected by the method, and these planets give direct information on how planets formed at the first place.

Astrometry searches for a slight displacement of a stellar position, which is caused by an orbital motion of a planetary system. The method is sensitive to distant planets, which give large stellar displacements in the observations. However, the distant planets have long orbital periods, so it requires the large baseline for the observation. Currently, there are not so many planets detected by dastrometry, but the Gaia mission, which is observing the full sky for five years, is expected to yield tens of thousands planets in the future (Perryman et al., 2014).

Microlensing observations are also sensitive to distant planets. It exploits the planetary microlensing, which causes the brighting with the relatively short time-scale from hours to days. The sensitivity of microlensing is independent on planetary temperature, so it can yield the detection of cold planets typically around the snow lines. Suzuki et al. (2016) statistically analyzed the MOA-II microlensing survey for fix years, and they found that the function for mass-ratio q is not described by a single power law, but it has a break at $q \simeq 10^{-4}$, which corresponds to $20 M_\oplus$ for the median stellar mass of $0.6 M_\odot$ in the survey. The results show that the cold-Neptune like planets are possibly

most common type of planets beyond the snowline. This technique is unique because it is sensitive to free-floating planets, which are unbounded to any stellar objects. The estimated frequency of Jupiter-sized free-floating or wide-orbit planets was estimated to be ~ 1 per one pre-main sequence star (Sumi et al., 2011), and later revised as ~ 0.25 (Mróz et al., 2017). Free-floating planets are considered to be formed by the ejection from planetary systems via dynamical scattering.

As a result of the numerous observations, we are gradually understanding the planetary architectures in a statistical manner. Figure 2.1 shows planetary orbital periods and planetary masses, and Figure 2.2 shows planetary radii. The blue points in the figures represent the Solar System, which is distant from majority of observed systems. This demonstrates the diversity in extrasolar worlds as well as the observational limitation of the current technology.

There are several distinct types of planets in the exoplanetary systems. One notable class is "Hot Jupiter" that has the Jupiter-sized radius or mass orbiting in a few to tens of days. The existence of Hot Jupiters directly requires the improvement in theories, because standard planet formation scenarios including core accretion and gravitational instability naturally expect the formation of cold planets. They are also dynamically important for the stability of planetary systems when they migrate from outer part of orbits. Currently, the origins of Hot Jupiters are still unknown. Possible scenarios include the in-situ formation, gas disks migration from outer orbit, high-eccentricity tidal migration with Lidov-Kozai mechanisms, and/or planet-planet scattering (Dawson & Johnson (2018) and references therein). These formation path can be tested by using the observational features, including eccentricity distribution, obliquity of planetary orbit, radius inflation, semi-major axis distribution, the relation between stellar age and planetary parameters, and planetary atmosphere. Each of evidence can be explained by at least one path, but the single origin cannot account for every observational evidence (Dawson & Johnson, 2018).

Another new class of planets is close-in "Super-Earth" or "Mini Neptune", which are slightly larger than the Earth and slightly smaller than the Neptune, respectively. The Kepler satellite revealed the large population of such planets, and Zhu et al. (2018) estimated that the one third of the main-sequence stars are considered to harbor planetary systems composed of 3 planets with $R_{\rm p} \geq R_{\oplus}$ and orbital periods $P > 400$ days. Their observed orbital periods are relatively short, and this indicates that the viable paths for the formation are associated with migrations (e.g. Cossou et al., 2014) or in-situ formation (e.g. Raymond & Cossou, 2014). In the in-situ formation, Super-Earths can be considered as failed Hot Jupiters without sufficient gas accretion, which is caused by the late formation of cores due to low density of disks (Lee et al., 2014). The density of Super-Earth are diverse from ~ 0.1 g/cc (Masuda, 2014) to 7.46 g/cc (Carter et al., 2012) and the very low dense Super Earths are generally called "super-puffs", which would be mainly composed of gas rather than rock. Their formation mechanisms are uncertain, but hot or warm super-puffs do not form in gas-rich environments in in-situ formation, so they might be migrated to the current positions from outer orbits with sufficient gas supply (e.g. Lee & Chiang, 2016).

On the other hand, "Warm Jupiter" resides in between hot and cold Jupiters, and their
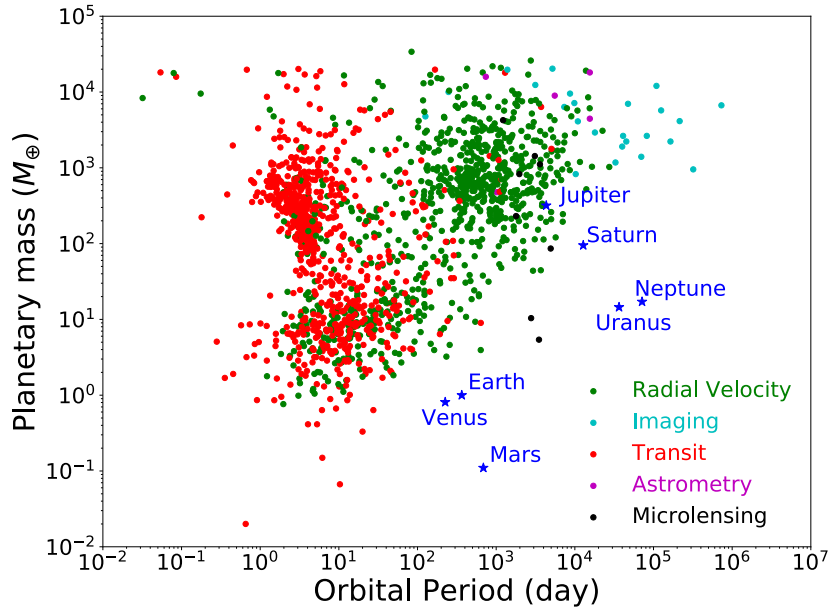
Figure 2.1 Orbital periods and planetary mass of exoplanets from the Extrasolar Planets Encyclopaedia (http://www.exoplanet.eu/catalog/). Colors express detection methods, and blue points correspond to planets in the Solar System.
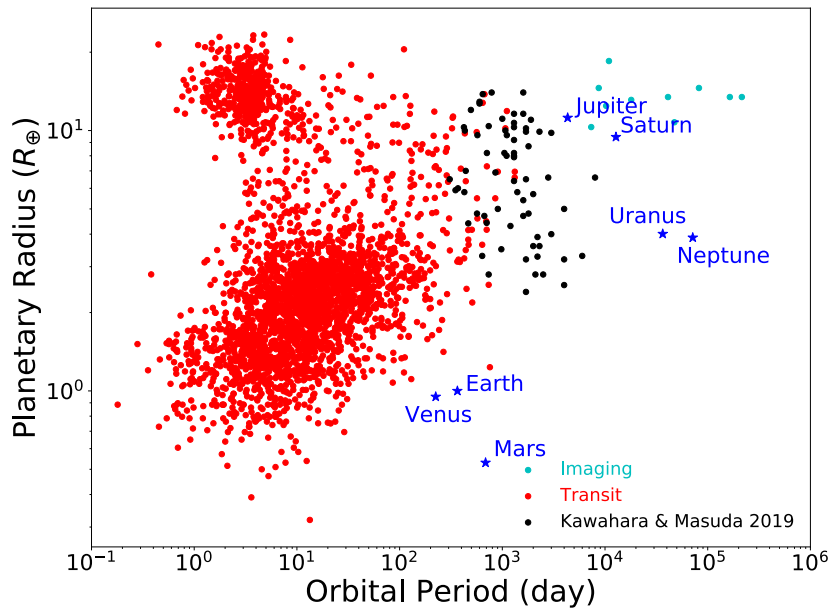
Figure 2.2 Orbital periods and planetary radii of exoplanets from the Extrasolar Planets Encyclopaedia (http://www.exoplanet.eu/catalog/). Black points are long-period transiting planets and their candidates detected by the Kepler (Kawahara & Masuda, 2019).

orbital periods are typically a few tens of days. They might be currently evolving from cold planets to close-in planets via some migration mechanisms, so their properties might be related to the connection between cold and hot Jupiters. However, their eccentricities are not so large to be largely migrated (e.g. Dawson et al., 2015), and their origin of has been still discussed (e.g. Dawson & Chiang, 2014).

Now, we turn to discuss exoplanets that resemble those in the Solar System. Basically, Solar-System analogs have small radii and/or long orbital periods, so their detection is observationally challenging even with the current technology. One exceptional class is "Cold Jupiter" with Jupiter radii and long orbital periods, most of which are probed by radial velocity surveys in decades (see Figure 2.1). The frequency of Jupiter-like planets is estimated to be 3%-10% (e.g. $6.2^{2.8}_{-1.6}\%$ for giant planets with $M_{\rm p} \sin i > M_{\rm J}$ and 3 au $< a < 10$ au (Wittenmyer et al., 2016), implying that the the Solar System-like systems might not be common structure among planetary systems.

The transit method can be exploited for identifying the long-period planets beyond the snowline. The concept is that double or even single transits could be caused by planets with orbital periods comparable or beyond the observational duration, which is at most 4 years in the Kepler satellite. The findings of such planets with the Kepler data are made by the citizen scientist Wang et al. (2015), visual inspection (Uehara et al., 2016), and automated pipeline (Foreman-Mackey et al., 2016; Osborn et al., 2016; Schmitt et al., 2017)). Black dots in Figue 2.2 show the summary of possible long-period planets found by the Kepler satellite from Kawahara & Masuda (2019)

More distant giant planets like Saturn, Neptune, and Uranus are still difficult to detect because of their long periods ($\simeq 100$ years), which are beyond the current observational duration for transit and radial velocity methods. On the other hand, the microlensing method is fairly sensitive to such distant planets. Gaudi et al. (2008) discovered a Jupiter+Saturn analog system around a $0.5M_\odot$-mass star. the star. In addition, Sumi et al. (2016) also found the first possible candidate of a Neptune analog, which might orbit a low mass M-dwarf with the mass of $0.19M_\odot$, albeit it could be min-Neptune or Super Earth around a brown dwarf.

Earth-like planets around Solar-type stars have also been technically challenging to detect and characterize. The transit method gives the tightest constraint on the occurrence rate, but as of today, there is no rocky planet with periods of $237 - 500$ days and planetary radii of $0.75 - 1.5R_\oplus$ around FGK star in the Kepler sample (Hsu et al., 2019). This result sets the upper limit on the occurrence rate to be 0.27 at 1σ level. Among the planets, Kepler-452 is the most Earth-like planet around a solar type star (Jenkins et al., 2015), although its radius $1.5^{+0.32}_{-0.22}R_\oplus$ is still slightly larger than the Earth. Since their statistical signature is very weak, their detection could be false positive (Mullally et al., 2018).

Since the first discovery of exoplanetary systems, our knowledge and technology have been dramatically advanced. Although the current observations still allow the detection of planets with large radii and/or not too long orbital periods, the future ground and space missions (e.g. Gaia) will open a new window to the unexplored landscape, and finally, the occurrence rates of Solar System-like systems will be quantitatively evaluated.

2.2 Solar System analogs beyond planets: exomoons, exoplanetary rings, and exoplanetary surface

The detection of exoplanets is just the beginning of a long story for unveiling the histories of formation and evolution of planets. The next key step is observational characterizations of exoplanets, ranging from the basic orbital and physical parameters including orbital periods, radii, masses, and eccentricities to planetary compositions, atmosphere, habitability, magnetic fields, surface inhomogeneities, and even signatures of life. Another natural approach will be identifications of analogs of moons, planetary rings, continents, ocean. asteroids, comets, trans-Neptunian objects, Kuiper belts. They can be different from what we know in the Solar System, and they will tell us a new perspective of the planetary formation.

In this section, we discuss the detection of exomoons, exoplanetary rings, and surface inhomogeneities, all of which are main representatives of the planetary structures. For the latter two themes, we present methodologies to identify them in this thesis.

2.2.1 Exomoons

The detection of exomoons is still at the forefront of the current observations, and there is no solid confirmation of the systems. One of promising methods is the transit techinque, which probes the potential transits of exomoons and/or slight wobble of the planets through transit timing and duration variations (Kipping, 2009a,b). Kipping et al. (2012) initiated a serious search for exomoons using the Kepler data, and they finally obtained the statistical constraint and a hint for the single-moon populations (Teachey et al., 2018). Surprisingly, they also claimed the detection of the possible planet-moon system Kepler-1625 b. Their follow-up observations with the Hubble Space Telescope (HST) still favor the exomoon hypotheses, and the system is considered to be composed of Jupiter masse planet with ∼1 year orbit and the Neptune-sized exomoon (Teachey & Kipping, 2018). Although some groups cast doubt on the detection by pointing out the systematical errors in the analyses (Heller et al., 2019; Kreidberg et al., 2019), their claim is very encouraging for the further studies on this field.

The microlensing method is another approach to detect exomoons via detailed modeling of the light curvess. Bennett et al. (2014) discovered an event of microlensing that can be interpreted as motion of the Sub-Earth sized exomoon candidate orbiting around the planet with 4 Jupiter mass. The method allows the other solutions without the moons, but the future observations with WFIRST would be promising for the further studies.

Direct imaging technique is another possible path to find exomoons in the future, but their reflectional light is seriously contaminated by planetary light. Agol et al. (2015) proposed the methodology for detecting moon by exploiting positional displacements of the center of light called "spectroastrometry". The relative ratios of reflectional light of planets and moons depend on wavelength, so the difference can be used to estimate the orbital motions of the moon, the planetary mass, or even the separate spectrum of two bodies.

The detection of exomoons is still challenging, but attracting the interests at the same time. The transit and microlensing methods are already attempted to the searches, and the direct imaging technique is also promising in the future observations.

2.2.2 Exoplanetary rings

Since giant planets in the Solar System are commonly accompanied by planetary rings, we naturally expect that rings should also exist around exoplanets. However, due to the observational difficulty in detecting them, there has not been any confirmed candidate.

Saturnian rings, which are mainly composed of icy particles, have large optical depth implying the large amount of scattering, reflection, and blocking. One of approaches is the direct imaging of reflectional light from ringed planets. Arnold & Schneider (2004) and Dyudina et al. (2005) found that a ringed planet gives a significantly asymmetric phase curve with varying in amplitude several times during one period, and the phase curve of a ringed planet could be discriminated from that of a ringless planet. The current direct-imaging technique does not have sufficient sensitivity for that, but the future observation for the long duration is promising to find the solid evidence of the ring.

Although the direct imaging of a ring is not realistic in the current technology, the transit method is effective for the detection of a ring even with the current precision. Specifically, it was demonstrated that the Kepler satellite has the sensitivity to identify exoplanetary (Barnes & Fortney, 2004). Once the signatures are detected, the spectroscopic observation during the transit gives another complimentary evidence (Ohta et al., 2009). The serious search for exoplanetary rings using the Kepler data was rewarding but not conducted. In section 2.2.2.1, we summarize the formulation of the transit method for detecting a ringed planet, and, in section 2.2.2.2, we present the previous attempts to search for planetary rings.

2.2.2.1 Transit Photometry and Its Application to Ring Search

Transit is an astronomical event when a small celestial object blocks light from a larger body by passing between the observer and the source. During the transit, the stellar flux apparently decreases by blocking, and it could be the indirect evidence of a planet in exoplanetary sciences. The signatures of the transit depend on orbital configurations and sizes of both a planet and star.
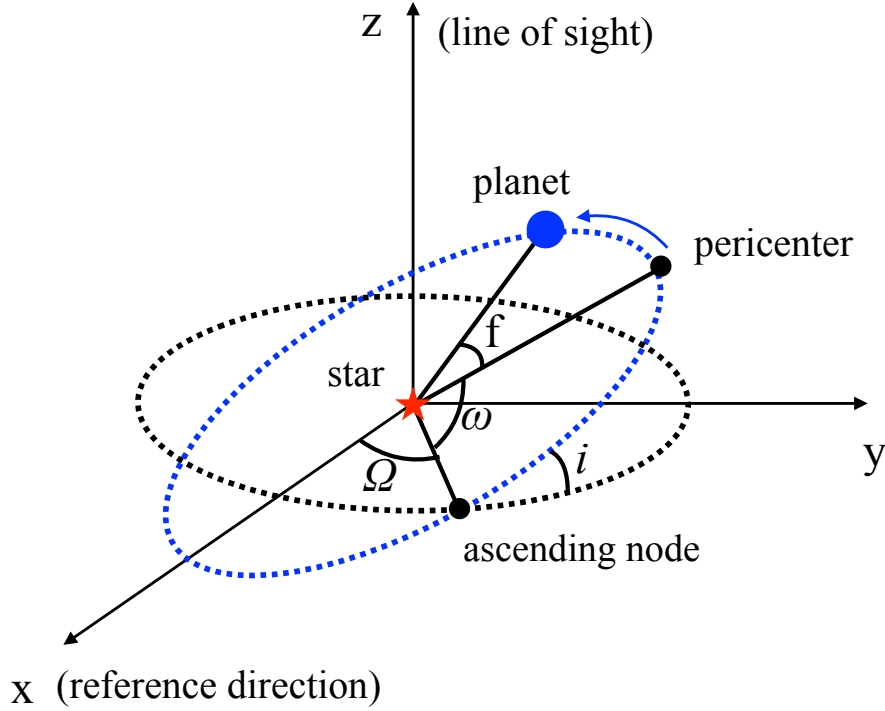
Figure 2.3 Orbital configuration of a planet and star, and their geometrical parameters. The z axis is taken to be the direction of a line of sight, and x and y axes are taken to be orthogonal to z axis.

Figure 2.3 depicts a planetary orbital configuration and geometrical parameters. Assuming the Keplerian motion, the relative position from a star to a planet is written as:

$$x = r(\cos \Omega \cos(\omega + f) - \sin \Omega \sin(\omega + f) \cos i), \tag{2.1}$$
$$y = r(\sin \Omega \cos(\omega + f) + \cos \Omega \sin(\omega + f) \cos i), \tag{2.2}$$
$$z = r \sin(\omega + f) \sin i, \tag{2.3}$$

where r is the distance from the planet to the star, Ω is the longitude of ascending node, i is the orbital inclination, ω is the argument of pericenter, and f is the true anomaly. Here, the true anomaly f describes the time evolution of the system, and it is determined by the orbital equations (e.g. the Kepler equation).

We take the z axis to be the line of sight, and the total relative flux can be rewritten as

$$F = 1 - \frac{\int I(x,y)D(x,y,t)dS}{I_{all}}, \tag{2.4}$$

where $I(x,y)$ is the stellar intensity map, and $D(x,y,t)$ describes the fraction of light that is blocked by the planet at (x,y,t). Assuming the limb-darkening law, $I(x,y)$ is

described as

$$I(x, y) = I(r) = I_0(1 - 2q_2\sqrt{q_1}(1 - \mu) - \sqrt{q_1}(1 - 2q_2)(1 - \mu)^2), \quad (2.5)$$

where (q_1, q_2) are limb-darkening parameters with $0 < q_1 < 1, 0 < q_2 < 1$ (Kipping, 2013), I_0 is the intensity at the stellar center, and $\mu = \sqrt{1 - (r/R_\star)^2}$ with the stellar radius $R_\star$. The calculation of Eq (2.4) requires the integration, which depends on the exact shape of the planet. We can consider a single planet, a ringed planet, or even a planet with an moon. The calculation itself can be done by pixel-by-pixel integration on the stellar surface, but the efficient and accurate algorithms have been proposed. As for the ringless planet, Mandel & Agol (2002) presented exact analytic expression for the eclipse of a star assuming the stellar intensity maps including quadratic limb darkening. On the other hand, there had been no proposed analytic method to calculate the integration in case of the ringed planet.

In general, rings are described by five parameters as summarized in Figure 2.4: inner radius of a ring R_{in}, outer radius R_{out}, the shading parameter T, and ring geometry (θ, ϕ). The shading parameter determines the form of $D(x, y, t)$ as:

$$D(x, y, t) = \begin{cases} 1 & : \text{if } (x, y) \text{ is within the planetary disk} \\ T & : \text{if } (x, y) \text{ is within the ring disk, but out of the planetary disk} \\ 0 & : \text{otherwise.} \end{cases} \quad (2.6)$$

Instead of using $(R_{\mathrm{in}}, R_{\mathrm{out}})$, we adopt dimensionless parameters for efficient fitting:

$$r_{\mathrm{in/p}} \equiv \frac{R_{\mathrm{in}}}{R_{\mathrm{p}}}, \qquad r_{\mathrm{out/in}} \equiv \frac{R_{\mathrm{out}}}{R_{\mathrm{in}}}. \quad (2.7)$$
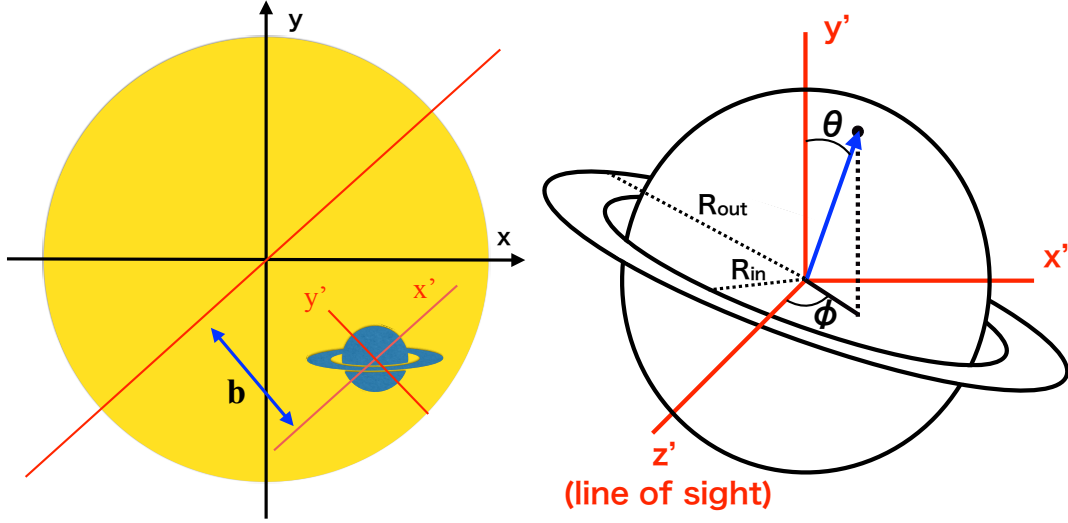
Figure 2.4 Schematic picture of transiting ringed planet. (a) Transiting ringed planet on a stellar disk. The x' axis is taken to be parallel to the transit chord, whose displacement from the stellar center is described by $b = a \cos i / R_\star$. (b) Geometrical parameters for ringed planet. (θ, ϕ) specify the direction of the ring axis, R_{in} shows the inner ring radius, and R_{out} shows the outer ring radius.

Aizawa et al. (2017) presented a formulation for the fast and accurate numerical integration of Eq (2.4) for a transiting ringed planet. They adopted a cylindrical coordinates (r, θ). Then, with r fixed, we can calculate intersections between a circle with radius of r and a ringed planet, and, on the circle, the value of $D(x, y, t)$ can change only at these boundaries.

$$\int I(x,y)D(x,y,t)dS = \sum_l D_l \int (\theta_{l+1}(r) - \theta_l(r))I(\sqrt{1-(r/R_\star)^2})r dr, \qquad (2.8)$$

where $D(x, y, t)$ takes a constant value between $\theta_l(r) < \theta < \theta_{l+1}(r)$. The expressions for $\theta_l(r)$ are reduced to quartic equations, and there are at most 10 possible solutions for θ. The number of possible solutions depends on r, and the boundary values are also obtained by solving quartic equations. The specific derivations for $\theta_l(r)$ are given in Aizawa et al. (2017).

Using the above model, they tested the precision and computational time assuming a transit of Saturn-like plane with $R_{\mathrm{p}}/R_\star = 0.083667$, $R_{\mathrm{in/p}} = 1.5$, $R_{\mathrm{out/p}} = 2.0$, $\theta = \pi/3$, $\phi = \pi/3$, $T = 1.0$. For orbital parameters and stellar parameters, they took $P = 10759.3$ days, $a/R_\star = 2049.89$, $b = 0.5$, $q_1 = 0.49$, and $q_2 = 0.34$. For comparison, they also considered the pixel-by-pixel integration around the planetary center (Ohta et al. 2009). They found that the current ring model at least gives the precision of 10^{-7}, and the computational speed is faster than the pixel integration when we require the precision beyond 10^{-5}. This comparison confirmed the robustness and speed of this computational scheme.

2.2.2.2 Previous Attempt to Search for Rings

Previously, there are several attempts to search for exoplanetary rings. Brown et al. (2001) for the first time set constraint on the ring size using the HST observation of a transiting planet HD209458, and they excluded the opaque ring with the radius of 1.8 times the planetary radius. Santos et al. (2015) also investigated the possibility that the presence of a ring account for the large reflectional light and rotational velocity of Peg 51 b, but the required configuration is inconsistent with the orbital stability. Therefore, they excluded the ring hypothesis for Peg 51 b. Lecavelier des Etangs et al. (2017) also tried to identify the ring around CoRoT-9b using the Spitzer photometry, and they did not find any signature of the ring.

In the meantime, a few searches for rings using the Kepler have been also conducted. Heising et al. (2015) searched for rings around 21 Kepler planets with 1 day $< P < 51$ days, but they found no plausible candidate. On the other hand, Aizawa et al. (2017) attempted to identify exoplanetary rings among 89 long-period planets ($P > 200$ days for most systems) with at most three transits in order to search for Saturn-like icy rings. They detected one possible candidate around KIC 10403228, whose light curve is consistent with single transit caused by a planet with a Saturnian sized ring. Due to the nature of the single event, the data are also consistent with a binary planet model and a circumstellar disk around a red giant star. After the publication of the paper, we inspected the parallax data presented by the gaia DR2, and find that the the host star is unlikely to be a giant star. As the orbital period is uncertain for this system, the further discrimination of the scenarios is challenging unless follow-up photometric observations including TESS give the additional transit.

Although Aizawa et al. (2017) explored cold planets, the majority of Kepler planets have not been still investigated. Saturnian rings are composed of icy particles, but it is not strange that the rocky rings are common around exoplanets. Therefore, the search for the exoplanetary rocky rings using the Kepler data is awaited, and we explore this possibility in Chapter 3.

2.2.3 Global Mapping of Earth Analogs

The surface of the Earth is diverse, and it is composed of land, ocean, clouds, vegetation, and snow. These features would also be common on exoplanets, and the identification of such surface information is rewarding to understand the exoplanetary environments. In addition, the surface information includes the vegetation, so it can be the evidence of a biosignature of the planet life. However, the characterization of the exoplanetary surfaces is not straightforward because it is basically impossible to directly resolve the planet. Given this difficulty, Ford et al. (2001) showed that the light curves scattered by a planet vary in intensity due to the apparent motions of surface inhomogeneities caused by planetary spins. By computing reflectional light curves in the multi-band observations, they showed that the light curves can be used to reconstruct the surface properties including land, ice, and even plant life. Based on this concept, the techniques of the inverse modeling have been developed by subsequent studies. In this section, we

summarize the formulation of global mapping technique.

2.2.3.1 Forward Modeling of Reflectional Light from Exoplanet

We briefly describe the forward modeling of the global mapping following Fujii & Kawahara (2012). Figure 2.5 summarizes the geometric configuration and parameters. The scattering property of planetary surface depends on positions, and it is descried by the bidirectional reflectance distribution function (BRDF) $f(\theta_0, \theta_1, \varphi)$, where θ_0 is the incident zenith angle, θ_1 is the scattering zenith angle, and φ is the azimuthal angle between the direction of the incident and scattering light. Then, the scattering intensity at each pixel on the planetary surface is given by

$$\frac{dI}{d\omega} = F_\star R_{\rm p}^2 f(\theta_0, \theta_1, \varphi) \cos\theta_0 \cos\theta_1, \tag{2.9}$$

where $F_\star$ is the stellar flux, $R_{\rm p}$ is the planetary radius.
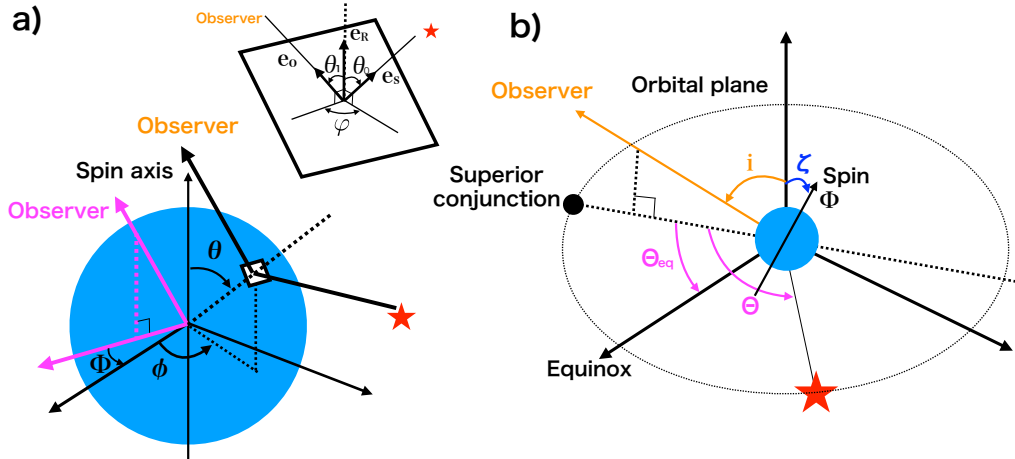
Figure 2.5 (a) Schematic picture of planetary reflection from a star to an observer. The planetary surface is described by (θ, ϕ), and the spin motion is descried by Φ. The close view of the surface is shown in the upper right. (b) Orbital configuration of planetary system with reflection. In the figure, ζ describes the planetary obliquity, Θ is the ecliptic longitude, and $\Theta_{\rm eq}$ is the ecliptic longitude of the equinox.

The simplest expression for BRDF is the Lambertian reflection

$$f(\theta_0, \theta_1, \varphi) = \frac{m(\theta, \phi)}{\pi}, \tag{2.10}$$

where $m(\theta, \phi)$ is a surface albedo on (θ, ϕ). However, this is the approximation for the uniform reflection, and in reality, the functional form of $f(\theta_0, \theta_1, \varphi)$ depends on surface types (e.g. Fujii et al., 2010). The scattering for land is generally characterized by the

Rossi-Li model, which incorporates the isotropic scattering, the effect of thickness of the land, and the effect of the shadow (Eq (14) in Fujii et al. (2010)). The scattering for the ocean is descried by the characteristic BRDF function with the specular reflection when $\theta_0 = \theta_1$. The specular reflection could be exploited to directly discover the evidence of the ocean from light curves (Robinson et al., 2010).

The incident light is scattered by not only the surface but the planetary atmosphere (e.g. Fujii et al., 2010). In this case, the BRDF function is modified as

$$f(\theta_0, \theta_1, \varphi)_{\mathrm{atm},k} = f_{\mathrm{atm}}(\theta_0, \theta_1, \varphi) + C_{\mathrm{atm}}(\theta_0, \theta_1, \varphi) \times f_{\mathrm{surf},k}(\theta_0, \theta_1, \varphi), \tag{2.11}$$

where $f_{\mathrm{atm}}(\theta_0, \theta_1, \phi)$ describes the BRDF function for the atmosphere, and $C_{\mathrm{atm}}(\theta_0, \theta_1, \phi)$ describes the attenuation due to the atmosphere.

Assuming the Lambert reflection in Eq (2.10), the total reflectional light on the surface is given by

$$I = \int_s F_\star R_{\mathrm{p}}^2 f(\theta_0, \theta_1, \varphi) \cos\theta_0 \cos\theta_1 d\Omega, \tag{2.12}$$

$$= F_\star R_{\mathrm{p}}^2 \int_s \frac{m(\theta, \phi)}{\pi} \cos\theta_0 \cos\theta_1 d\Omega, \tag{2.13}$$

where (θ, ϕ) is the spherical coordinate system, s is the area that is visible both from an observer and a star. Total reflectance depends on wavelength, and Figure 2.6 shows the specific reflectance depending on surface types. Albedo of the land generally is large for the long wavelength. The albedo of the vegetation has the sharp rise around $\lambda = 0.7 \mu m$, and this called red edge (e.g. Robinson et al., 2010). The snow albedo is very close to 1, and the water albedo is close to zero.
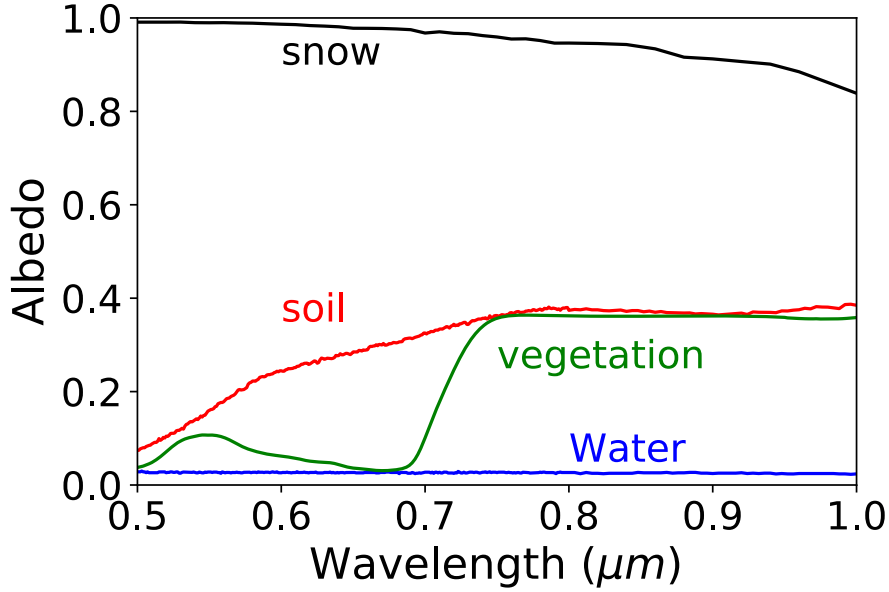
Figure 2.6 Effective albedo and its dependency on wavelength for various components taken from the ECOSTRESS spectral library (https://speclib.jpl.nasa.gov). We assume that snow is "Fine Snow", vegetation is "Uvularia sessifolia", water is "Tap Water", and soil is "Dark yellowish brown micaceous loam" in the library.

The integration in Eq (2.13) requires the expressions for geometrical positions including a planet and a star, and Figure 2.5 summarizes geometric parameters. The spin motion is specified by $\Phi(t) = \omega_{\mathrm{spin}}t + \Phi_{\mathrm{offset}}$, where ω_{spin} is the angular velocity of the planetary spin and Φ_{offset} is the constant offset for $\Phi(t)$. The ecliptic longitude is descried by Θ, whose origin is taken as the superior conjunction. The orbital inclination that is the angle between the line of sight and orbital axis is defined as i. Finally, the spin axis is specified by the obliquity ζ and the ecliptic longitude of the vernal equinox Θ_{eq}.

The ecliptic longitude Θ and the spin motion $\Phi(t)$ determine time evolution of the geometrical evolution among planet, star, and a observer. We define the unit vector from the planetary surface (θ, ϕ) to the host star as e_{S}, the unit vector from the surface to the observer as e_{O}, and the vector normal to the surface as e_{R}. We introduce the coordinate system (x, y, z), where x axis is the direction of equinox, and the z axis is taken to the orbital axis. In addition, the y axis is taken to construct rectangular coordinate system. Then, the components of vectors e_{S}, e_{O}, and e_{R} are given as:

$$e_{\mathrm{S}} = (\cos(\Theta - \Theta_{\mathrm{eq}}), \sin(\Theta - \Theta_{\mathrm{eq}}), 0)$$
$$e_{\mathrm{O}} = (\sin i \cos \Theta_{\mathrm{eq}}, -\sin i \sin \Theta_{\mathrm{eq}}, \cos i)$$
$$e_{\mathrm{R}} = (\cos(\phi + \Phi) \sin \theta), \cos \zeta \sin(\theta + \Phi) \sin \theta + \sin \zeta \cos \theta,$$
$$- \sin \zeta \sin(\phi + \Phi) \sin \theta + \cos \zeta \cos \theta).$$

Using these expressions, we can compute $\cos \theta_0$ and $\cos \theta_1$ as well as I in the following

manner:

$$I = \frac{F_\star R_p^2}{\pi} \int m(\theta, \phi) W(\theta, \phi; \Theta, \Phi) d\Omega, \tag{2.14}$$

where we define the weight functions for the illuminated $W_I(\theta, \phi; \Theta, \Phi)$, visible area $W_V(\theta, \phi; \Phi)$, and their multiplication $W(\theta, \phi; \Theta, \Phi)$ as:

$$W_I(\theta, \phi; \Theta, \Phi) = \max\{e_S \cdot e_R, 0\}, \tag{2.15}$$

$$W_V(\theta, \phi; \Phi) = \max\{e_O \cdot e_R, 0\}, \tag{2.16}$$

$$W(\theta, \phi; \Theta, \Phi) = W_I(\theta, \phi; \Theta, \Phi) \times W_V(\theta, \phi; \Phi). \tag{2.17}$$

$$\tag{2.18}$$

2.2.3.2 Inverse modeling of mapping

The previous section deals with the forward modeling, and we can conversely exploit Eq (2.14) to estimate the planetary surface from the light curves. We adopt the linearized expression of Eq (2.14) using the discretized planetary surface with N_{pixel} pixels:

$$I = \frac{F_\star R_p^2}{\pi} \sum_j^{N_{pixel}} m(\theta_j, \phi_j) W(\theta_j, \phi_j; \Theta, \Phi) \Delta\omega_j, \tag{2.19}$$

where we assume the small pixels with the solid angle $\Delta\omega_j$. Then, by normalizing I, we obtain

$$d_i = \sum_j^{N_{pixel}} G_{i,j} m(\theta_j, \phi_j) + \epsilon_i, \tag{2.20}$$

$$G_{i,j} = W(\theta_j, \phi_j; \Theta(t_i), \Phi(t_i)) \Delta\omega_j, \tag{2.21}$$

where d_i is the i-th normalized data, t_i is the time for i-th data, and ϵ_i is the observational error associated with d_i. Generally, the above problem is ill-posed, and there is no unique solution for a given d. To give the unique solution, Kawahara & Fujii (2011) introduced the Tikhonov regularization, which balances between the observational noise and the spatial resolution of the surface. The cost function for minimization is given by

$$Q_\lambda \equiv \sum_{i=1}^{N_{data}} \frac{|d(t_i) - \sum_j^{N_{pixel}} G_{i,j} m_j|^2}{\sigma_i^2} + \lambda^2 |m - \hat{m}|^2, \tag{2.22}$$

where σ_i is the standard deviation of the observational error for d_i, and $\hat{m} = \langle d \rangle$ is taken to be the mean of the data as a prior for the model. If the geometry is known, the minimization for Q_λ can be analytically solved:

$$m_{est,\lambda} = V\Sigma_\lambda U^T (\tilde{d} - \tilde{G}\hat{m}) + \hat{m}, \tag{2.23}$$

$$(\Sigma_\lambda)_{i,j} \equiv \frac{\kappa_i}{\kappa_i^2 + \lambda^2} \delta_{i,j}, \tag{2.24}$$

where we introduce $\tilde{d}_i \equiv d_i \sigma_i$, , $\tilde{G}_{i,j} = G_{i,j}/\sigma_i$, and Σ_λ is the diagonal matrix. The matrix G is decomposed as $G = U\Lambda V^T$, where U and V are orthogonal matrices, using the singular value decomposition. The i-th eigenvalue of G is κ_i, which is the i-th component of Σ. In order to determine the optimal λ, Kawahara & Fujii (2011) adopted L-curve criterion, which searches for λ with the maximum curvature point of the model norm $|m_{\text{est},\lambda} - \hat{m}|$ versus residual $|d - Gm_{\text{est},\lambda}|$ plot (Hansen, 2010). We note that the Tikhonov regularization does not build on physical foundation, so there still remain freedoms to choose the appropriate terms for the mapping.

When deriving the analytical solution in Eq (2.24), we implicitly assume the spin parameter $(\zeta, \Theta_{\text{eq}})$, but they should be also estimated from the data as well. One can exploit Eq (2.22) to infer $(\zeta, \Theta_{\text{eq}})$ by minimizing the cost function using some algorithms (e.g. Nelder-Mead method; Kawahara & Fujii (2011)). We can also directly read off the geometry from light curves by analyzing frequency modulations in the data, which are caused by the spin motions (Kawahara, 2016). The proposed method does not require the mapping method, so it is complementary to other methods that use the amplitude modulations.

The above formulations implicitly assume one band observation, but they can be naturally extended to multi-band observations in the real observation. Fujii et al. (2011) reconstructed the colored longitudinal map of the Earth using the real observation by assuming the specific surface types including oceans and soil.

In real observations, the clouds significantly contribute to the light variations, and the mitigation of their effect is one of important themes in this field. The effective albedo of clouds is basically flat in wavelength, so it can be mitigated by subtracting one color from another. On the other hand, the subtraction does no erase the reflection of the land, whose albedo varies in wavelength (see Figure 2.6). On the basis of this concept, Kawahara & Fujii (2011) employed the difference in the light curves between red and blue bands, and they successfully recovered the overall land distribution of the Earth from the light curve.

Beyond the simple subtraction, one can also adopt the principal component analysis (PCA), which is one of methods for reducing the dimensionality of the data by calculating orthogonal eigenvectors for sets of vectors. Assuming the n data of m elements X, the covariant matrix of the data is given by $X^T X$. The covariant matrix is symmetric matrix, so it can be diagonalized as $X^T X = U\Lambda U^T$, where Λ is a diagonal matrix, and U is an unitary matrix composed of eigenvectors u_k with m elements. The eigenvalues of Λ represent the variance of the eigenvectors, which describe the contribution of the k-th component u_k to the full variation of the light curves.

Cowan et al. (2009) firstly introduced PCA to extract the surface information from 2-days observations of the Earth in seven different bands in the EPOXI observation. They claimed that the derived eigencolors represent the relative color subtracted by the Earth mean color that is mostly explained by a cloud spectrum with atmospheric scattering. Among seven colors, the two strongest colors turns out to account for the 98 % variance of the data, and the first eigencolor is significantly sensitive to variations in longer wavelength corresponding to cloud-free continents. The second one corresponds to the shorter wavelength corresponding to cloud-free ocean. On the other hand, Fan et al. (2019) in-

troduced the same technique to extract surface information using 2-years observations of the Earth. In this case, they found that the strongest component describe the variations caused by cloud reflection, and the second strongest one is closely correlated, specifically linearly, with the land fraction of the Earth the coefficient of determination r^2 is 0.91. The difference between the results of PCA and their interpretation would be ascribed to the difference in the observation duration.

PCA does not require the prior information on the surface types, so it can be applied to not only the Earth but also the exoplanets. However, PCA does not resolve the surface types (land, plant, snow), so the further improved methods, which enable the determinations of the surface types and distributions simultaneously, would be required to recover a "color" map of an exoplanet.

One possible improvement in the method is the appropriate adoption of the regularization term in Eq (2.22), because the Tikhonov regularization does not build on physical validity. In addition, previous studies assumed observational duration of a few years, but this will not be realistic to occupy satellites in a such long duration only for the global mapping. We explore these issues further in Chapter 5.

2.3 Angular Momentum Evolution in Star Formation and Emergent Constraint on Star Formation from Alignment

Exoplanetary systems are originally formed from molecular clouds, and the filling the gap between them is important to unveil the evolutional histories of exoplanets. Especially, proto-planetary disks can be considered to be the initial conditions of planet formation, so revealing their origins is crucially important for studying the subsequent evolution of exoplanetary systems (e.g. Simbulan et al., 2017).

One of key concepts in the star formation is the angular momentum evolution of stellar systems. Let us consider a cloud core with mass of M, radius of R_{init}, and angular velocity of Ω_{init}. Then, the total angular momentum can be roughly approximated as $M R_{\text{init}}^2 \Omega_{\text{init}}$. If this cloud core contracts to the object with the size of R_{end}, the angular velocity is given by:

$$\Omega_{\text{end}} = \frac{R_{\text{init}}^2}{R_{\text{end}}^2} \Omega_{\text{init}}, \tag{2.25}$$

where we assume the angular momentum preservation. Let us adopt $\Omega_{\text{init}} \simeq 10^{-6}$ yr^{-1} and $R_{\text{init}} = 0.1$ pc for the cloud core (Goodman et al., 1993). Then, the stellar angular velocity is roughly 10^7 yr^{-1} if we adopt the sun radius of $R_{\text{end}} = 2 \times 10^{-8}$ pc. This angular velocity is 3 orders of magnitude larger than the break-up angular velocity of the Sun, $\Omega_{\text{break}} \simeq \sqrt{GM_\odot/R_\odot^3} \simeq 2 \times 10^4$ yr^{-1}, so this value is not allowed in the real situation, and this is called "angular momentum problem". If we equate the Kepler angular velocity with Eq (2.25), we find $R_{\text{end}} \simeq 5000$ au implying that there should be the rotationally supported structures at this scale, and these correspond to stellar envelopes. This simple

discussion demonstrates the requirement of the physical processes for extracting the initial angular momentums during the course of stellar evolution to finally make the star.

Figure 2.7 summarizes the evolution of the specific angular momentum from cloud to stellar scales. The rotations of the systems are basically probed by velocity gradients through the measurement of the Doppler shift of line emissions, mostly on the assumption of a solid rotation. Before going into the detail, we briefly comment on a few caveats in Figure 2.7. Firstly, the angular momentum is derived from the assumption that the velocity gradients trace the rotations of the systems, but this might not be true due to the complexity in kinematics including turbulent and infalling motions (e.g. Dib et al., 2010). Secondly, the figure only summarizes the specific angular momentum for independent objects rather than collecting the radial structure for particular systems, in other words, spatial dependence. In the similar manner, the figure only considers snapshots of the individual systems, so it does not correctly trace the evolution of the star formation from cloud to smaller scales. Having said so, the figure well describes the evolution of the angular momenta, and it is useful for grasping the overall picture of the evolution

The angular momentum evolution is mainly divided into three regimes. In the first regime with the length scale $\simeq 0.1$ pc, the specific angular momentum roughly follows $R^{1.5}$. Historically, Fleck & Clark (1981) compiled measurements of rotations for 12 clouds using molecular lines, and they found the relation $\Omega \propto R^{-2/3}$. For the smaller region, Goodman et al. (1993) also studied the rotations of 43 cores by measuring the velocity gradients, and found that the specific angular momenta are roughly scaled with $R^{1.5}$ consistently with Fleck & Clark (1981). These results were also confirmed by subsequent studies down to sub parsec scales (Caselli et al., 2002; Pirogov et al., 2003; Chen et al., 2007; Tobin et al., 2011; Tatematsu et al., 2016; Chen et al., 2019). Recently, Pineda et al. (2019) also studied the spatial distributions of specific angular momentum for cores, and they found that the relation $j_{\mathrm{fit}}(r) \propto r^{-1.80}$ from 800 to 10000 au. This might indicate the transition from the turbulent region $j \propto R^{1.5}$ to the solid rotation regime $j \propto R^{2.0}$ of the cores.

In the second regime beyond the scale of 0.1 pc for cores, the cores start to collapse gravitationally, and the specific angular momentum keeps constant until the rotationally supported structures are formed. Ohashi et al. (1997) compiled the interferometric observations of 7 young stars with rotationally supported disks and infalling envelopes in the Taurus molecular cloud, and compared the specific angular momenta with those of dense cores. They found that the specific angular momenta of envelopes are basically constant, $\simeq 10^{-3}$ km s^{-1} pc, consistently with the angular momentum preservation. In the third regime of proto-planetary disks, the specific angular momentum follows the Keplerian motion $\propto \sqrt{GMr}$, where G is the gravitational constant, M is the stellar mass. The specific angular momentum of proto-planetary disks are typically within the range of $\log_{10} j$ cm^{2}s$^{-1} = 19.4 \sim 20.9$ (Simon et al., 2000; Isella et al., 2009; Andrews et al., 2010; Williams & Cieza, 2011). Proto-planetary disks and envelope are accreted onto the protostars by losing their own angular momentums, and angular momentums transportation in proto-planetary disks would be driven by viscosity or other mechanisms (e.g, spiral density waves or disk winds) (e.g. Rafikov, 2017).
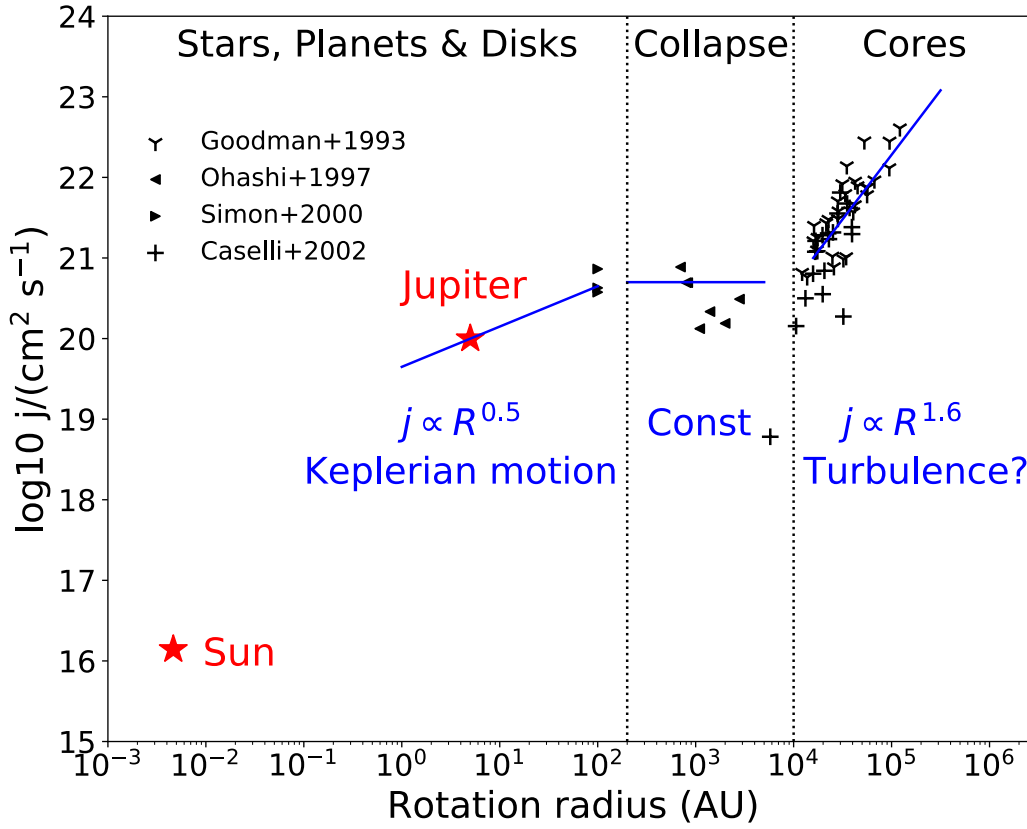
Figure 2.7 Specific angular momentum evolution in stellar systems from core scales to Sun (modified version of Figure 8 in Belloche (2013)). The values of specific angular momentum are taken from several literature (Goodman et al., 1993; Ohashi et al., 1997; Simon et al., 2000; Caselli et al., 2002). In the first regime, the specific angular momentum follows the relation $j \propto R^{1.5-1.6}$. In the second regime during the gravitational collapse, the angular momentum is preserved, and in the third regime, the rotation is described as the Keplerian motion $j \propto R^{0.5}$.

One of possible origins for the rotation is the velocity distribution, which follows the power law relation $\sigma_u(R) \sim R^\beta$ in molecular clouds (Larson, 1981). The values of β was estimated to be 0.38 in Larson (1981) and β of 0.5 in subsequent studies (e.g. Heyer & Brunt, 2004). The origin of $\sigma_u(R) \sim R^\beta$ is considered to be turbulent motions, which predict $\beta = 0.33$ in case of the Kolomogorov turbulence (Kolmogorov, 1941a,b). From the relation $\sigma_u(R) \sim R^{0.5}$, the dimension analysis of j predicts the relation $j \propto Rv \propto R^{1.5}$, and this is consistent with the empirical relation from measurement of core's rotations $j \propto R^{1.5-1.6}$ (e.g. Goodman et al., 1993) (also see Figure 2.7). Apart from the above dimensional analysis, the observed relation $j \propto R^{1.5}$ is also reproduced in 3d MHD simulations of core formation, which incorporate the turbulence as well as magnetic fields (e.g. Li et al., 2004; Chen & Ostriker, 2015, 2018). These facts support the hypothesis that the angular momentum is originated from or, furthermore, "generated" by the turbulent

motions in molecular clouds.

There are also other possible paths for explaining the origins of angular momentum. Corsaro et al. (2017) presented three-dimensional hydrodynamical simulations of protocluster formation by changing the initial rotations of the molecular clouds. When the initial rotation is very large, they found that the directions of angular momentums are preferentially directed toward that of the injected rotation, suggesting that the angular momentum is originated from the global rotation of clouds. On the other hand, Kuznetsova et al. (2019) presented a suit of simulations of protocore formation in a collapsing molecular clouds with a global rotation in a similar manner to Corsaro et al. (2017), and they found that the direction of the initial global rotation does not affect those of angular momentums of resultant cores. They claimed that the angular momentums are generated mainly by the torques between dense parts in the gas rather than the global rotation, and this is consistent with their result that the enhancement in the density of gas particles increases the specific angular momentums as well.

In the above, we briefly overview the evolution of angular momentum and their origins, which are still uncertain even faced with large and diverse observations. The difficulty in revealing the star formation partly comes from the that the observations only give snapshot of specific systems at specific timings rather than the entire history of star formation. Simulations can resolve this problem partly, but they simultaneously bring new additional uncertainties including the initial conditions and the controlling parameters, and these make the robust comparison challenging. Therefore, any small piece of observational findings is precious to fully understand the picture of the star formation, which also advances our understanding of the planetary formation as well.

If the stellar angular momentum is originated from turbulent motions in molecular gas, the directions of rotations of stellar systems are expected to be randomly distributed. Conversely, if the orientations of stellar angular momentum are not random, the angular momentums are not simply generated by the random turbulent motion but by other physics or their combinations. For example, as studied in Corsaro et al. (2017), the global rotation of clouds possibly accounts for the angular momentum of each stellar component, and if so, the directions of rotations would be preferentially directed toward the initial rotation. In this way, the spatial correlations among stellar angular momentums can constrain the nature of the stellar rotations, which would be originally determined by the complex balance among turbulent motions, rotation, gravity, pressure, radiation, and magnetic fields.

The strong tool for investigating the relation is the distribution of stellar inclinations. The values can be obtained by exploiting the spectroscopic projected stellar rotational velocity $v_\star \sin i_{\rm s}$, the stellar rotation period $P_{\rm rot}$, and the stellar radius $R_\star$. Using this concept, however, Jackson & Jeffries (2010) found no statistical trend of the alignment of stellar spins in Pleiades and Alpha Per clusters. Jackson et al. (2018) also reconfirmed that there is no strong evidence of the alignment among stars in Pleiades. On the other hand, Corsaro et al. (2017) measured the stellar inclination i_s of 48 red giants in two open clusters, and they claimed that both of fields show the evidence of the strong alignment. Furthermore, Kovacs (2018) reported the evidence for alignment of stellar spins in the open cluster, Praesepe.

Bimodality of the alignment or non-alignment possibly arises from the difference in the physical properties of parent clouds, but the apparent alginment might be caused by the systematics inherent in the methods for the analyses. Mosser et al. (2018) revisited the previous analyses of red giants including all stars in Corsaro et al. (2017), and they did not reproduce excess of low stellar inclinations in NGC 6819 and 6791 reported in Corsaro et al. (2017). They ascribed this discrepancy to the very narrow ranges of priors for the Bayesian analysis adopted in Corsaro et al. (2017), and the estimated values unexpectedly favors solutions with the low stellar inclinations leading to the apparent alignment. On the other hand, Kamiaka et al. (2018) suggested that the spectroscopic measurements of $v_\star \sin i_\mathrm{s}$ can be overestimated by macroturbulence typically being ignored in the analyses, and these systematics might account for the alignment with large stellar inclinations claimed in Kovacs (2018).

Although their finding and methodologies turned out to be unreliable or at least should be revisited (Mosser et al., 2018; Kamiaka et al., 2018), their results encouraged for the further studies to understand the origins of alignment. Corsaro et al. (2017) attributed it to the initial rotation of the parent clouds of open clusters. Specifically, using hydrodynamical simulations, they showed that if the more than half of the kinetic energy is rotational energy, the observational alignment is reproduced. In the similar manner, Rey-Raposo & Read (2018) simulated the hydrodynamical evolution of molecular clouds extracted from galactic simulations down to a scale of 0.1 pc, and they found the strong alignment among protocores in the clouds. These results show that the alignment among stellar spins might be related to the initial rotation of the clouds. In reality, however, the competition among the global rotation, turbulence and magnetic field in star-forming regions would be largely complex, and it is not trivial to connect the simulations to the observations.

One possible extension of search for alignment is search for alignment in difference scales. Proto-planetary disks reside in between stars and molecular clouds, so it might contain the direct information of the star formation rather than stars. In addition, observational properties of star-forming regions (e.g. magnetic fields, velocity fields, density) can be used to interpret the origins of possible alignment among disks in the regions. Fortunately, there are several intensive surveys for proto-planetary disks by ALMA, so we can exploit the observations to study the alignment further.

In summary, the alignment among stellar rotations give us a unique probe to connect the global molecular clouds to each stellar components. The alignment, if exists, is apparently inconsistent with the turbulent origins of angular momentum, and it poses a question to the current understanding of the angular momentum evolution, so the further investigation is rewarding. In Chapter 4, we attempt to search for alignment using proto-planetary disks.

2.4 Summary

In this section, we overview the current observational knowledge of the exoplanetary systems, most of which do not exist in the Solar System implying the diversity in extrasolar

world as well as the observational limitations of the current instrument. These striking observational findings also enforce the modification of planetary formation, which previously did not care about the new types of planets (e.g. Hot Jupiter). Until now, there have been over detected 4000 exoplanets, and the next step would be the observational characterization of the systems via measurements of planetary density, populations, and atmospheres. In addition, search for analogs of rings, moons, and Earth in the exoplanetary systems would be indispensable for consistently explaining the planetary formation.

On the other hand, the planetary systems are originated from the molecular clouds, so correct understanding and knowledge of the star formation directly gives the foundations of planetary formation as well. One of the key concepts in physics is the angular momentum conservation, but this law apparently prohibits the formation of the stars unless we consider the significant extraction of the angular momentum. One possible origin of angular momentum is the turbulent motions, which predict the random orientations of the stellar rotations, and this hypothesis can be tested by investigating the spatial correlations among stellar angular momentum. Previous studies claimed the detection of alignment, but the significance is still controversial.

Any piece of observational evidence is vitally important to correctly understand the real physics to finally tackle the problem of unveiling the planetary formation from beginning to end. Given this in mind, we specifically focus on three specific topics on the observational characterization of the systems: the systematic search for exoplaneary rings using the Kepler light curves, formulating the methodology for global mapping of an Earth analog, and quest for alignment among disk orientations using the ALMA observation. These themes look independent and irrelevant to each other, but they will commonly contribute to an unified understanding of the planetary formation.

Chapter 3

Systematic Search for Rings around *Kepler* Planet Candidates: Constraints on Ring Size and Occurrence Rate

A bunch of exoplanets have been discovered, and one of the next steps will be the detection of an exoplanetary ring. Indeed, the photometric accuracy of the Kepler satellite potentially allows for the detection of rings around transiting planets, but there has been no report of the confirmed ringed planet in spite of several attempts (e.g. Barnes & Fortney, 2004; Ohta et al., 2009; Heising et al., 2015; Aizawa et al., 2017; Lecavelier des Etangs et al., 2017). The important lesson learned from early attempts, however, is the encouraging fact that the detection of rings around exo-planets, if any, is close to within reach even though not yet easy obviously. Therefore we decide to extend our previous search to all *Kepler* transiting planets with sufficiently high photometric accuracy in their short-cadence data.

More specifically, we select 168 *Kepler* planet candidates with high signal-to-noise ratios using the short-cadence data, so that we are able to probe tiny and short-duration characteristic signatures of rings. Because of those selection criteria, majority of our targets turned out to be short-period planets. Thus our survey is preferentially designed for rocky, instead of icy, rings in practice, but we can test the robustness of possible ring signatures at separate transit epochs. From this point of view, the present work is very complementary to our previous work (Aizawa et al., 2017), and regarded as a significant extension of Heising et al. (2015).

While we believe that some fraction of exoplanets should accompany rings, the required condition and the nature of those rings are largely unknown both theoretically and observationally. Even though we have not identified any candidate for a ringed planet in the analysis of the present chapter, we found several cases that mimic signature of rings, which are useful examples of false-positives for future ring searches. Also we are able to constrain the ring parameters from our null results for the targets. Our statistical and observational constraints would add insights into the origin and evolution of rings in a

completely different environment than those in our Solar system. The approach of our current methodology will eventually answer the question to what extent our Solar system is a typical (or atypical) planetary system in the Galaxy, hopefully affirmatively.

The rest of the chapter is organized as follows. Section 3.1 describes our selection of target planets. Section 3.2 explains the data reduction and analyses of lightcurves with transiting ringless or ringed planets in detail. Section 3.3 presents the results and implications of our analysis. Finally, Section 3.4 concludes and discusses the future prospects for exoplanetary ring search.

3.1   Target selection

Since signatures of planetary rings are tiny, we have to carefully select target systems with sufficient signal-to-noise ratios for detailed analysis before performing a time-consuming individual analysis. We adopt the signal-to-noise ratio (S/N) of transiting systems as a measure of a rough potential detectability of their rings:

$$(S/N) = \sqrt{\frac{T_{\mathrm{obs}}}{P_{\mathrm{orb}}}} \frac{\delta_{\mathrm{TD}}}{\sigma_{\mathrm{TD}}}. \tag{3.1}$$

In the above equation, T_{obs} is the total duration of the observed lightcurve in the short-cadence data (1 month $\leq T_{\mathrm{obs}} \leq$ 4 years), P_{orb} and δ_{TD} denote the the orbital period and transit depth, and finally σ_{TD} is the effective uncertainty of the data on the transit depth. To estimate σ_{TD}, we interpolate or extrapolate the photometric uncertainty corresponding to the transit duration τ_{TD} using values of the robust root-mean square (RMS) combined differential photometric precision (CDPP) in the *Kepler* Stellar Table.

In the present chapter, we focus on the *Kepler* short-cadence (1 min) data alone. The long-cadence data (29.4 mins) are not suitable for searching for signatures of rings, which are identifiable only for short timescales around the egress and ingress of the transit. We first retrieve parameters from the Q1–Q17 Data Release 25 catalog of all *Kepler* Objects of Interests (KOIs) (Thompson et al., 2018), and calculate (S/N) of those KOI planets that have short-cadence data. We exclude the systems whose dispositions are "FALSE POSITIVE" in the catalog.

The total duration T_{obs} corresponds to the observed duration of the system in the *Kepler* short-cadence data. Roughly speaking, $(S/N) = 1$ corresponds to the 1σ-detection of the transit of a planet, not of a planetary ring. Since a typical amplitude of the photometric anomaly due to a Saturnian ring is less than 1 percent of the planetary transit depth, we select all *Kepler* planet candidates with $(S/N) > 100$ as our targets.

Orbital periods and planetary radii of all 4029 KOIs with short-cadence data are shown in Figure 3.1. The majority of the KOI planets have insufficient (S/N) to detect possible rings, and 168 KOI planets satisfy $(S/N) > 100$ (plotted in red circles). We note that our targets include all systems in Heising et al. (2015) except for KOI-398.02 with $(S/N) = 97.1$ (20 out of 21).
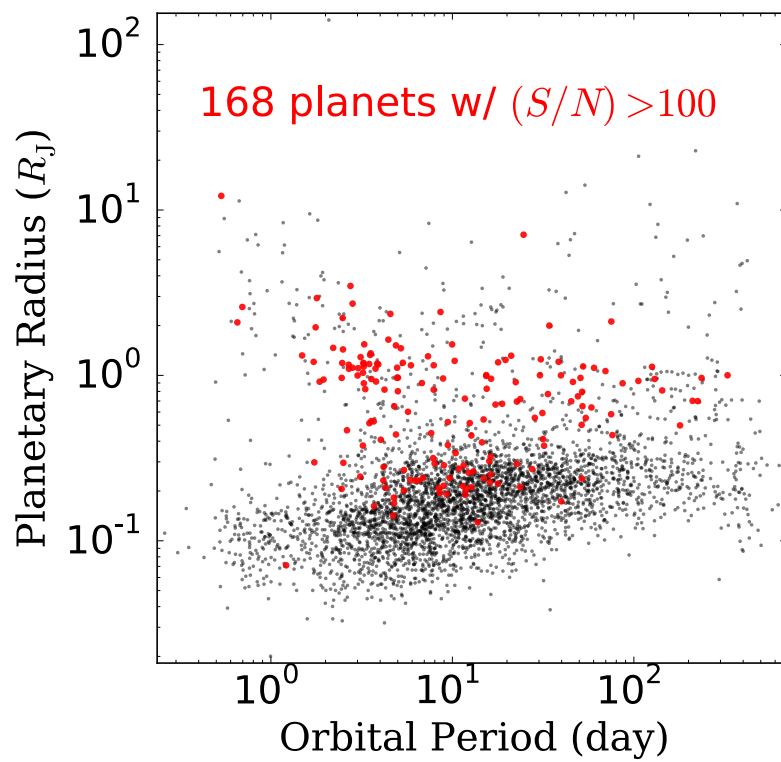
Figure 3.1 Planetary radii of 4029 KOIs against their orbital periods. Red points indicate the 168 targets with $(S/N) > 100$ that are examined closely in the present chapter.

3.2 Ring survey method: data reduction and fits of ringless and ringed planet models

This section describes our analysis method of ring survey, including lightcurve data reduction and fit to the parametrized templates of a planet with and without a planetary ring. The method is largely based on our previous paper Aizawa et al. (2017), and the brief description is summarized in Section 2.2.2.1. We adopt the stellar intensity profile with quadratic limb-darkening in Eq (2.5). Throughout the present analysis, we adopt the circular orbit of all the planets for simplicity, and we our ringless planet model is specified by seven parameters: the planet to star radius ratio $R_{\rm p}/R_{\star}$, the impact parameter b, the semi-major axis normalized by the stellar radius $a/R_{\star}$, the time of a transit center t_0, limb-darkening parameters q_1 and q_2, and the normalizing factor of the light curve c.

Our ring model is specified by additional five parameters; inner ring radius $R_{\rm in}$, outer ring radius $R_{\rm out}$, shading rate T, and orientation angles for ring axes θ and ϕ. If $T = 1$, a ring is fully opaque, and if $T = 0$, the ring is completely transparent. To increase the efficiency of numerical fitting, we employ $r_{\rm out/in} = R_{\rm out}/R_{\rm in}$ and $r_{\rm in/p} = R_{\rm in}/R_{\rm p}$, instead of $R_{\rm out}$ and $R_{\rm in}$. Thus our ringed planet model is specified by 12 parameters in total. Further details of the model are found in Section 2.2.2.1 and Aizawa et al. (2017).

3.2.1 Making phase-folded lightcurves

If a transiting planet has a ring, the ring signature should be imprinted equally in each lightcurve at different transit epochs. Since, the ring parameters, in particular the orientation angles of the ring, are supposed not to vary for the timescale of $T_{\rm obs}$, the signal-to-noise ratio of the signature should increase by stacking all the lightcurves properly. To produce such precise phase-folded lightcurves requires an accurate determination of both the transit center and baseline of each lightcurve at different transit epochs.

We use the short-cadence Pre-search Data Conditioned Simple Aperture Photometry (PDC-SAP) fluxes of the target objects from the Mikulski Archive for Space Telescopes (MAST). We adopt the transit model $F(t)$ implemented by the Pytransit package (Parviainen, 2015) for transiting ringless planets, which generates the lightcurve based on the model of Mandel & Agol (2002) with the quadratic limb darkening law.

We first apply the ringless model separately to each transit by varying the transit centers and baseline functions alone. Here, we take the fourth-order polynomials as the baseline functions, and we retrieve the transit duration and the other parameters of transiting planets from the MAST pipeline with the help of the Python interface *kplr* (http://dan.iel.fm/kplr/). We extract the lightcurve during the epoch of ± 2 times the transit duration with respect to each transit center for the subsequent analysis.

After fitting, we exclude outliers exceeding 5σ amplitude in the flux so as to determine the baseline of the lightcurve accurately. We repeat the fitting procedure and removal of outliers until no outliers are left. Then we visually check each transit in order to exclude inappropriate transits that may be strongly affected by instrumental systematics.

Several transits exhibit large transit timing variations, which our pipeline cannot automatically deal with. In such cases, we appropriately choose the initial transit centers before fitting so as to correctly identify the transits. Finally, we obtain the best baseline using the out-of-transit (outside $\pm0.6\times$ transit duration around the transit center) data alone, and normalize the lightcurve with the fitted baseline. Our fit to the transit model lightcurve is performed with the public code *mpfit* (Markwardt, 2009) that is based on the Levenberg-Marquardt (LM) algorithm.

We stack the obtained normalized lightcurve at each transit, and make the phase-folded lightcurve. We derive the transit duration by applying the ringless model to the phase-folded lightcurve. With the updated transit duration, we repeat the above procedure to obtain the final phase-folded lightcurve.

We extract the phase-fold lightcurve during an epoch within ±1 transit duration around the transit center. To finish the fitting procedures in realistic time, the lightcurve is divided into 500 bins with an equal time interval. Here, we require one bin to accommodate at least 10 points to guarantee the appropriate binning. So, for systems with the number of the phase-folded data less than 5000, we choose the bin width for one bin to have 10 data points.

Finally, we have phase-folded lightcurves for 168 planets, which are analyzed for ring search in the next subsection.

3.2.2 Separate fitting to planetary solutions with and without a ring

Our search for ring signatures is based on the comparison between the separate best solutions for a planet with and without a ring for all our targets.

In order to find the best solution in the 7 parameter space for a ringless planet model, we randomly generate 1000 different initial sets of parameters from the homogeneous distribution in a finite range. Then, we use the LM method to find the local minima starting from each of initial values, and we choose the best solution among the solutions. In fitting, we use the binned data that are produced in Section 3.2.1. We confirm that generally 100 initial sets of parameters are sufficient to find the minimum for our purpose.

Finally, we calculate the chi-squared value:

$$\chi^2_{\mathrm{ringless}} = \sum_{\mathrm{i}}([d(t_{\mathrm{i}}) - m(t_{\mathrm{i}})]/\Delta d(t_{\mathrm{i}}))^2 \tag{3.2}$$

from the binned data. Here, $d(t_{\mathrm{i}})$, $m(t_{\mathrm{i}})$, and $\Delta d(t_{\mathrm{i}})$ are the observed flux, the expected flux of the model, and the uncertainty in observed flux at $t = t_{\mathrm{i}}$, respectively. We assume $\Delta d(t_{\mathrm{i}})$ to be a standard deviation of the normalized flux of each lightcurve estimated from its out-of-transit epoch.

The same procedure is performed for a ringed planet model. In this case, we have 12 free parameters t_0, b, R_{p}, $r_{\mathrm{out/in}}$, $r_{\mathrm{in/p}}$, θ, ϕ, T, $a/R_{\star}$, c, q_1 and q_2. We calculate the chi-squared value χ^2_{ring}, which has the definition similar to $\chi^2_{\mathrm{ringless}}$.

One fit of the ringed model takes about a few minutes in a lap-top, and the fits to the entire datasets were carried out with PC clusters in The Center for Computational Astrophysics (CfCA) in National Astronomical Observatory, Japan.

3.2.3 Searching for ring signatures via comparison between ringless and ringed planet models

Our next procedure is to create a list of tentative ringed-planet candidates from the comparison between the best-fit values for the two models, $\chi^2_{\text{ringless, min}}$ and $\chi^2_{\text{ring, min}}$. Specifically for this purpose, we adopt a *F*-test with *F* statics (e.g. Lissauer et al., 2011), and define

$$F_{\text{obs}} = \frac{(\chi^2_{\text{ringless, min}} - \chi^2_{\text{ring, min}})/(N_{\text{ring}} - N_{\text{ringless}})}{\chi^2_{\text{ring, min}}/(N_{\text{bin}} - N_{\text{ring}} - 1)}, \tag{3.3}$$

where N_{bin} is the number of in-transit bins of the phase-folded lightcurve (typically 500), and $N_{\text{ring}} = 12$ and $N_{\text{ringless}} = 7$ are the number of free parameters in the planetary models with and without a ring, respectively.

The numerator of the right-hand side of Eq. (3.3) corresponds to the improvement in χ^2 of the ring model divided by the number of the additional degrees of freedom characterizing a ring. The denominator is the χ^2 per degree of freedom for the ringed model. Thus, F_{obs} represents a measure of relative improvement of the fit by introducing the ring. The large F_{obs} prefers the ringed planet model. Note, however, that F_{obs} is defined simply through the ratio of the minimum values of χ^2 for the two models. Therefore it is nothing to do with the goodness of the fit for either model, which needs to be checked separately.

According to the *F*-test, the measure of the the null hypothesis that our ringed model does not improve the fit relative to the ringless model is given by the *p*-value defined as

$$p = 1 - \int_0^{F_{\text{obs}}} F(f|N_{\text{bin}} - N_{\text{ring}} - 1, N_{\text{ring}} - N_{\text{ringless}})\,\mathrm{d}f, \tag{3.4}$$

where $F(f|N_{\text{bin}} - N_{\text{ring}} - 1, N_{\text{ring}} - N_{\text{ringless}})$ is the *F*-distribution with the degrees of freedom $(N_{\text{bin}} - N_{\text{ring}} - 1, N_{\text{ring}} - N_{\text{ringless}})$.

The larger value of F_{obs}, therefore the smaller value of p disfavors the null assumption, i.e., the ringed model better fits the data than the ringless model. In this chapter, we adopt the condition of $p < 0.05$ for the rejection of the null hypothesis. For those tentative candidates of ringed planets, we attempt to understand the origins of anomalies by examining individual lightcurves and statistics (e.g. $\chi^2_{\text{ring, min}}$) further.

We also test the robustness of possible ring signatures by dividing the multiple transits into those at even and odd transit numbers, creating the phase-folded lightcurves separately, and computing the *p*-values ($p_{\text{even}}, p_{\text{odd}}$). Unlike the other analyses, we use the non-binned data here in order to evade the additional uncertainties in the lightcurves due to the extra binning step, especially for systems with the low number of the data. For the calculation of ($p_{\text{even}}, p_{\text{odd}}$), we approximate the best-fit model of the binned data as that of the non-binned data, and then we calculate F_{obs} in Eq (3.3) for non-binned

data. If rings mainly account for signals in lightcurves, we expect p_{even} to be close to p_{odd} because of the consistency of the signals.

Finally, we comment on the validity of applying the *F*-test to our ring search. The *F*-test needs to satisfy two conditions (e.g. Protassov et al., 2002). One is that the two models are nested in a sense that the more complicated model reduces to the simpler one if the additional parameters in the former model are removed. This is trivially satisfied in the present case. The other condition is that the simpler model should not be located at the edge of the parameter space of the more complicated model. Strictly speaking, this condition may not hold because our ring model reduces to the ringless model in the limit of $R_{\mathrm{out}} \to R_{\mathrm{p}}$. Nevertheless, *F*-test gives us a practically useful criterion, and we decide to use it in selecting tentative candidates for further analysis.

3.2.4 Obtaining upper limits on the outer radius of a ring

Even for planetary systems without any detectable signatures of a ring, we may constrain the property of a possible ring within the observational detection limit. To proceed realistically, we need to reduce the number of free parameters charactering the ring. Thus we fix the inner radius of the ring as $R_{\mathrm{in}} = R_{\mathrm{p}}$, and set the opacity of the ring as $T = 1$ just for simplicity. Furthermore, we focus on two cases for the orientation angles of the ring as we describe in the next subsections. Thus we are left with a single parameter, the outer radius of the ring R_{out}. In practice, we place upper limits on the ratio $R_{\mathrm{out}}/R_{\mathrm{p}}$ from the fit to the lightcurves.

3.2.4.1 Timescale for tidal alignment of planetary ring

The deviation of the lightcurve due to a ring relative to a ringless planet model prediction crucially depends on the size, opacity and orientions of the ring. In turn, a useful constraint on the size of the ring is placed only if the orientation of the ring is well specified. The ring axis is most likely aligned with the planetary spin axis. In the case of close-in planets as we mainly consider in the present chapter, the planetary spin axis is expected to be tidally aligned with that of the planetary orbit. Therefore the ring axis in such tidally aligned systems can be specified physically.

The damping timescale, which is comparable to the spin-orbit synchronization timescale, is given by

$$t_{\mathrm{damp}} \simeq \frac{2CQ_{\mathrm{p}}}{3k_{\mathrm{p}}} \left(\frac{M_{\mathrm{p}}}{M_{\star}}\right) \left(\frac{a}{R_{\mathrm{p}}}\right)^3 \left(\frac{P_{\mathrm{orb}}}{2\pi}\right), \tag{3.5}$$

(e.g. Schlichting & Chang, 2011). In the above equation, a is the semi-major axis of the planetary orbit, R_{p} is the planetary radius, P_{orb} is the planetary orbital period, M_{p} is the planetary mass, $M_{\star}$ is the stellar mass, C is the dimensionless moment of inertia of the planet (i.e., divided by $M_{\mathrm{p}}R_{\mathrm{p,eq}}^2$ with $R_{\mathrm{p,eq}}$ being the equatorial radius of the planet), Q_{p} is the tidal dissipation function of the planet, and k_{p} is the Love number.

We estimate t_{damp} for our target systems using the parameters from the Q1–Q17 Data Release 25 catalog of KOIs (Thompson et al., 2018), and list the values in Tables 3.1 to

3.3. In doing so, we adopt typical values of $Q_{\mathrm{p}} = 10^{6.5}$, $C = 0.25$, and $k_{\mathrm{p}} = 1.5$. The adopted value of Q_{p} is supposed to be typical for gas giants, but that for rocky planets would be substantially smaller. Thus the values listed in Tables 3.1 to 3.3 would be significantly over-estimated for rocky planets.

For the majority of systems, the planetary mass M_{p} is not directly measured. Thus we adopt Eq. (8) of Weiss et al. (2013), and rewrite it as

$$\frac{M_{\mathrm{p}}}{M_{\oplus}} = 0.337 \left(\frac{R_{\mathrm{p}}}{R_{\oplus}}\right)^{1/0.53} \left(\frac{F}{\mathrm{ergs^{-1}cm^{-2}}}\right)^{0.03/0.53}, \tag{3.6}$$

where $M_{\oplus}$ and $R_{\oplus}$ are the mass and radius of Earth, and F is the incident flux of the host star received at the location of the planet:

$$F = \frac{\sigma_{\mathrm{SB}} T_{\mathrm{eff}}^4 R_{\star}^2}{4\pi a^2}, \tag{3.7}$$

with σ_{SB} is the Stefan-Boltzmann constant. For example, if we consider the Hot Jupiter (a=0.05 AU) around the Sun, we obtain $F = 5.46 \times 10^8$ ergs^{-1}cm^{-2}.

We compute M_{p} from R_{p} in the Kepler catalog for 155 systems. According to Eq. (3.6), the remaining 13 systems have $M_{\mathrm{p}} > M_{\mathrm{J}}$ and we set $M_{\mathrm{p}} = M_{\mathrm{J}}$ for such systems, since Eq. (8) of Weiss et al. (2013) cannot be applied for that range. Because we use the values of M_{p} only in computing their t_{damp}, that simple estimate does not change our result.

3.2.4.2 Aligned with the planetary orbit

Under the strong tidal interaction with the star, the ring becomes aligned to the orbital plane of the planet. Indeed Brown et al. (2001) gave the upper limit on the ring size of a Hot Jupiter, HD 209458 b, as $1.7R_{\mathrm{p}}$ assuming the alignment.

In a similar manner, we place upper limits on the ring size assuming the tidal alignment. The tidal alignment leads to the orientation of $\theta = \arcsin(b/(a/R_{\star}))$ and $\phi = 0$. In addition, the small value of θ enhances the effective optical depth viewed from the observer, relative to that from the top-view. Thus, we assume $T = 1$ even though rings can be very thin like Jupiter's rings.

In summary, we fix $\phi = 0°$, $\theta = \arcsin(bR_{\star}/a)$, $T = 1$, and $R_{\mathrm{in}} = R_{\mathrm{p}}$ for fitting. Assuming these conditions, we fit the ringed model to the data using at least 100 sets of randomly chosen initial parameters, and we pick up the best solution among the local optimum solutions.

After obtaining the best solutions with fixed values of $R_{\mathrm{out}}/R_{\mathrm{p}}$, we define the 3σ limit $(R_{\mathrm{out}}/R_{\mathrm{p}})_{\mathrm{upp}}$ where

$$\Delta\chi^2(R_{\mathrm{out}}/R_{\mathrm{p}}) \equiv (\chi^2_{\mathrm{ring, \, min}}(R_{\mathrm{out}}/R_{\mathrm{p}}) - \chi^2_{\mathrm{ringless, \, min}})/(\chi^2_{\mathrm{ringless, \, min}}/\mathrm{dof}) \tag{3.8}$$

becomes 9. In practice, we compute $\Delta\chi^2(R_{\mathrm{out}}/R_{\mathrm{p}})$ at 11 values of $R_{\mathrm{out}}/R_{\mathrm{p}}$: 1.1, 1.3, 1.5, 2.0, 2.5, 3.0, 4.0, 5.0, 6.0, 8.0, and 10.0. Then we interpolate them to find $(R_{\mathrm{out}}/R_{\mathrm{p}})_{\mathrm{upp}}$.

Our procedure to setting the upper limit is illustrated in Figure 3.2 for KOI–97.01. In this example, the interpolated curve crosses the $\Delta\chi^2 = 9$ threshold at $R_{\mathrm{out}}/R_{\mathrm{p}} = 1.55$. Thus we obtain $(R_{\mathrm{out}}/R_{\mathrm{p}})_{\mathrm{upp, Aligned}} = 1.55$ for KOI–97.01. Figure 3.3 plots three corresponding fitting curves with $R_{\mathrm{out}}/R_{\mathrm{p}} = 1.5$, 2.0, and 2.5 along with the curve of the ringless model.

If $\Delta\chi^2 < 9$ for $R_{\mathrm{out}}/R_{\mathrm{p}} = 10.0$, we do not place upper limits $(R_{\mathrm{out}}/R_{\mathrm{p}})_{\mathrm{upp}}$. These cases are marked as $-$ in Tables 3.1 to 3.3 below.

The alignment condition is determined by the tidal dissipation function Q_{p} and the Love number k_{p}, the planet/star mass ratio, the dimensional moment of the inertia of the planet C, the orbital period P_{orb}, and the normalized semi-major axis $a/R_\star$. As discussed in Appendix A, 154 out of the 168 planetary systems are supposed to become aligned within a timescale of 1Gyr, if we adopt a fiducial values, $Q_{\mathrm{p}} = 10^{6.5}$, $k_{\mathrm{p}} = 1.5$, $C = 0.25$, and the mass-radius relation (Eq (8) in Weiss et al. (2013)). We compute the upper limit on $R_{\mathrm{out}}/R_{\mathrm{p}}$ for all 168 systems in any case even if their alignment timescale is long.
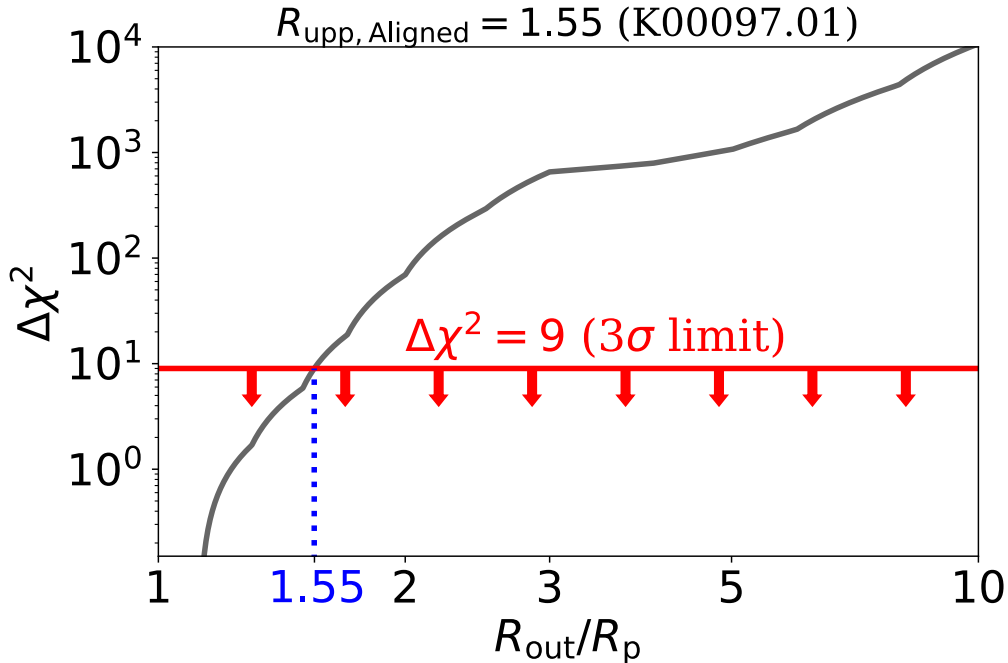
Figure 3.2 An example illustrating how to set an upper limit on $R_{\mathrm{out}}/R_{\mathrm{p}}$. Black curve shows $\Delta\chi^2$, eq.(6), of an aligned ring model for KOI-97.01. The value of $R_{\mathrm{out}}/R_{\mathrm{p}} = 1.55$ where $\Delta\chi^2 = 9$ is defined as our $(R_{\mathrm{out}}/R_{\mathrm{p}})_{\mathrm{upp, Aligned}}$.

3.2.4.3 Orientation of the Saturnian ring

As another model for the ring orientation, we simply adopt the Saturnian case $\phi = 0°$ and $\theta = 26.7°$, in addition to $T = 1$ and $R_{\mathrm{in}} = R_{\mathrm{p}}$ as before. Although the values of T and R_{in} are adopted just for simplicity, the derived upper limits are mainly sensitive to
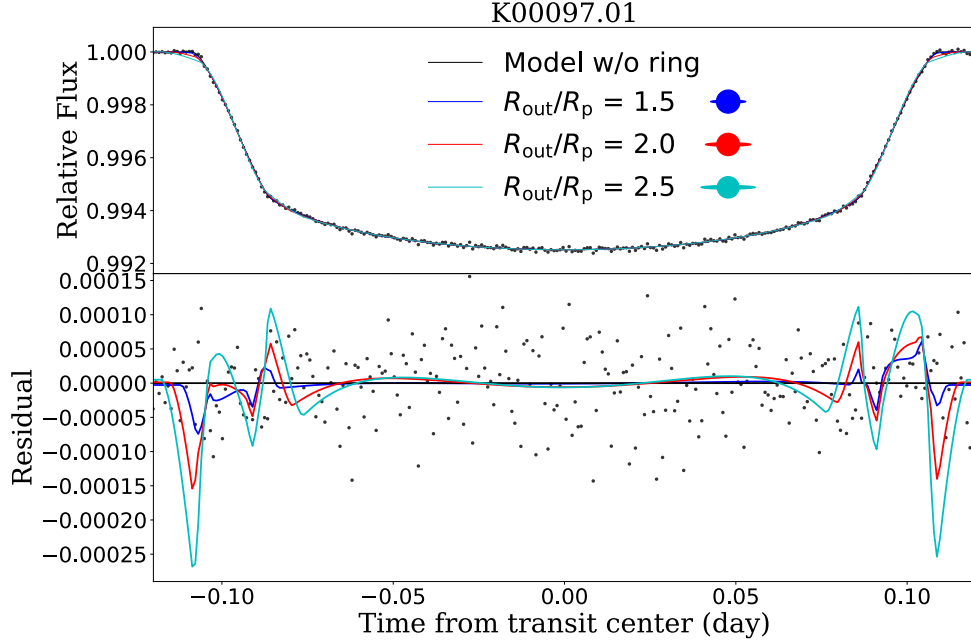
Figure 3.3 Lightcurves for KOI-97.01. Gray points are the binned data of KOI-97.01. Blue, red, and cyan curves correspond to the best-fits of the ringed model with $R_{\mathrm{out}}/R_{\mathrm{p}} = 1.5$, 2.0, and 2.5, respectively. The lower panels indicate the residuals with respect to the best-fit of the ringless model.

R_{out}, and can be scaled with the different values of T. An additional small signal due to an inner gap may be extracted if $R_{\mathrm{in}} > R_{\mathrm{p}}$, while it is not important in the present analysis (e.g Barnes & Fortney, 2004; Akinsanmi et al., 2018).

With fixed values of $R_{\mathrm{out}}/R_{\mathrm{p}}$, we search for the optimal solutions by varying other parameters in the similar manner as in Sec 3.2.4.2. In the analysis, we vary $R_{\mathrm{out}}/R_{\mathrm{p}}$ up to $1/\sin(26.7°) \simeq 2.22$, above which a shape of an assumed ring is not distinguishable from an oblate planet with the same oblateness. Practically, we use 8 fixed values of $R_{\mathrm{out}}/R_{\mathrm{p}}$: 1.1, 1.2, 1.3, 1.4, 1.6, 1.8, 2.0, and 2.22. Then, we obtain the 3σ limit $(R_{\mathrm{out}}/R_{\mathrm{p}})_{\mathrm{upp, Saturn}}$ by interpolating the values of $\{R_{\mathrm{out}}/R_{\mathrm{p}}, \Delta\chi^2(R_{\mathrm{out}}/R_{\mathrm{p}})\}$. If $\Delta\chi^2 < 9$ for $R_{\mathrm{out}}/R_{\mathrm{p}} = 2.22$, we do not give the upper limits $(R_{\mathrm{out}}/R_{\mathrm{p}})_{\mathrm{upp, Saturn}}$.

In addition to the limits on $R_{\mathrm{out}}/R_{\mathrm{p}}$, we also place upper limits on the ratio of the outer radius of the ring and the stellar radius, $(R_{\mathrm{out}}/R_\star)_{\mathrm{upp}}$. Qualitatively this is simply given by $(R_{\mathrm{out}}/R_{\mathrm{p}})_{\mathrm{upp}} \times (R_{\mathrm{p}}/R_\star)_{\mathrm{ringless}}$, but not exactly because the best-fit planet radius may be different if the ring model is assumed instead. To evaluate $(R_{\mathrm{out}}/R_\star)_{\mathrm{upp}}$ correctly, we estimate $R_{\mathrm{p}}/R_\star$ corresponding to $(R_{\mathrm{out}}/R_{\mathrm{p}})_{\mathrm{upp, Saturn}}$ by interpolating the values of $\{R_{\mathrm{p}}/R_\star, (R_{\mathrm{out}}/R_{\mathrm{p}})_{\mathrm{upp, Saturn}}\}$. Then, we obtain $(R_{\mathrm{out}}/R_\star)_{\mathrm{Saturn,upp}} = (R_{\mathrm{out}}/R_{\mathrm{p}})_{\mathrm{upp, Saturn}} \times (R_{\mathrm{p}}/R_\star)$ using the interpolated values. For simplicity, we only give $(R_{\mathrm{out}}/R_\star)_{\mathrm{upp}}$ for systems with $(R_{\mathrm{out}}/R_{\mathrm{p}})_{\mathrm{upp, Saturn}}$.

Incidentally the damping timescales of the 13 systems with $p < 0.001$ turned out to be significantly less than 1 Gyr except for KOI-868. Thus the possible rings for the 12 systems are likely to be aligned with the planetary orbital plane. Thus we do not compute

$(R_{\rm out}/R_{\rm p})_{\rm upp, \, Saturn}$ for all the systems with $p < 0.001$.

3.3 Result of the ring survey

3.3.1 No Convincing Candidate for a Ringed Planet

We have performed a ring search following the method described in Section 3.2. The result for all the 168 Kepler objects is summarized in Tables 3.1 to 3.3.

We identify 29 candidate objects with p-values less than the threshold value of 0.05. For most of these systems, the ring model yields $\chi^2_{\rm ring}/{\rm dof} \sim 1$ (Figure 3.4). However, after inspecting individual lightcurves of these systems, we conclude that none of them is a viable candidate for a ringed planet. The 11 of the 29 candidates do not exhibit any convincing ring-like signatures in the lightcurves, and so are excluded. The other 18 systems do show anomalous features in the lightcurves, but they are most likely ascribed to other mechanisms: gravity darkening (2 systems), spot-crossing (9 systems), disintegration of a planet (1 system), artifacts generated during the folding process (3 systems), and stellar activity (3 systems) as discussed in the following.
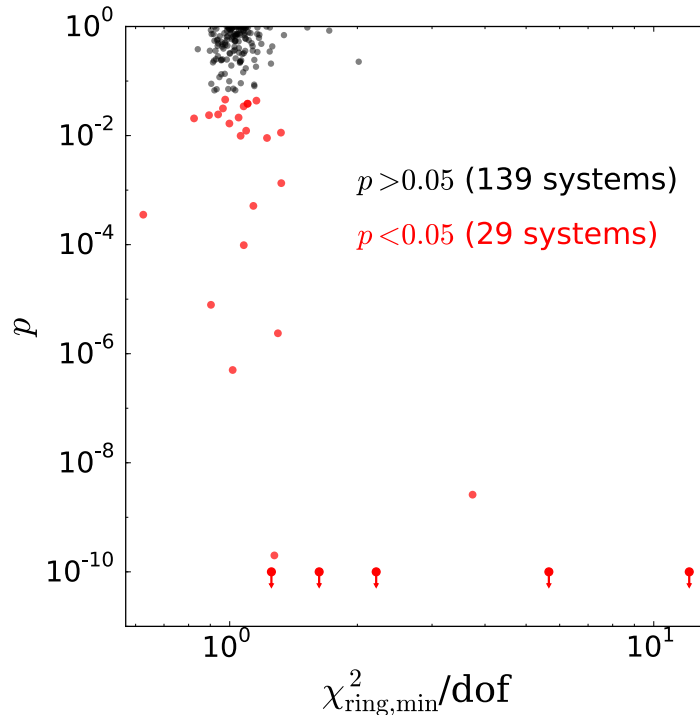
Figure 3.4 The p-values against $\chi^2/{\rm dof}$ for our 168 targets.

3.3.2 Closer consideration of individual systems with $p < 0.05$

The analysis described in Section 3.3 leaves 29 systems with $p < 0.05$. Their lightcurves are carefully examined and compared with the expected ring signature. It turned out that they are not caused by the presence of a ring. We describe the origin of those anomalies individually here. They are interesting objects themselves, and also provide useful examples of possible false-positives for future ring searches.

3.3.2.1 Gravity darkening: KOI-2.01 and 13.01

Fast rotating stars have higher (lower) effective surface temperature in the polar (equatorial) regions because of the stronger centrifugal force along the equatorial plane. Thus the transit lightcurve becomes asymmetric with respect to the central transit time depending on the path of the planet. The anomaly due gravity darkening is not confined preferentially around the ingress or egress phases unlike the ring signature (see Fig. 3.3 for example), and can be distingushed easily by eye.

Figure 3.5 shows a lightcurve of our tentative candidate KOI-13.01 (Kepler-13 b), which cannot be well fitted anyway even by adding a ring. This system was analysed first by Barnes et al. (2011), who found that the lightcurve is very well explained by gravity darkening. Masuda (2015) presented a further elaborated analysis of KOI-13 (Kepler-13), as well as another gravity darkened system, KOI-2, in our targets.
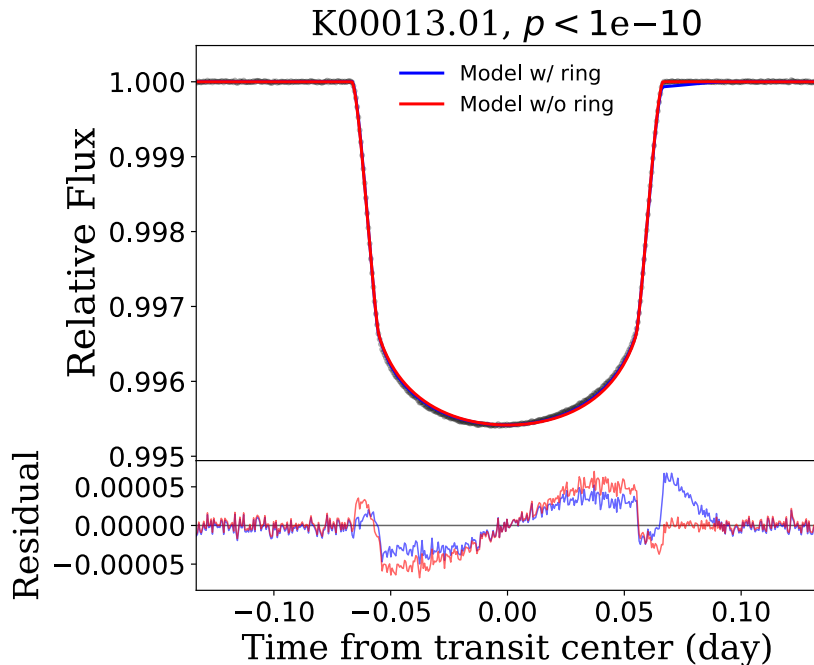
Figure 3.5 Lightcurve of a gravity darkened system, KOI-13.01 (Kepler 13 b).

3.3.2.2 Evaporation of atmosphere: KOI-3794.01

Another tentative candidate, KOI-3794.01 (KIC 12557548, *Kepler*-1520 b), is known as an evaporating planet (e.g. Rappaport et al., 2012), whose lightcurve is shown in Figure 3.6. Indeed, the transit depth of the lightcurves at different epochs (before phase-folded) exhibits significant time-variation, which is inconsistent with the ring hypothesis.
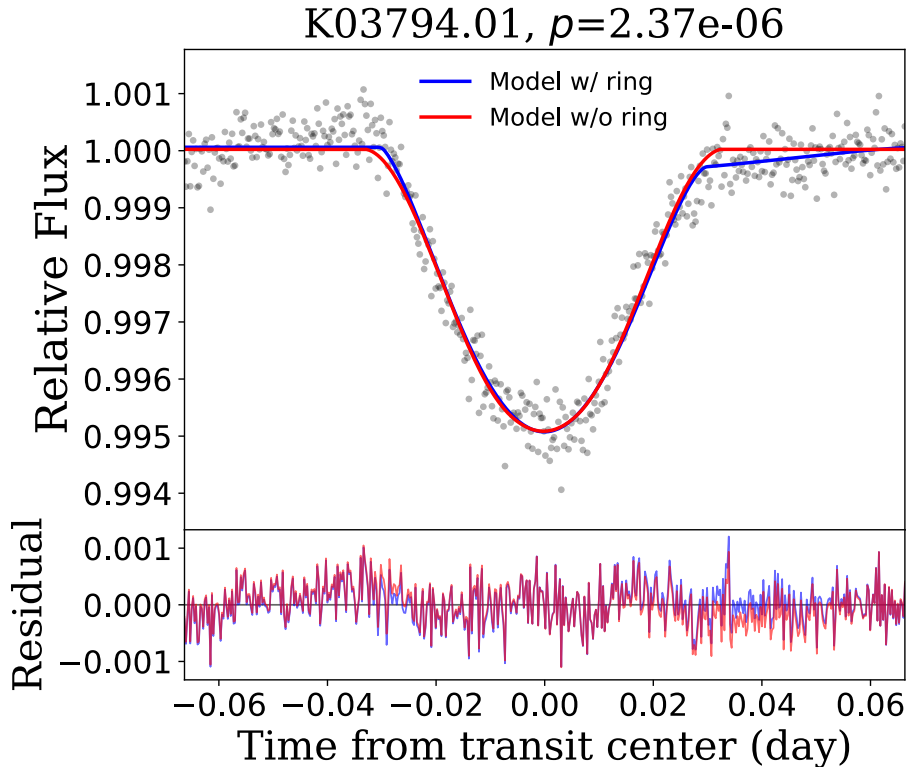
Figure 3.6 Lightcurve of an evaporating planet KOI-3794.01 (Kepler-1520 b)

3.3.2.3 Spot crossing during transit: KOI-3.01, 63.01, 676.01, 1353.01, 1416.01, 1539.01, 1714.01, 1729.01, and 6016.01

Stellar spots add non-negligible anomalous features in the transit lightcurves. Among the 29 tentative candidates with $p < 0.05$, we find that 9 systems are likely explained by spot-crossing events, not by a ring. As a significant example, we show the phase-folded lightcurve of KOI-1714.01 in Figure 3.7, where the entire flux is strongly affected by by spot-crossing events.

Spot-crossing features have been already reported for four systems out of 9 systems; KOI-3.01 (*Kepler*-3b) show frequent spot-crossing anomalies at fairly similar phases, and its planetary orbit is estimated to be misaligned relative to the stellar spin (Sanchis-Ojeda & Winn, 2011). Combining the spot anomalies and the Rossiter-McLaughlin effect of KOI-63.01 (*Kepler*-63 b), Sanchis-Ojeda et al. (2013) concluded that the system has a

large spin-orbit misalignment of $\Psi = 104°$. Also the variability of lightcurves due to spot-crossing events have been reported for KOI-676.01 (*Kepler*-210 c) by Sanchis-Ojeda et al. (2013), and for KOI-1353.01 (*Kepler*-289 c) by Schmitt et al. (2014).

The other five systems KOI-1416.01(*Kepler*-850 b), 1539.01, 1714.01, 1729.01, and 6016.01 are classified as possible false positives in *Kepler* CFOP webpages, and we confirmed that there are no ring-like signatures.
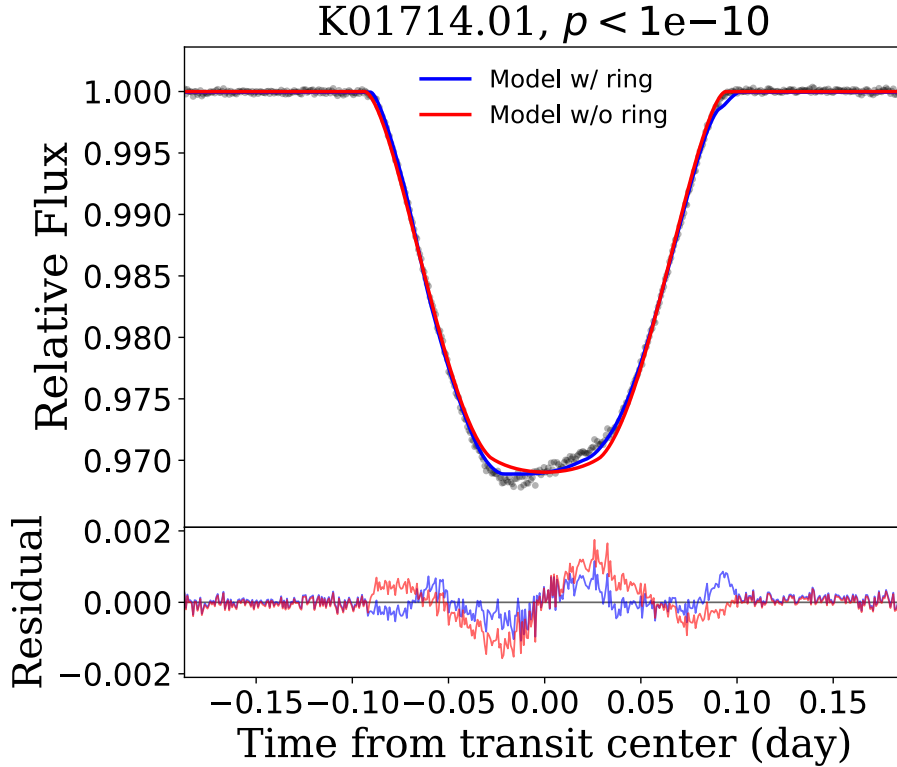
Figure 3.7 Lightcurve of a spot-crossing event, KOI-1714.01.

3.3.2.4 False anomalies due to an inaccurate choice of a transit center: KOI-70.02, 102.01, and 148.01

Phase-folded lightcurves of KOI-70.02, 102.01, and 148.01 show anomalous features around egress and ingress phases. The transit depth of those three systems is very small, and we suspect that the anomalies are simply caused by inaccurate central transit epochs in phase-folding.

Figure 3.8 shows an example for KOI-148.01. In the left panel, we show the lightcurve, which is folded as described in §3.1. As shown in the left panel, the anomalous features appear around the egress and ingress. Then, to find out the origin of the anomaly, we create a phase-folded lightcurve using a linear ephemeris. Specifically, when we fit the individual transit, we fix each transit center to $t_{cen,i} = t_{cen,0} + iP_{orb}$, where $t_{cen,i}$ is the transit center at the i-th transit. Here, we retrieve $t_{cen,0}$ and P_{orb} from the *Kepler* catalog.

The refolded lightcurve is plotted in the right panel, which show that the anomalous features disappear. We made sure that this is also the case for the other two systems, KOI 70.02 and 102.01.
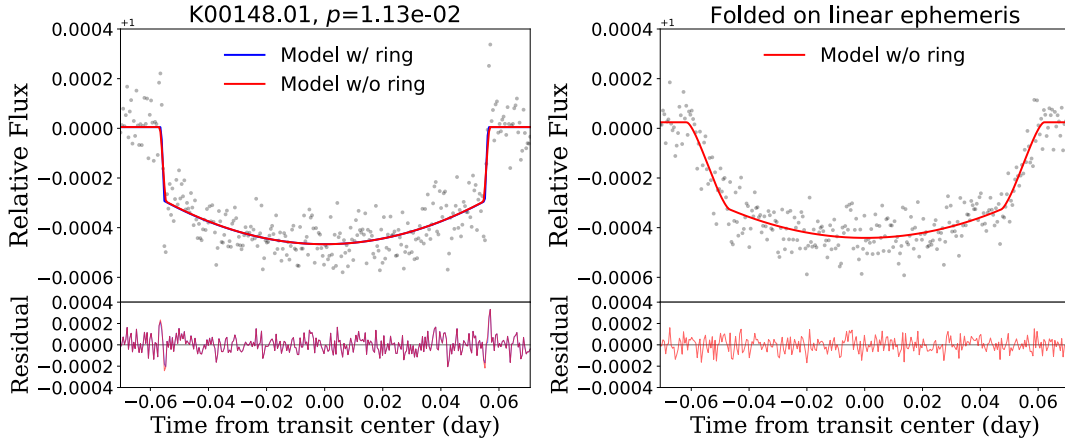
Figure 3.8 Two different phase-folded lightcurves of KOI-148.01.

3.3.2.5 Systems without statistical significance: KOI-4.01, 5.01, 212.01, 214.01, 257.01, 423.01, 433.02, 531.01, 686.01, 872.01, and 1131.01

Out of the 168 targets, we find 11 systems that marginally favor the ring model at $2 - 3\sigma$ levels: KOI-4.01, 5.01, 212.01, 214.01, 257.01, 423.01, 433.02, 531.01, 686.01, 872.01, and 1131.01. Figure 3.9 shows their lightcurves as well as the best-fit model with and without a ring (in blue and red lines, respectively)).

To examine their significance, we divide their individual transit lightcurves into two groups as described in subsection 3.2.3. If the anomaly is really caused by a ring, both p_{even} and p_{odd} should remain small.

We find that 9 systems have both of p_{even} and p_{odd} larger than 0.32 (i.e., 1σ), and two systems have both p_{even} and p_{odd} with merely 1σ significance: $(0.11, 0.12)$ for KOI-4.01 and $(0.029, 0.037)$ for KOI-257.01. Even though the two systems are likely to be statistical flukes, we examined the lightcurve visually in any case. The lightcurve of KOI-4.01 seems marginally consistent with the ring signature, but the amplitude is so tiny and can be easily produced by random noise. The features of KOI-257.01 are likely to produced by the folding procedure as we discussed in Sec 3.3.2.4 because the transit depth is so small.

We note that the rejection of the null hypothesis of a ring with the level of $p = 0.05$ implies that $168 \times 0.05 = 8.4$ systems are expected to show 2σ signals even if there is no ring at all. Thus 11 marginal systems even if there is no ring system are fairly consistent with our choice of the threshold.

Figure 3.9 Lightcurves of 11 systems without statistical significance listed in B.5

K00433.02, *p*=2.07e-02

K00531.01, *p*=2.44e-02

K00686.01, *p*=4.38e-02

K00872.01, *p*=4.57e-02

K01131.01, *p*=3.84e-02
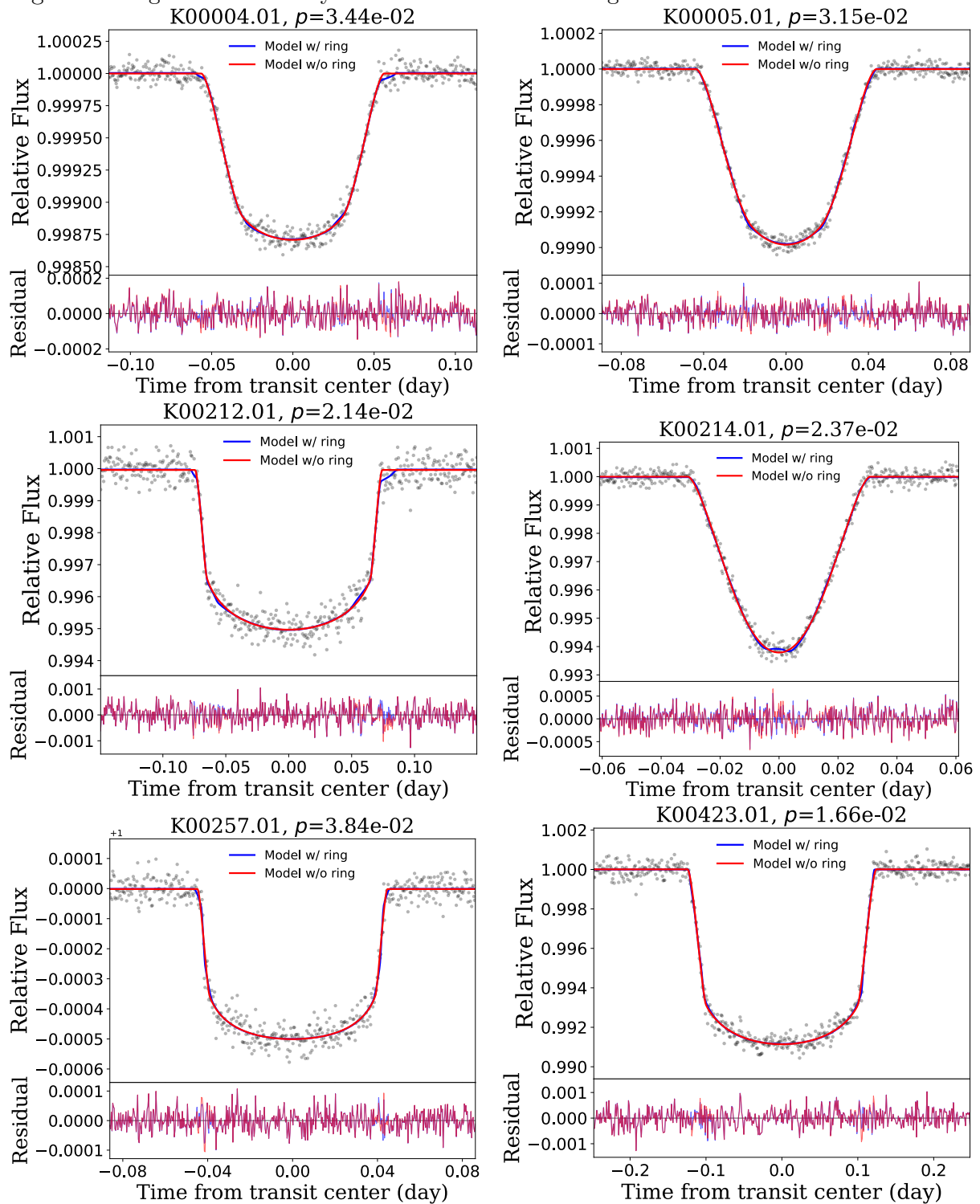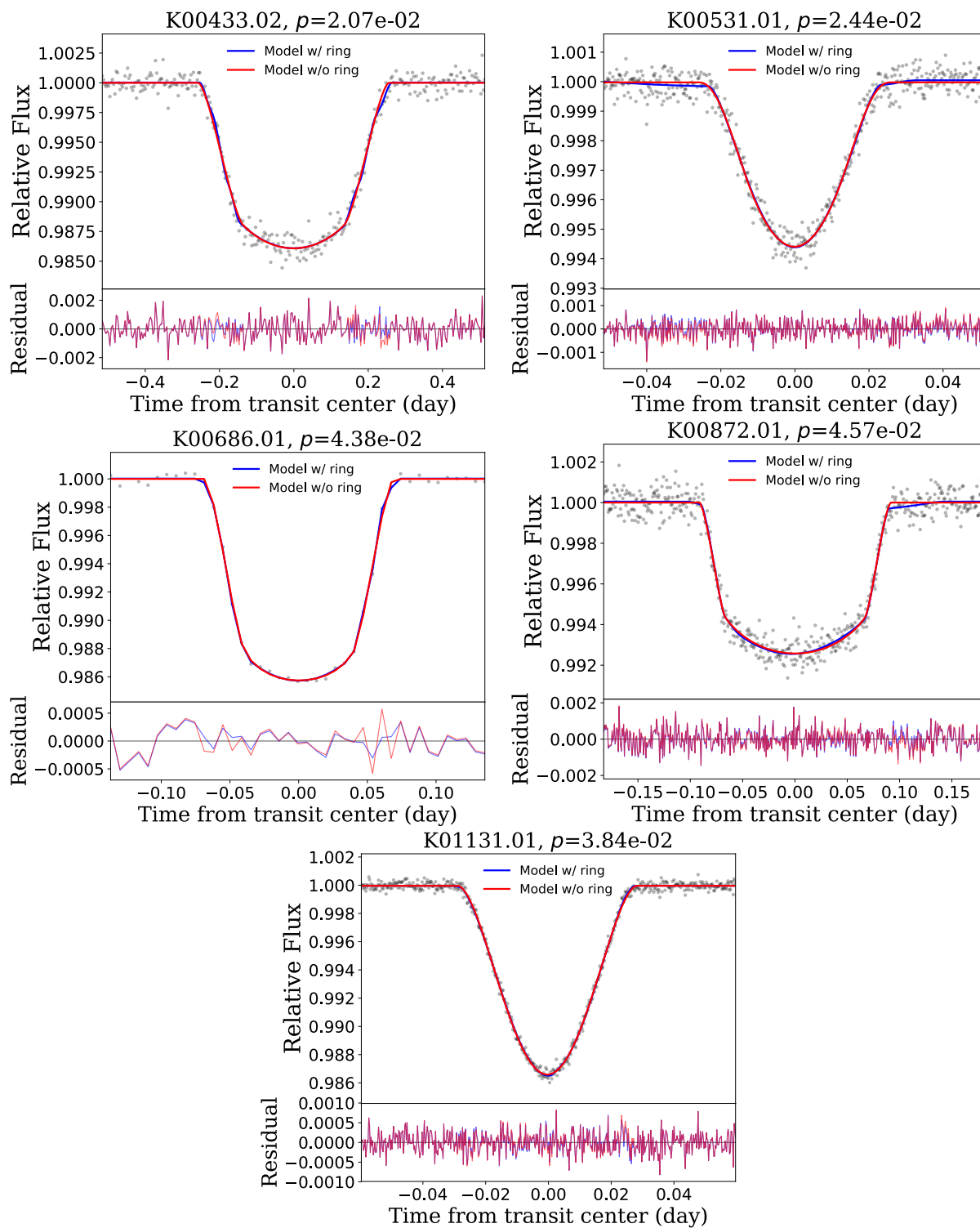
3.3.2.6   The remaining systems: KOI-12.01, 868.01, and 971.01

Finally, we consider the remaining three systems that have not been discussed.

The lightcurve of KOI-12.01 (*Kepler*-448 b) shows anomalous features during the transit, which are significant during -0.03 days to 0.1 days with respect to the central transit epoch. We find that such large pulse-like signals appear also during out-of-transit. Thus they are likely due to stellar activities.

The lightcurves of KOI-971.01 (KIC 11180361) show strong stellar activities, which are typical for multiple star systems (Niemczura et al., 2015), and CFOP webpages also identify this system as false positive. Thus, the planetary rings are not origins of the signals.

The lightcurve of KOI-868.01 shows an anomaly during the egress, which is shown in the left panel of Figure 3.10 along with the best-fit models. The fit yields $\chi^2_{\rm ringless,\ min}/{\rm dof} = 202.0/190$, $\chi^2_{\rm ring,\ min}/{\rm dof} = 171.6/195$, and $p = 7.88 \times 10^{-6}$. The analysis based on the binned data supports a Neptune-sized ringed planet of an orbital period of 236 days. The best-fit ring model gives $\theta = 25.5 \pm 10.0°$, $\phi = 12.4 \pm 3.7°$, $T = 0.46 \pm 0.18$, $r_{\rm in/p} = 1.88 \pm 0.36$, and $r_{\rm out/in} = 1.63 \pm 0.43$. The radius ratio $R_{\rm p}/R_\star = 0.099 \pm 0.012$ gives $R_{\rm p}/R_{\rm J} = 0.63 \pm 0.08$ assuming the stellar radius $R_\star = 0.657^{+0.022}_{-0.032}\,R_\odot$. The non-vanishing obliquity is consistent with the long alignment timescale $t_{\rm damp} = 2.95$ Gyr.

In order to check the consistency of signals, we calculate the *p*-values for the two transits in the short-cadence data separately. As a result, we find $p = 0.76$ and 7.4e-07 for the first and second transits, respectively. Indeed as indicated in the right panel of Figure 3.10, the lightcurves at the first and second transits are systematically different. Therefore KOI-868.01 is unlikely to be a ringed planet. We do not understand the origin of the anomalies because there are only two transits, but suspect that temporal stellar activities or spot-crossing events are responsible.
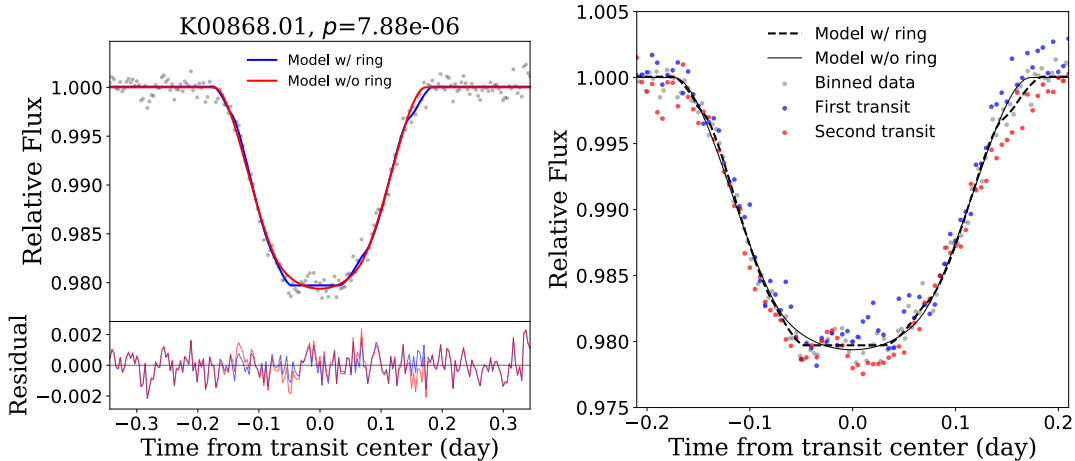
Figure 3.10 Lightcurves of KOI-868.01. Left panel indicates binned lightcurve (black circles) along wih the best-fits of the ringed and ringless models. Right panels shows the comparison for two different transits.

3.3.3 Upper Limits on the Ring Size

3.3.3.1 Result

Given the null detection, we derive upper limits on the outer radius of the possible ring following the method described in Sec 3.2.4. The resulting upper limits, $(R_{\mathrm{out}}/R_{\mathrm{p}})_{\mathrm{upp, Aligned}}$, $(R_{\mathrm{out}}/R_{\mathrm{p}})_{\mathrm{upp, Saturn}}$, and $(R_{\mathrm{out}}/R_{\star})_{\mathrm{upp}}$, are listed in Table 3.1 to 3.3. If we cannot obtain upper limits due to poor signal-to-noise ratios, we leave those values blank in the tables. The following discussions exclude 18 systems for $(R_{\mathrm{out}}/R_{\mathrm{p}})_{\mathrm{upp, Aligned}}$ and 7 systems for $(R_{\mathrm{out}}/R_{\mathrm{p}})_{\mathrm{upp, Saturn}}$ that are identified as possible false positives in the *Kepler* Community Follow-up Program (CFOP) webpage.[1]

Figure 3.11 compares upper limits $(R_{\mathrm{out}}/R_{\mathrm{p}})_{\mathrm{upp}}$ for the aligned and Saturn-like configurations against the physical planetary radii. The latter values are computed as $(R_{\mathrm{p}}/R_{\star})_{\mathrm{ringless}} \times R_{\star}$, where the values of $(R_{\mathrm{p}}/R_{\star})_{\mathrm{ringless}}$ are obtained from the ringless model and the stellar radii are taken from the Kepler catalog. Even assuming the ring aligned with the orbital plane, we find fairly tight limits on the ring size (several times R_{p}) for a few tens of systems.

Figure 3.12 is a similar plot to Figure 3.11, but against the equilibrium temperatures T_{eq} of the planets. The exhibited pattern does not reflect the physical dependence of $(R_{\mathrm{out}}/R_{\mathrm{p}})_{\mathrm{upp}}$ on T_{eq}, but simply comes from the fact that the hotter planets have shorter orbital periods, and hence larger signal-to-noise ratios of the phase-folded lightcurve. With sufficient signal-to-noise ratios for future data, however, such plots would provide interesting constraints on the physical properties of rings as a function of melting temperature of different compositions.

As mentioned in Section 3.3.1, the lightcurves of some of the 29 systems with $p < 0.05$ include contributions from the effects other than rings, such as gravity darkening and spot crossing. Nevertheless, we neglect them in deriving the upper limits on $R_{\mathrm{out}}/R_{\mathrm{p}}$. If we fit and remove those effects from the lightcurve, the upper limits may become more stringent. In this sense, the upper limits on $R_{\mathrm{out}}/R_{\mathrm{p}}$ listed in Tables 3.1 and 3.2 would be a bit conservative.

---

[1]https://exofop.ipac.caltech.edu/cfop.php
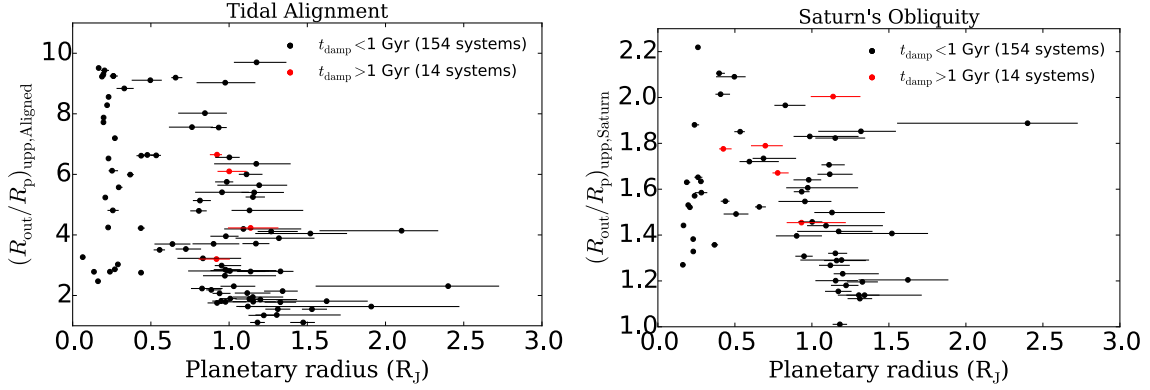
Figure 3.11 Upper limits on $R_{\mathrm{out}}/R_{\mathrm{p}}$ as a function of R_{p}. Left and right panels correspond to the tidally aligned ring, and a ring with Saturn's obliquity, respectively. Black points ($t_{\mathrm{damp}} < 1$ Gyr) are likely candidates for the aligned systems. The numbers of systems in panels count all targets with and without limits.
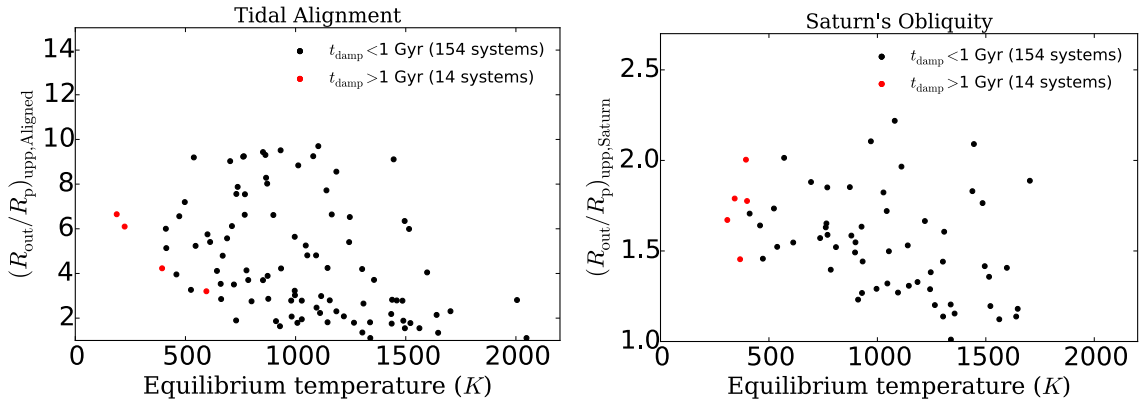
Figure 3.12 Same as Fig. 3.11, but plotted against the equilibrium temperature of the planets.

3.3.3.2   Comparison of Roche radius and upper limits

To understand implications of the upper limits physically, we compare the limits $(R_{\mathrm{out}}/R_{\mathrm{p}})_{\mathrm{upp}}$ with the Roche radii. If we consider ring formation by tidal destruction of incoming objects (e.g. satellites), the outer radius of the ring may be set by the Roche radius:

$$R_{\mathrm{out}} \sim 2.45 \, R_{\mathrm{p}} \left(\frac{\rho_{\mathrm{p}}}{\rho_{\mathrm{s}}} \right)^{1/3} = 1.6 \, R_{\mathrm{p}} \left(\frac{\rho_{\mathrm{p}}/1 \, \mathrm{g \, cm^{-3}}}{\rho_{\mathrm{s}}/3.5 \, \mathrm{g \, cm^{-3}}} \right)^{1/3}, \qquad (3.9)$$

where ρ_{p} is the planetary density and ρ_{s} is that of the incoming object. Here we scale the result using $\rho_{\mathrm{p}} = 1 \, \mathrm{g cm^{-3}}$ and $\rho_{\mathrm{s}} = 3.5 \, \mathrm{g cm^{-3}}$, which are the typical values for rocky components in the Solar System.

This implies that, if the inferred upper limit on the ring size $R_{\mathrm{out}}/R_{\mathrm{p}}$ is much smaller

than 1.6, the ring is unlikely to exist even inside that limit — unless ρ_s is unreasonably large. In our sample, six systems satisfy $t_{\mathrm{damp}} < 1\mathrm{Gyr}$ and $(R_{\mathrm{out}}/R_{\mathrm{p}})_{\mathrm{upp, \, Aligned}} < 1.6$, and one satisfies $t_{\mathrm{damp}} > 1\mathrm{Gyr}$ and $(R_{\mathrm{out}}/R_{\mathrm{p}})_{\mathrm{upp, \, Saturn}} < 1.6$. We may exclude possible rings around these systems.

3.3.4 Upper Limits on the Ring Occurrence

The above limits on $R_{\mathrm{out}}/R_{\mathrm{p}}$ translate into the the upper limit on the occurrence rate of rings $q[> x]$ as a function of $x \equiv R_{\mathrm{out}}/R_{\mathrm{p}}$. Here $q[> x]$ is the probability that a planet has a ring larger than x times the planetary radius. For example, $q[> x = 1]$ is simply the occurrence rate of rings, and $q[> x = 2]$ is that of rings larger than twice the planetary radii.

We attempt to estimate the upper limit on $q[> x]$ as follows. For a given value of x, consider n samples extracted from systems with $q[> x]$, for which the rings with $R_{\mathrm{out}}/R_{\mathrm{p}} > x$ should have been readily detectable — so this may be chosen to be $N[< x]$, the number of systems with $(R_{\mathrm{out}}/R_{\mathrm{p}})_{\mathrm{upp}} < x$. Then the probability that we detect n_{obs} rings with $R_{\mathrm{out}}/R_{\mathrm{p}} \geq x$ out of the n samples is given simply by the binominal distribution:

$$\mathrm{Prob}(n_{\mathrm{obs}}|q[> x], n) =_n C_{n_{\mathrm{obs}}} q[> x]^{n_{\mathrm{obs}}} (1 - q[> x])^{n - n_{\mathrm{obs}}}. \tag{3.10}$$

Without any prior knowledge of $q[> x]$ nor n_{obs}, we assume the uniform distribution for $\mathrm{Prob}(q[> x])$ and $\mathrm{Prob}(n_{\mathrm{obs}})$ with proper normalizations:

$$\int_0^1 \mathrm{Prob}\left(q[> x]|n\right) dq[> x] = 1 \rightarrow \quad \mathrm{Prob}\left(q[> x]|n\right) = 1 \tag{3.11}$$

$$\sum_{n_{\mathrm{obs}}=0}^n \mathrm{Prob}(n_{\mathrm{obs}}|n) = 1 \rightarrow \mathrm{Prob}(n_{\mathrm{obs}}|n) = 1/(n + 1) \tag{3.12}$$

According to Bayes' theorem, we obtain

$$\mathrm{Prob}(q[> x]|n_{\mathrm{obs}} = 0, n) = \frac{\mathrm{Prob}(q[> x]|n)\mathrm{Prob}(n_{\mathrm{obs}} = 0|q[> x], n)}{\mathrm{Prob}(n_{\mathrm{obs}} = 0|n)}$$
$$= (n + 1)(1 - q[> x])^n \tag{3.13}$$

The corresponding cumulative distribution function for $q[> x]$ is given by:

$$\mathrm{CDF}(q[> x]) = 1 - (1 - q[> x])^{n+1}. \tag{3.14}$$

Here, we would like to obtain the 95% upper limits of $q[> x]$. Thus, the above equation gives

$$q[> x]_{\mathrm{upp}} = 1 - (0.05)^{\frac{1}{n+1}}. \tag{3.15}$$

Now, we substitute the values of $N[< x]$ plotted in Fig 3.12 into n, and obtain the upper limits of $q[> x]$ as a function of x.

Figure 3.13 shows $q[> x]_{\mathrm{upp}}$ using $N[< (R_{\mathrm{out}}/R_{\mathrm{p}})_{\mathrm{upp, \, Aligned}}]$, and $N[< (R_{\mathrm{out}}/R_{\mathrm{p}})_{\mathrm{upp, \, Saturn}}]$. Physically speaking, the limit $(R_{\mathrm{out}}/R_{\mathrm{p}})_{\mathrm{upp, \, Aligned}}$ is appropriate

only for systems with small values of t_{damp}, which have likely achieved tidal alignment. On the other hand, $(R_{\mathrm{out}}/R_{\mathrm{p}})_{\mathrm{upp, Saturn}}$ may be more relevant for those with large values of t_{damp}. Therefore, we distinguish the systems with $t_{\mathrm{damp}} < 1\,\mathrm{Gyr}$ and $t_{\mathrm{damp}} > 1\,\mathrm{Gyr}$ in the plot. The more relevant subset is shown with thick lines in each panel.
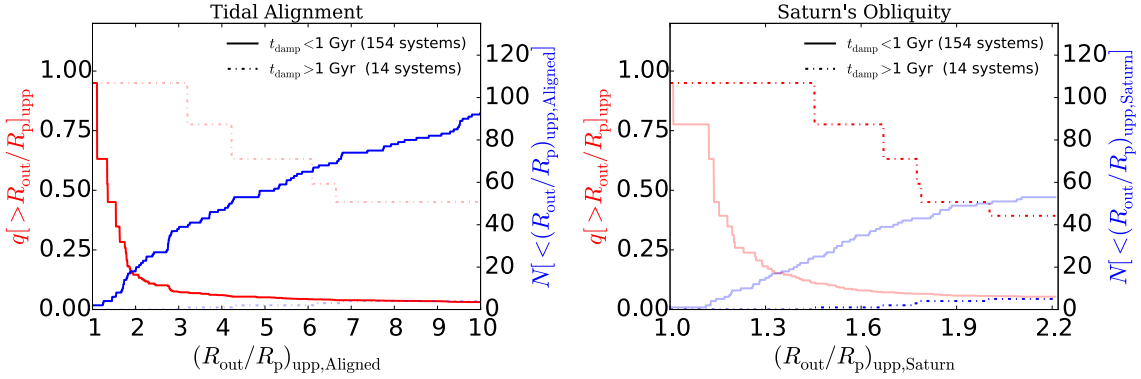
Figure 3.13 Cumulative frequency of upper limits $N[<(R_{\mathrm{out}}/R_{\mathrm{p}})_{\mathrm{upp}}]$ and upper imits on the occurence rate of rings $q[> x]_{\mathrm{upp}}$ in Eq (3.15). The left panel assumes the tidal alignment, while the right panel assumes the Saturn's obliquity. Thick lines in the left panel correspond to 154 systems with $t_{\mathrm{damp}} < 1\mathrm{Gyr}$, while those in the right panel to 14 systems with $t_{\mathrm{damp}} > 1\mathrm{Gyr}$.

3.4   Summary

We have performed a systematic and intensive search for exo-rings among the 168 *Kepler* planet candidates. The targets are homogeneously selected from all the KOIs that have the signal-to-noise ratio of the phase-folded lightcurves exceeding 100. As a result, a majority of our targets are short-period planets. This sample is complementary to that of long-period planets analyzed by Aizawa et al. (2017), and significantly larger than the 21 short-period planet samples by Heising et al. (2015).

For all the targets, we obtained the best-fit ringless and ringed model parameters from their individual phase-folded lightcurves following Aizawa et al. (2017). Then, we compare the two best-fits, and we select 29 systems as tentative candidates for which the ringed-model fit better explained the data than the ringless-model fit.

Those 29 systems are further examined individually and visually, and we conclude that none of them exhibits clear signature of a planetary ring. Instead, we derive upper limits on the ratio of the outer radius of the possible ring and the planetary radius assuming two different configurations; the tidally aligned ring and the Saturn's ring. The derived upper limits for individual systems are summarized in Tables 3.1 to 3.3.

The distribution of those upper limits can be used to derive the statistical upper limits on the occurrence rate of planetary rings as a function of $R_{\mathrm{out}}/R_{\mathrm{p}}$. We found that $\mathrm{Prob}(R_{\mathrm{out}}/R_{\mathrm{p}} > 2)$ should be less than 15 percent for tidally aligned ring systems.

Given that our targets are mainly in close-in orbits, the null detection of rings may not be so surprising (e.g. Schlichting & Chang, 2011). This is also consistent with the fact that dense planetary rings in our Solar System are discovered exclusively at temperatures close to 70 K (Hedman, 2015).

Nevertheless, our current result clearly indicates that the existing *Kepler* data are already accurate and precise enough to probe the planetary rings of a comparable size to the planet itself. This is quite encouraging, and the future effort towards the discovery of ring would likely be rewarding as we have witnessed numerous unexpected surprises in the history of astronomy, and especially exoplanetary science.

We also believe that the current methodology and examples of false-positives would be very useful in such future searches for planetary rings with improved datasets.

Having said so, it is important to emphasize other independent approaches to the ring survey. For instance, Zuluaga et al. (2015) pointed out that KOIs flagged as "FALSE POSITIVES", which we intentionally exclude from our current targets, may be promising because they could include possible ringed planets that are misinterpreted as anomalously large planets. Also a precession of planetary rings may induce a detectable level of transit depth variation (e.g. Carter & Winn, 2010; Heising et al., 2015). In addition, scattering and diffraction of the star light by the ring particles may be observable depending on the size of ring particles, especially through multi-band photometry in space.

Therefore, we expect that the upcoming observations with TESS and PLATO will substantially improve the observational searches for and understanding of the exoplanetary rings combined with the current result of the *Kepler* data.

Table 3.1: Parameters and statistics of 13 systems with $p < 0.001$

KOI	*Kepler*	P_{orb}^1 (day)	t_{damp} (Gyr)	$(R_{\mathrm{out}}/R_{\mathrm{p}})_{\mathrm{upp,\ Aligned}}$	$(R_{\mathrm{p}}/R_\star)_{\mathrm{ringless}}$	p	$(\chi^2_{\mathrm{ringless,min}}, \chi^2_{\mathrm{ring,min}}, N_{\mathrm{bin}})$	(S/N)	Comment[2]
2.01	2 b	2.20	2.60e-05	1.11	$0.07755 \pm$ 2e-05	5.02e-07	(534.22, 494.94, 500)	4357.03	GD
3.01	3 b	4.89	8.76e-04	2.75	$0.05886 \pm$ 3e-05	2.60e-09	(2011.23, 1820.95, 500)	2403.33	Spot
13.01	13 b	1.76	7.92e-06	1.63	$0.064683 \pm$ 4e-06	<1e-10	(8830.73, 5904.78, 500)	6359.84	GD
63.01	63 b	9.43	5.18e-03	2.44	$0.06481 \pm$ 4e-05	<1e-10	(1222.04, 1078.89, 500)	732.29	Spot
102.01	-	1.74	7.01e-05	5.51	$0.02810 \pm$ 6e-05	9.78e-05	(554.11, 525.66, 500)	432.74	Bad Fold
676.01	210 c	7.97	5.35e-03	7.20	$0.0520 \pm$ 5e-04	2.00e-10	(693.78, 620.69, 500)	302.61	Spot
868.01	-	236.00	2.95e+01	6.65	$0.144 \pm$ 1e-03	7.88e-06	(202.04, 171.63, 203)	182.23	Others
971.01	-	0.53	9.00e-10	8.13	$0.1 \pm$ 1e+00	3.54e-04	(319.16, 304.58, 500)	257.01	FP & Others
1416.01	840 b	2.50	3.55e-05	1.74	$0.1459 \pm$ 2e-04	5.14e-04	(579.31, 553.80, 500)	919.15	FP & Spot
1539.01	-	2.82	1.20e-05	1.10	$0.2568 \pm$ 2e-04	<1e-10	(982.31, 791.58, 500)	1364.17	FP & Spot
1714.01	-	2.74	5.29e-06	1.10	$0.17618 \pm$ 2e-05	<1e-10	(6978.85, 2755.22, 500)	688.33	FP & Spot
1729.01	-	5.20	2.88e-04	1.80	$0.1764 \pm$ 3e-04	<1e-10	(688.30, 610.78, 500)	816.17	FP & Spot
3794.01	1520 b	0.65	3.27e-07	-	$0.101 \pm$ 3e-03	2.37e-06	(678.22, 632.70, 500)	265.86	Evap

[1]Values from *Kepler* Object of Interest (KOI) Catalog Q1-Q17 DR 25(https://exoplanetarchive.ipac.caltech.edu/)

[2]FP=Possible False Positive (https://exofop.ipac.caltech.edu/cfop.php); GD = Gravity Darkening (B.1); Evap = Evaporating planet (B.2); Spot=Spot Crossing (B.3); Bad Fold = incorrect data folding (B.4); Small = non-significant signal (B.5); Others = B.6;

Table 3.2: Parameters and statistics of 16 systems with $0.001 < p < 0.05$

KOI	*Kepler*	P^1_{orb} (day)	t_{damp} (Gyr)	$(R_{\mathrm{out}}/R_{\mathrm{p}})_{\mathrm{upp, Aligned}}$	$(R_{\mathrm{out}}/R_{\mathrm{p}})_{\mathrm{upp, Saturn}}$	$(R_{\mathrm{out}}/R_{\star})_{\mathrm{upp}}$	$(R_{\mathrm{p}}/R_{\star})_{\mathrm{ringless}}$	p	$(\chi^2_{\mathrm{ringless,min}}, \chi^2_{\mathrm{ring,min}}, N_{\mathrm{bin}})$	(S/N)	Comment[2]
4.01	-	3.85	1.76e-04	-	-	-	$0.0394 \pm$ 3e-04	3.44e-02	(538.39, 525.32, 500)	148.29	FP & Small
5.01	-	4.78	6.05e-04	-	-	-	$0.04 \pm$ 1e-02	3.15e-02	(481.35, 469.45, 500)	455.35	FP & Small
12.01	448 b	17.86	1.44e-02	1.86	1.23	0.107	$0.09018 \pm$ 5e-05	1.23e-02	(548.57, 532.47, 500)	792.22	Others
70.02	20 b	3.70	1.23e-03	2.47	1.27	0.022	$0.01799 \pm$ 9e-05	1.34e-03	(671.05, 644.41, 500)	128.93	Bad Fold
148.01	48 b	4.78	2.46e-03	9.51	1.44	0.026	$0.0196 \pm$ 1e-04	1.13e-02	(663.02, 643.29, 500)	102.75	Bad Fold
212.01	-	5.70	1.04e-03	-	1.72	0.093	$0.0649 \pm$ 3e-04	2.14e-02	(525.10, 511.11, 500)	159.08	Small
214.01	424 b	3.31	1.46e-04	2.99	-	-	$0.104 \pm$ 3e-03	2.37e-02	(446.95, 435.27, 500)	448.51	Small
257.01	506 b	6.88	5.14e-03	9.25	2.22	0.033	$0.0224 \pm$ 2e-04	3.84e-02	(550.10, 537.05, 500)	161.18	Small
423.01	39 b	21.09	2.12e-02	3.89	1.85	0.129	$0.0890 \pm$ 6e-04	1.66e-02	(500.13, 486.18, 500)	225.79	Small
433.02	553 c	328.24	7.94e+01	6.10	-	-	$0.120 \pm$ 7e-03	2.07e-02	(250.09, 238.97, 303)	112.04	Small
531.01	-	3.69	2.97e-04	-	-	-	$0.096 \pm$ 4e-03	2.44e-02	(469.53, 457.33, 500)	183.64	Small
686.01	-	52.51	3.36e-01	4.68	-	-	$0.118 \pm$ 4e-03	4.38e-02	(46.09, 31.21, 40)	153.64	FP & Small
872.01	46 b	33.60	1.36e-01	-	-	-	$0.084 \pm$ 2e-03	4.57e-02	(486.30, 475.20, 500)	173.00	Small
1131.01	-	0.70	2.08e-07	1.02	1.02	0.211	$0.2 \pm$ 7e-02	3.84e-02	(549.24, 536.21, 500)	727.17	FP & Small
1353.01	289 c	125.87	4.46e+00	4.23	2.00	0.153	$0.1048 \pm$ 6e-04	9.04e-03	(544.28, 525.28, 442)	198.14	Spot
6016.01	-	4.55	7.76e-05	1.32	1.65	0.463	$0.23 \pm$ 2e-02	9.91e-03	(503.24, 487.04, 472)	1719.88	FP & Spot

---

[1]Values from *Kepler* Object of Interest (KOI) Catalog Q1-Q17 DR 25(https://exoplanetarchive.ipac.caltech.edu/)

[2]FP=Possible False Positive (https://exofop.ipac.caltech.edu/cfop.php); GD = Gravity Darkening (B.1); Evap = Evaporating planet (B.2); Spot=Spot Crossing (B.3); Bad Fold = incorrect data folding (B.4); Small = non-significant signal (B.5); Others = B.6;

Table 3.3: Parameters and statistics of 139 systems with $p > 0.05$

KOI	Kepler	P_{orb}^1 (day)	t_{damp} (Gyr)	$(R_{\mathrm{out}}/R_{\mathrm{p}})_{\mathrm{upp,\,Aligned}}$	$(R_{\mathrm{out}}/R_{\mathrm{p}})_{\mathrm{upp,\,Saturn}}$	$(R_{\mathrm{out}}/R_{\star})_{\mathrm{upp}}$	$(R_{\mathrm{p}}/R_{\star})_{\mathrm{ringless}}$	p	$(\chi^2_{\mathrm{ringless,min}}, \chi^2_{\mathrm{ring,min}}, N_{\mathrm{bin}})$	(S/N)	Comment[2]
1.01	1 b	2.47	4.20e-05	1.11	1.01	0.127	$0.1259 \pm 7\mathrm{e}{-04}$	1.00e+00	(511.76, 511.76, 500)	9353.67	-
7.01	4 b	3.21	3.42e-04	5.99	1.36	0.031	$0.02445 \pm 7\mathrm{e}{-05}$	3.41e-01	(572.68, 566.10, 500)	284.12	-
10.01	8 b	3.52	1.11e-04	1.78	1.20	0.109	$0.0940 \pm 4\mathrm{e}{-04}$	7.51e-01	(491.06, 488.39, 500)	1565.89	-
17.01	6 b	3.23	9.43e-05	3.71	1.15	0.105	$0.0932 \pm 1\mathrm{e}{-04}$	3.60e-01	(456.00, 450.92, 500)	2671.28	-
18.01	5 b	3.55	1.12e-04	2.14	1.14	0.088	$0.0790 \pm 1\mathrm{e}{-04}$	1.36e-01	(482.37, 474.17, 500)	2054.24	-
20.01	12 b	4.44	1.69e-04	1.81	1.20	0.138	$0.1179 \pm 1\mathrm{e}{-04}$	4.81e-01	(583.61, 578.28, 500)	3127.91	-
22.01	422 b	7.89	1.34e-03	1.95	1.82	0.135	$0.0956 \pm 2\mathrm{e}{-04}$	1.33e-01	(473.51, 465.41, 500)	1886.93	-
42.01	410 A b	17.83	9.29e-02	8.28	-	-	$0.0169 \pm 2\mathrm{e}{-04}$	1.00e+00	(484.28, 484.20, 500)	144.80	-
46.01	101 b	3.49	3.06e-04	9.11	2.09	0.048	$0.0320 \pm 2\mathrm{e}{-04}$	2.20e-01	(451.10, 444.68, 500)	152.32	-
64.01	-	1.95	2.93e-05	2.81	-	-	$0.04 \pm 1\mathrm{e}{-02}$	1.45e-01	(532.93, 524.06, 500)	286.21	-
69.01	93 b	4.73	2.94e-03	2.78	-	-	$0.0157 \pm 2\mathrm{e}{-04}$	1.00e+00	(525.95, 526.55, 500)	265.72	-
70.01	20 c	10.85	1.62e-02	9.25	1.65	0.040	$0.0289 \pm 1\mathrm{e}{-04}$	6.40e-01	(482.40, 479.07, 500)	225.66	-
75.01	-	105.88	3.63e+00	3.20	-	-	$0.0378 \pm 2\mathrm{e}{-04}$	7.06e-01	(575.70, 572.23, 500)	208.26	-
82.01	102 e	16.15	6.07e-02	5.24	-	-	$0.0289 \pm 5\mathrm{e}{-04}$	9.92e-01	(516.92, 516.39, 500)	248.53	-
84.01	19 b	9.29	1.50e-02	9.23	1.63	0.033	$0.02376 \pm 9\mathrm{e}{-05}$	8.74e-01	(490.32, 488.50, 500)	220.22	-
85.01	65 c	5.86	3.38e-03	6.53	1.38	0.021	$0.01652 \pm 5\mathrm{e}{-05}$	4.95e-01	(553.43, 548.49, 500)	191.04	-
94.01	89 d	22.34	3.70e-02	3.71	1.40	0.089	$0.0695 \pm 2\mathrm{e}{-04}$	3.25e-01	(492.67, 486.86, 500)	858.57	-
94.02	89 c	10.42	1.20e-02	8.84	-	-	$0.0255 \pm 1\mathrm{e}{-04}$	7.58e-01	(548.33, 545.41, 500)	165.65	-
94.03	89 e	54.32	8.66e-01	-	-	-	$0.0409 \pm 5\mathrm{e}{-04}$	4.59e-01	(480.16, 475.61, 500)	201.68	-
97.01	7 b	4.89	2.53e-04	1.55	-	-	$0.0823 \pm 1\mathrm{e}{-04}$	3.32e-01	(518.47, 512.42, 500)	1580.40	-
98.01	14 b	6.79	1.21e-03	2.18	-	-	$0.0455 \pm 1\mathrm{e}{-04}$	6.91e-01	(518.91, 515.68, 500)	588.69	-
100.01	-	9.97	2.14e-03	-	-	-	$0.055 \pm 3\mathrm{e}{-03}$	7.82e-01	(541.86, 539.14, 500)	188.32	-
103.01	-	14.91	4.75e-02	-	1.88	0.040	$0.0271 \pm 2\mathrm{e}{-04}$	5.61e-01	(458.09, 454.44, 500)	114.38	-
104.01	94 b	2.51	1.93e-04	3.03	-	-	$0.0390 \pm 7\mathrm{e}{-04}$	8.64e-01	(520.19, 518.18, 500)	276.45	-
105.01	463 b	8.98	8.95e-03	-	1.58	0.041	$0.0300 \pm 2\mathrm{e}{-04}$	3.57e-01	(535.74, 529.75, 500)	175.89	-
108.01	103 b	15.97	4.70e-02	-	-	-	$0.0212 \pm 5\mathrm{e}{-04}$	7.25e-02	(507.09, 496.74, 500)	109.94	-
108.02	103 c	179.61	3.21e+01	-	-	-	$0.0335 \pm 7\mathrm{e}{-04}$	9.73e-01	(538.74, 537.79, 500)	118.02	-

[1]Values from *Kepler* Object of Interest (KOI) Catalog Q1-Q17 DR 25(https://exoplanetarchive.ipac.caltech.edu/)

[2]FP=Possible False Positive (https://exofop.ipac.caltech.edu/cfop.php); GD = Gravity Darkening (B.1); Evap = Evaporating planet (B.2); Spot=Spot Crossing (B.3); Bad Fold = incorrect data folding (B.4); Small = non-significant signal (B.5); Others = B.6;

KOI	*Kepler*	$P_{\rm orb}$ (day)	$t_{\rm damp}$ (Gyr)	$(R_{\rm out}/R_{\rm p})_{\rm upp,\ Aligned}$	$(R_{\rm out}/R_{\rm p})_{\rm upp,\ Saturn}$	$(R_{\rm out}/R_{\star})_{\rm upp}$	$(R_{\rm p}/R_{\star})_{\rm ringless}$	p	$(\chi^2_{\rm ringless,min},\ \chi^2_{\rm ring,min},\ N_{\rm bin})$	(S/N)	Comment
111.01	104 b	11.43	2.53e-02	9.43	-	-	$0.0208 \pm 6\text{e-}04$	9.95e-01	(482.47, 482.07, 500)	149.05	-
111.02	104 c	23.67	2.16e-01	-	-	-	$0.0205 \pm 7\text{e-}04$	1.00e+00	(507.95, 508.06, 500)	102.89	-
111.03	104 d	51.76	1.86e+00	-	-	-	$0.0230 \pm 2\text{e-}04$	6.83e-01	(506.56, 503.35, 500)	104.53	-
115.01	105 b	5.41	2.21e-03	4.81	-	-	$0.0243 \pm 5\text{e-}04$	1.00e+00	(533.29, 534.26, 500)	164.82	-
119.01	108 b	49.18	4.74e-01	4.79	-	-	$0.0403 \pm 5\text{e-}04$	7.28e-01	(443.98, 441.43, 500)	146.21	-
122.01	95 b	11.52	1.92e-02	-	1.63	0.028	$0.0203 \pm 1\text{e-}04$	3.48e-01	(612.05, 605.09, 500)	124.25	-
123.01	109 b	6.48	4.52e-03	4.25	-	-	$0.0179 \pm 4\text{e-}04$	9.59e-01	(567.41, 566.21, 500)	104.11	-
125.01	468 b	38.48	1.24e-01	6.66	1.21	0.165	$0.1396 \pm 5\text{e-}04$	1.71e-01	(539.81, 531.35, 500)	586.79	FP
127.01	77 b	3.58	1.58e-04	1.81	1.31	0.120	$0.0981 \pm 3\text{e-}04$	5.86e-01	(497.21, 493.42, 500)	970.07	-
128.01	15 b	4.94	3.96e-04	1.79	-	-	$0.1026 \pm 5\text{e-}04$	2.50e-01	(474.56, 468.17, 500)	1113.76	-
129.01	470 b	24.67	4.53e-04	2.78	1.76	0.114	$0.0805 \pm 4\text{e-}04$	4.45e-01	(485.79, 481.08, 500)	211.74	-
130.01	-	34.19	5.36e-02	2.95	-	-	$0.1142 \pm 7\text{e-}04$	6.75e-02	(457.67, 448.15, 500)	785.48	FP
131.01	471 b	5.01	4.38e-04	2.65	1.61	0.105	$0.0765 \pm 4\text{e-}04$	2.37e-01	(453.50, 447.26, 500)	333.34	FP
135.01	43 b	3.02	8.54e-05	1.88	-	-	$0.0855 \pm 2\text{e-}04$	3.59e-01	(442.14, 437.21, 500)	1246.59	-
137.01	18 c	7.64	3.37e-03	6.62	1.55	0.058	$0.0426 \pm 1\text{e-}04$	9.21e-01	(485.86, 484.43, 500)	425.15	-
137.02	18 d	14.86	1.90e-02	3.51	-	-	$0.0541 \pm 5\text{e-}04$	4.42e-01	(460.59, 456.11, 500)	444.75	-
139.01	111 c	224.78	4.17e+01	-	-	-	$0.053 \pm 1\text{e-}03$	2.45e-01	(471.58, 465.18, 500)	127.91	-
141.01	-	2.62	1.38e-04	6.64	-	-	$0.055 \pm 2\text{e-}03$	1.83e-01	(570.48, 561.75, 500)	325.66	-
143.01	-	22.65	5.32e-02	7.41	-	-	$0.06 \pm 2\text{e-}02$	9.99e-01	(479.24, 479.01, 500)	115.81	FP
144.01	472 b	4.18	9.22e-04	2.86	-	-	$0.0357 \pm 8\text{e-}04$	9.96e-01	(512.22, 511.84, 500)	206.94	-
148.02	48 c	9.67	1.31e-02	-	1.57	0.038	$0.0280 \pm 2\text{e-}04$	2.60e-01	(509.73, 503.01, 500)	153.76	-
149.01	473 b	14.56	2.67e-02	-	-	-	$0.0286 \pm 2\text{e-}04$	9.36e-01	(530.61, 529.21, 500)	105.77	-
150.01	112 b	8.41	1.03e-02	-	1.52	0.035	$0.0263 \pm 2\text{e-}04$	6.78e-02	(512.70, 502.05, 500)	108.37	-
152.01	79 d	52.09	6.40e-01	-	-	-	$0.0506 \pm 6\text{e-}04$	2.86e-01	(462.65, 456.81, 500)	166.31	-
153.01	113 c	8.93	1.12e-02	-	-	-	$0.031 \pm 1\text{e-}03$	9.01e-01	(494.06, 492.45, 500)	132.84	-
153.02	113 b	4.75	2.13e-03	-	-	-	$0.0254 \pm 7\text{e-}04$	9.98e-01	(595.02, 594.71, 500)	136.46	-
156.03	114 d	11.78	2.74e-02	-	-	-	$0.035 \pm 1\text{e-}03$	4.26e-01	(504.95, 499.90, 500)	156.89	-
157.01	11 c	13.02	2.93e-02	-	-	-	$0.0253 \pm 3\text{e-}04$	6.32e-01	(495.87, 492.40, 500)	120.27	-
157.02	11 d	22.69	1.32e-01	-	-	-	$0.0275 \pm 3\text{e-}04$	9.20e-01	(485.51, 484.09, 500)	121.48	-
157.03	11 e	32.00	2.72e-01	-	-	-	$0.0381 \pm 7\text{e-}04$	5.94e-01	(535.66, 531.63, 500)	131.42	-
161.01	475 b	3.11	4.52e-04	2.78	-	-	$0.0309 \pm 7\text{e-}04$	9.80e-01	(525.60, 524.80, 500)	173.70	-
182.01	-	3.48	1.15e-04	1.61	1.17	0.154	$0.1359 \pm 3\text{e-}04$	9.56e-01	(532.88, 531.71, 500)	907.22	FP

KOI	*Kepler*	P_{orb} (day)	t_{damp} (Gyr)	$(R_{\mathrm{out}}/R_{\mathrm{p}})_{\mathrm{upp, Aligned}}$	$(R_{\mathrm{out}}/R_{\mathrm{p}})_{\mathrm{upp, Saturn}}$	$(R_{\mathrm{out}}/R_{\star})_{\mathrm{upp}}$	$(R_{\mathrm{p}}/R_{\star})_{\mathrm{ringless}}$	p	$(\chi^2_{\mathrm{ringless,min}}, \chi^2_{\mathrm{ring,min}}, N_{\mathrm{bin}})$	(S/N)	Comment
183.01	423 b	2.68	5.46e-05	1.79	1.20	0.144	$0.1240 \pm$ 2e-04	7.58e-01	(531.38, 528.53, 500)	1927.67	-
186.01	485 b	3.24	9.44e-05	5.40	1.29	0.145	$0.1177 \pm$ 5e-04	7.09e-02	(463.20, 453.68, 500)	907.61	-
188.01	425 b	3.80	1.89e-04	2.07	-	-	$0.1137 \pm$ 8e-04	6.82e-01	(505.55, 502.34, 500)	763.67	-
189.01	486 b	30.36	7.40e-02	3.96	1.64	0.182	$0.132 \pm$ 1e-03	8.43e-01	(491.38, 489.33, 500)	495.16	FP
191.01	487 b	15.36	1.05e-02	2.85	-	-	$0.1130 \pm$ 6e-04	1.93e-01	(498.81, 491.33, 500)	722.16	-
192.01	427 b	10.29	2.75e-03	5.64	1.29	0.110	$0.0892 \pm$ 2e-04	6.18e-01	(575.01, 570.87, 500)	577.13	-
194.01	488 b	3.12	7.67e-05	1.36	1.14	0.145	$0.1346 \pm$ 4e-04	4.36e-01	(557.03, 551.56, 500)	894.33	-
195.01	426 b	3.22	1.05e-04	2.31	-	-	$0.117 \pm$ 1e-03	7.15e-01	(510.76, 507.73, 500)	806.33	-
196.01	41 b	1.86	2.41e-05	1.75	-	-	$0.1001 \pm$ 5e-04	8.59e-02	(567.27, 556.20, 500)	932.49	-
197.01	489 b	17.28	2.22e-02	9.19	1.52	0.124	$0.0916 \pm$ 8e-04	9.92e-02	(495.08, 485.81, 500)	370.23	-
199.01	490 b	3.27	7.58e-05	4.05	1.41	0.120	$0.0923 \pm$ 4e-04	7.36e-01	(506.74, 503.88, 500)	652.81	-
200.01	74 b	7.34	9.60e-04	2.80	-	-	$0.0911 \pm$ 7e-04	8.52e-01	(514.93, 512.85, 500)	430.98	-
201.01	491 b	4.23	3.04e-04	2.23	1.97	0.116	$0.0806 \pm$ 5e-04	8.58e-01	(441.44, 439.70, 500)	657.38	-
202.01	412 b	1.72	1.46e-05	1.34	1.18	0.117	$0.103 \pm$ 2e-03	7.27e-01	(448.69, 446.11, 500)	895.88	-
203.01	17 b	1.49	8.41e-06	1.55	1.12	0.146	$0.1323 \pm$ 1e-04	4.32e-01	(619.80, 613.66, 500)	3014.03	-
204.01	44 b	3.25	1.03e-04	2.79	-	-	$0.0802 \pm$ 8e-04	9.14e-02	(527.39, 517.27, 500)	348.47	-
205.01	492 b	11.72	6.63e-03	3.53	-	-	$0.097 \pm$ 1e-03	2.29e-01	(522.98, 515.67, 500)	369.77	-
206.01	433 b	5.33	4.32e-04	6.35	1.42	0.082	$0.0633 \pm$ 4e-04	6.08e-01	(533.62, 529.71, 500)	257.22	-
208.01	493 b	3.00	9.31e-05	2.82	1.83	0.125	$0.0865 \pm$ 5e-04	7.29e-01	(568.67, 565.42, 500)	202.89	-
209.01	117 c	50.79	3.85e-01	5.41	1.55	0.094	$0.0698 \pm$ 4e-04	7.41e-01	(510.66, 507.82, 500)	358.63	-
209.02	117 b	18.80	3.14e-02	3.70	-	-	$0.0466 \pm$ 5e-04	2.40e-01	(471.61, 465.15, 500)	237.63	-
217.01	71 b	3.91	1.60e-04	5.25	1.32	0.166	$0.1334 \pm$ 5e-04	2.44e-01	(564.36, 556.70, 500)	1059.21	-
229.01	497 b	3.57	3.05e-04	-	-	-	$0.0505 \pm$ 5e-04	2.48e-01	(486.02, 479.46, 500)	117.38	-
232.01	122 c	12.47	1.25e-02	-	1.49	0.059	$0.0438 \pm$ 2e-04	5.17e-01	(469.98, 465.94, 500)	269.24	-
244.01	25 c	12.72	1.63e-02	4.23	-	-	$0.03561 \pm$ 9e-05	2.16e-01	(522.14, 514.67, 500)	429.53	-
244.02	25 b	6.24	4.08e-03	8.56	1.33	0.023	$0.01875 \pm$ 6e-05	5.76e-01	(459.81, 456.24, 500)	223.07	-
245.01	37 d	39.79	1.17e+00	-	-	-	$0.0227 \pm$ 3e-04	9.98e-01	(504.20, 503.92, 500)	154.71	-
246.01	68 A b	5.40	3.05e-03	7.72	1.53	0.023	$0.01688 \pm$ 4e-05	1.00e+00	(490.53, 498.47, 500)	249.46	-
250.01	26 b	12.28	2.19e-02	-	-	-	$0.0480 \pm$ 5e-04	1.18e-01	(468.86, 460.52, 500)	108.72	-
251.01	125 b	4.16	1.03e-03	-	-	-	$0.0450 \pm$ 9e-04	9.99e-01	(522.41, 522.17, 500)	136.30	-
254.01	45 b	2.46	4.52e-05	1.90	-	-	$0.1821 \pm$ 9e-04	8.35e-01	(481.66, 479.60, 500)	1514.84	-
261.01	96 b	16.24	5.82e-02	6.12	-	-	$0.0261 \pm$ 4e-04	3.23e-01	(532.12, 525.82, 500)	153.96	-

KOI	*Kepler*	P_orb (day)	t_damp (Gyr)	$(R_\mathrm{out}/R_\mathrm{p})_\mathrm{upp,\,Aligned}$	$(R_\mathrm{out}/R_\mathrm{p})_\mathrm{upp,\,Saturn}$	$(R_\mathrm{out}/R_\star)_\mathrm{upp}$	$(R_\mathrm{p}/R_\star)_\mathrm{ringless}$	p	$(\chi^2_\mathrm{ringless,min}, \chi^2_\mathrm{ring,min}, N_\mathrm{bin})$	(S/N)	Comment
277.01	36 c	16.23	4.68e-02	-	-	-	$0.0207 \pm$ 1e-04	9.86e-01	(527.45, 526.75, 500)	139.68	-
279.01	450 b	28.45	1.32e-01	6.63	1.85	0.050	$0.0349 \pm$ 2e-04	6.91e-01	(531.31, 528.00, 500)	206.16	-
280.01	-	11.87	2.98e-02	9.31	-	-	$0.0194 \pm$ 2e-04	8.24e-01	(527.11, 524.77, 500)	126.35	-
282.01	130 c	27.51	2.56e-01	-	-	-	$0.0236 \pm$ 7e-04	3.94e-01	(475.67, 470.66, 500)	111.58	-
304.01	518 b	8.51	1.15e-02	-	-	-	$0.0228 \pm$ 2e-04	1.00e+00	(489.96, 490.58, 500)	108.97	-
314.01	138 c	13.78	6.55e-02	-	-	-	$0.0249 \pm$ 8e-04	1.00e+00	(448.61, 448.73, 500)	113.40	-
319.01	-	46.15	3.17e-01	9.03	-	-	$0.051 \pm$ 9e-03	2.25e-01	(523.15, 515.79, 500)	137.89	-
351.02	90 g	210.60	3.43e+01	-	1.79	0.087	$0.0597 \pm$ 4e-04	8.91e-02	(383.31, 374.62, 427)	111.28	-
366.01	-	75.11	4.79e-01	4.14	-	-	$0.064 \pm$ 2e-03	5.33e-01	(375.88, 371.57, 367)	172.90	-
367.01	-	31.58	2.35e-01	-	2.01	0.062	$0.0422 \pm$ 6e-04	6.63e-01	(284.44, 281.38, 310)	192.72	-
398.01	148 d	51.85	4.65e-01	5.14	-	-	$0.100 \pm$ 3e-03	3.18e-01	(493.58, 487.69, 500)	184.33	-
433.01	553 b	4.03	5.57e-04	-	2.11	0.071	$0.0478 \pm$ 4e-04	9.36e-01	(494.54, 493.24, 500)	129.83	-
464.01	561 b	58.36	8.60e-01	-	-	-	$0.068 \pm$ 1e-03	4.90e-01	(461.90, 457.74, 500)	174.35	-
611.01	-	3.25	1.32e-04	-	-	-	$0.11 \pm$ 4e-02	3.84e-01	(413.93, 409.50, 500)	405.50	-
620.01	51 b	45.16	3.75e-01	-	1.73	0.104	$0.0725 \pm$ 5e-04	8.62e-01	(525.96, 523.91, 500)	120.00	-
620.02	51 d	130.18	5.87e+00	-	1.45	0.131	$0.0985 \pm$ 7e-04	5.02e-01	(288.97, 284.74, 305)	130.48	-
631.01	628 b	15.46	1.39e-02	8.02	-	-	$0.0617 \pm$ 8e-04	9.62e-01	(123.10, 121.88, 111)	120.26	-
674.01	643 b	16.34	1.44e-02	-	-	-	$0.0369 \pm$ 3e-04	9.16e-01	(454.41, 453.04, 500)	137.26	-
676.02	210 b	2.45	2.53e-04	7.88	-	-	$0.0381 \pm$ 6e-04	5.62e-01	(483.27, 479.43, 500)	265.21	-
680.01	435 b	8.60	4.84e-04	2.31	1.89	0.090	$0.0630 \pm$ 3e-04	9.78e-01	(504.98, 504.17, 500)	468.57	-
760.01	-	4.96	3.50e-04	9.70	-	-	$0.112 \pm$ 3e-03	2.52e-01	(123.17, 117.00, 139)	179.87	-
767.01	670 b	2.82	6.55e-05	2.08	1.67	0.166	$0.1200 \pm$ 6e-04	5.49e-01	(451.94, 448.26, 500)	922.58	-
802.01	-	19.62	1.70e-02	4.11	-	-	$0.144 \pm$ 1e-03	9.55e-01	(407.32, 406.22, 414)	239.43	-
806.01	30 d	143.21	8.97e+00	-	1.67	0.131	$0.0922 \pm$ 8e-04	4.28e-01	(472.50, 467.79, 500)	108.09	-
806.02	30 c	60.32	5.04e-01	6.00	1.71	0.188	$0.132 \pm$ 2e-03	6.64e-01	(484.77, 481.58, 500)	305.49	-
824.01	693 b	15.38	1.02e-02	5.75	-	-	$0.121 \pm$ 2e-03	5.43e-01	(506.00, 501.84, 500)	122.79	-
834.01	238 e	23.65	5.62e-02	7.56	-	-	$0.057 \pm$ 1e-03	3.56e-01	(502.90, 497.27, 500)	162.09	-
841.02	27 c	31.33	1.47e-01	-	-	-	$0.066 \pm$ 2e-03	7.20e-01	(502.77, 499.83, 500)	107.50	-
880.02	82 c	51.54	7.77e-01	-	-	-	$0.056 \pm$ 2e-03	1.00e+00	(488.24, 488.50, 500)	118.13	-
883.01	-	2.69	5.44e-05	1.64	1.27	0.217	$0.1800 \pm$ 8e-04	7.14e-02	(493.31, 483.20, 500)	1462.56	-
884.01	247 c	9.44	7.18e-03	-	-	-	$0.0492 \pm$ 4e-04	4.71e-01	(473.11, 468.71, 500)	159.90	-
889.01	75 b	8.88	2.19e-03	7.55	1.59	0.160	$0.114 \pm$ 2e-03	4.02e-01	(517.30, 511.93, 500)	329.94	-

KOI	Kepler	$P_{\rm orb}$ (day)	$t_{\rm damp}$ (Gyr)	$(R_{\rm out}/R_{\rm p})_{\rm upp, Aligned}$	$(R_{\rm out}/R_{\rm p})_{\rm upp, Saturn}$	$(R_{\rm out}/R_\star)_{\rm upp}$	$(R_{\rm p}/R_\star)_{\rm ringless}$	p	$(\chi^2_{\rm ringless,min}, \chi^2_{\rm ring,min}, N_{\rm bin})$	(S/N)	Comment
918.01	725 b	39.64	1.66e-01	6.56	1.46	0.151	0.1143 ± 8e-04	5.62e-01	(544.34, 540.01, 500)	373.56	-
959.01	-	12.71	2.50e-02	2.12	1.96	0.260	0.179 ± 1e-03	8.41e-01	(92.72, 89.28, 65)	1216.12	FP
961.01	42 b	1.21	9.26e-05	3.27	-	-	0.0446 ± 3e-04	9.61e-01	(743.83, 742.28, 500)	107.21	-
984.01	-	4.29	1.41e-03	-	-	-	0.031 ± 3e-03	2.26e-01	(995.18, 981.19, 500)	180.30	-
1074.01	762 b	3.77	1.62e-04	4.20	1.44	0.137	0.1043 ± 4e-04	8.08e-02	(568.08, 556.81, 500)	439.51	-
1089.01	418 b	86.68	1.92e+00	-	-	-	0.083 ± 2e-03	7.55e-01	(475.60, 473.04, 500)	145.85	-
1426.02	297 c	74.93	1.98e+00	-	-	-	0.0632 ± 9e-04	6.60e-01	(392.61, 389.30, 395)	119.29	-
1448.01	-	2.49	1.50e-05	1.68	1.27	0.230	0.1894 ± 4e-04	6.96e-01	(657.90, 653.84, 500)	1137.21	FP
1456.01	855 b	7.89	1.93e-03	3.23	-	-	0.0754 ± 6e-04	5.40e-01	(504.84, 500.66, 500)	226.00	-
1474.01	419 b	69.73	8.96e-01	-	-	-	0.0633 ± 7e-04	3.72e-01	(458.00, 452.46, 453)	185.06	-
1478.01	858 b	76.14	2.86e+00	-	1.78	0.070	0.0489 ± 2e-04	2.39e-01	(400.00, 392.79, 382)	122.21	-
1545.01	-	5.91	5.65e-04	4.81	1.50	0.162	0.1212 ± 9e-04	5.52e-01	(506.69, 502.59, 500)	318.66	-
1547.01	-	30.69	6.38e-02	-	-	-	0.126 ± 2e-03	2.09e-01	(166.69, 157.65, 139)	110.46	-
1781.01	411 c	7.83	5.03e-03	5.57	-	-	0.0420 ± 6e-04	7.47e-01	(515.99, 513.16, 500)	173.86	-
1784.01	-	5.01	5.19e-04	8.43	-	-	0.3 ± 4e+01	3.61e-01	(558.13, 551.92, 500)	210.08	FP
6969.01	-	1.79	2.44e-06	1.13	1.02	0.242	0.2368 ± 3e-04	3.13e-01	(527.82, 521.46, 500)	2074.42	FP

Chapter 4

Observational Quest for Alignment of Disk Orientations in Nearby Star-Forming Regions: Orion, Lupus, Taurus, Upper Scorpius, and ρ Ophiuchi

The related paper is under peer review.

Chapter 5

Global Mapping of an Exo-Earth using Sparse Modeling

The related paper is under peer review.

Chapter 6

Summary and Future Prospects

6.1 Summary

In this thesis, we focus on observational aspects of exoplanetary and stellar systems by exploiting current (ALMA and Kepler) and future instruments (LUVOIR and HabEx). The significant findings and attempts in each chapter are summarized as follows:

Chapter 3

- We intensively search for exoplanetary rings around the 168 Kepler planets, whose light curves would allow the detection of Saturn-like rings. Most of planets have short orbital periods, and the expected composition of ring particles is rock rather than ice. In this sense, this search is complementary to the previous search around long-period planets (Aizawa et al., 2017), and significantly improved over the previous search around short-period planets (Heising et al., 2015).

- Although we identify 29 tentative systems, where the ring model is statistically preferred over the ringless model, none of the signatures turn out to be robust after inspecting the light curves in detail. These false positives (e.g. stellar spots, evaporating planets) are useful for the future search for rings.

- The null results put upper limits on the size of possible rings, and using the sets of constraints, we demonstrate that the occurrence rate of exoplanetary rings larger than twice the planetary radius should be less than 15 %. Although the majority of planets are very different from the Solar System, our search provides the quantitative constraint on the ring formation and evolution in exoplanetary systems.

Chapter 4

- We systematically search for the evidence of alignment of proto-planetary disks in five nearby star-forming regions. In the analyses, we mostly exploit the ALMA observations of them to determine their geometry.

- We find that PA distributions are well described by the uniform distribution in four regions other than Lupus region, and this is basically consistent with the turbulent nature of angular momentum. On the other hand, we identify the possible signature of the alignment in the Lupus III at the statistical significance of 2σ, and it might imply other mechanisms for generating angular momentum beyond turbulent motions.

- We also confirm the robustness of observed disk geometries in the Lupus region by comparing different methods for extracting disk's geometry (CLEAN+imfit, uvmodelfit, and sparse modeling). Although the sparse modeling significantly resolves the substructures of disks, it does not give the significant improvement on the estimations of position angles and inclinations compared with other methods.

- We find the alignment among disks in the Orion Nebular Cluster, but it turns to be likely a false positive after inspecting details of calibrations for the interferometric observations. Specifically, the systematic errors in the observation make disk images stretched in a certain direction so that the apparent alignment is produced. This effect becomes significant for marginally resolved disks, and it should be carefully addressed for the robust discussion of the alignment.

Chapter 5

- We propose to exploit a sparse modeling in global mapping of an Earth analog from its scattered light curves. We find that the sparse modeling potentially recovers the better resolved map than the Tikhonov regularization in case of the cloudless Earth. We also apply the sparse modeling to the real scattered light curves of the Earth, and we demonstrate that the method can separate the the Australian continent and the South American continent, which cannot be resolved in the reconstructed map using Tikhonov regularization.

- We also attempt to recover the surface map from noise-injected light curves by assuming an Earth analog at a distance of 10 pc. We find that the multi-epoch observation for 1 day per month can reconstruct the main surfaces of an Earth analog in future direct imaging missions such as HabEx or LUVOIR. This demonstrates the feasibility of global mapping in realistic situations with limited observational duration.

The methodology of search for rings presented in Chapter 3 will be applicable to other observations including TESS (Transiting Exoplanet Survey Satellite). The constraint on the ring frequency gives a quantitative information on ring formation complementary to the knowledge in the Solar System. In Chapter 4, we find that disk orientations are likely to be random in four regions out of five, and it is consistent with the turbulent nature of angular momentum. On the other hand, we find the possible alignment in the Lupus III at 2σ level, and it might require mechanism beyond turbulence. Additionally, we find the apparent alignment in ONC, but it is likely to be a false positive due to systematical noises. On the other hand, we demonstrate that the sparse modeling is potentially

useful in global mapping of an Earth analog in the future observations in Chapter 5. Furthermore, we show that intermittent observations even with a cadence of one month allow the global mapping assuming a planet at a distance of 10 pc.

Chapter 4 and Chapter 5 have the connection to each other in viewpoints of the application of the sparse modeling, and the further studies would be rewarding. In addition, Chapter 3 and Chapter 5 commonly present the methodologies for identifying Solar-System counterparts in the exoplanetary systems: exorings and exosurfaces. Additionally, all of chapters attempt to give new light on the architectures of exoplanets: planetary spins and alignment among planetary systems and/or proto-planetary disks. They are complementary to previous discussions on spin-orbit misalignment, and will give unique information of planetary formation. In summary, the works in this thesis present previous unconventional viewpoints, and they will be helpful for further understanding of origin, formation, and evolution of planetary systems including the Solar System.

6.2 Future Prospects

Finally, we briefly discuss the possible future directions for each topic addressed in this thesis: search for planetary rings in the future, investigation into alignment among disks or cores and its implication, and further application of sparse modeling in astronomy.

6.2.1 Search for exoplanetary rings using transit method in the future

We have intensively searched for planetary rings using the Kepler data, so the next possible direction would be exploitation of other data including TESS, which basically observes the full sky. The promising targets for the ring search would be cold long-period planets like Saturn, but the short-period planets would be also be valuable to be explored if rocky rings generally exist. The typical observational duration of the TESS is one month, so the main targets in the ring search would be short-period planets with possible rocky rings. On the other hand, the particular sectors have been observed for more than one month, so it is still promising to search for icy rings around long-period planets.

Long-period planets can be also identified in long baselines achieved by combinations of current and future photometric observations including Kepler, TESS, CHaracterizing ExOPlanets Satellite (CHEOPS), and PLAnetary Transits and Oscillations of stars (PLATO). Recently, the collaboration of the Kepler mission and TESS has yielded the detection of Jupiter-sized planet HIP41378 f with $P = 542$ days (Santerne et al., 2019), and this demonstrates the feasibility of the method in the future.

In addition, a ring significantly increases the apparent size of the planet, and this leads to the underestimation of planetary density, which can be the indirect evidence of the ring system (Zuluaga et al., 2015). In reality, there is a class of the extremely low dense super Earth planets, so called Supper Puffs, and they might be explained by the ringed planets rather than the single planet (Piro & Vissapragada, 2019). Another interesting

example is HIP41378 f with the extremely small density (0.09 ± 0.02 g cm^{-3}), and it can be explained by the ringed planet (Santerne et al., 2019). The small planetary density is the just the indirect evidence of the possible ringed planet, and additional analyses and observations are necessary to prove or reject the ring hypothesis. One way is to search for the anomalies in light curves caused by rings as investigated in this thesis, although it requires the exquisite photometric precision. Another way is to exploit multi-band observations of transit light curves, whose shapes potentially change depending on wavelength due to chromatic scattering and absorption by ring particles (e.g. Barnes & Fortney, 2004). Especially, the exoplanets discovered by TESS are comparatively close to the Earth, so it practically allows for the follow-up observations of transit light curves in other telescopes.

6.2.2 Exploration of alignment of disks and cores and its implication

In Chapter 4, we explore the disk-disk alignment by exploiting previous observations and literature, but as demonstrated in Section 4.5, the marginally resolved disks are susceptible to systematic noises, which can produce the apparent alignment. To evade such false positive, it will be useful to implement a simulation for systematical observations of proto-planetary disks with help of the CASA task `simalma` (McMullin et al., 2007) so that we can quantify to what extent we can recover the possible alignment from the noisy observation. Such attempts can be also essential for determining correct size of disks in systematical survey. On the other hand, the current ALMA data for ONC used in this thesis is largely susceptible to observational errors, and the additional observation will be essential for investigating the region further.

We can also extend the disk alignment to that among molecular cloud cores in star-forming regions. The rotational axes of stellar cores can be constrained by the measurements of Doppler shifts of the molecular lines (e.g. N$_2$H$^+$), and we can naturally apply our methodology to their estimated directions of rotations. Previously, Tatematsu et al. (2016) gave estimations of directions of axes of angular momentums for 34 dark cores in Orion A cloud, whose average mass of cores is $45.7 M_\odot$ (Tatematsu et al., 2008). They implicitly pointed out that the core orientations in the upper cloud are preferentially directed toward the east direction, which is still inconsistent with the global rotation of the cloud. We can similarly pursue the alignment among cores by exploiting several searches for cores in previous literature (Caselli et al., 2002; Pirogov et al., 2003; Chen et al., 2007; Tobin et al., 2011; Tatematsu et al., 2016; Chen et al., 2019), and such studies would be complementary to our current work.

On the other hand, the origin and implication of the alignment are still unknown, and the further exploration is rewarding. One possibility is a global rotation of a molecular cloud (Corsaro et al., 2017; Kuznetsova et al., 2019), but we do not find the large rotation in Lupus III. We are now analyzing the simulation data presented by Chen & Ostriker (2015), which tracked the core formation and evolution in the colliding convergent flows in molecular clouds. Their simulations consider magnetic fields, which are ignored in

previous studies, so the results are complementary to the previous studies. We will report the results in the future.

6.2.3 Further application of sparse modeling

In this thesis, we explore the possibility of the sparse modeling in imaging of proto-planetary disks and global mapping of an Earth analog in future direct imaging observations. Beyond these attempts, further application and extension are rewarding. One natural application of sparse modeling would be identification of sub-structures of proto-planetary disks by exploiting the better effective angular resolution achieved the method. The structures of interest include the gap structures (e.g. ALMA Partnership et al., 2015), spiral structures (e.g. Pérez et al., 2016), bright arcs (e.g. Pérez et al., 2018), and misaignment in warped disks (e.g. Sakai et al., 2019). The typical enhancement of the angular resolution by sparse modeling is a few times (e.g. Honma et al., 2014), and the reanalyses of the data will potentially reveal the hidden structures of disks in existing data.

We can also extend usage of the sparse modeling to mapping of stellar spots on stellar surfaces. Periodic variations in light curves can be due to the apparent motions of stellar spots by the stellar rotations, and we can inversely solve the distributions of spots from the variations (e.g Walker et al., 2007). Stellar spots can be assumed to have zero luminosity in the estimation, we can naturally apply the sparse modeling to the light curves for the inference. Such attempts would also constrain not only the properties of stellar spots but also the stellar inclinations of stars, which are important for characterizing the planetary architectures as well.

In addition to the mapping of stellar spots, the methods for global mapping can be also improved in several points. The introduced regularization in this thesis is not unique, and one can also attempt other combinations, including L1, L2, TSV, and Total Variation (TV) terms, to search for optimal regularization terms. In choosing the optimal regularization parameters for the sparse modeling in the future observations, we suppose that we train the parameters by injecting and recovering different models as in Event Horizon Telescope Collaboration et al. (2019), but one might be able to extend the *l*-curve method to the three dimensional space (e.g surface curvature). One can also improve the method for global mapping to reconstruct a 2d "color" map of the exoplanetary surface from multi-band observations. Previously, Fujii et al. (2017) pointed out that there exist the degeneracy between surface types and their spatial distributions, but one can also exploit some regularization terms to suppress the number of surface types for solving the degeneracy. In the real scattered light curves, the clouds can be significant sources of systematic noises in mapping, so the methods for handling them should be seriously explored. In summary, it will be rewarding to pursue the complete methodology for recovering the 2d map of a colored Earth assuming the future observations.

Acknowledgement

First of all, I wish to express my sincere gratitude to my supervisor, Yasushi Suto, for his continuous support and encouragement. He directly or sometimes indirectly has taught me about a lot things: open-mindedness, how to choose research topics, how to survive the tough times, skills of critical thinking, and how to take balance between details and big pictures. In addition, he always took the precious time to give me advices whenever I wanted, and gave me a lot opportunities to deepen and expand the researches in various ways. These experiences and skills will be useful and encouraging for the rest of my life in a broad sense, not limited to the research.

I was also fortunate to collaborate with Hajime Kawahara, whose attitude toward science always stimulated me in various ways. The discussion with him was simply enjoyable and insightful, and it definitely broadened my perspective a lot. Working with him, I also realized that collaboration with others from different backgrounds are essentially important in pursuing good researches. I would also like to thank Kento Masuda for his insight advices and comments. The most important thing I learned from him is the importance of being and behaving professional, which significantly has affected my view of researches. Furthermore, I want to show my gratitude to Kashiyama Kazumi for his continuous supports in various respects. I was always overwhelmed by his broad knowledge. Through the discussion with him, I unconsciously has got familiar with a lot of topics, which definitely expanded my possibility. He also listened to me and gave me appropriate advices when I was worried about the future.

I would also like to show my gratitude to my collaborators, Yoko Oya, Shiro Ikeda, Takeshi Nakazato, Siteng Fan, and Tomoyuki Tajiri for their professional knowledge, comments, and discussions. Woking with them, I directly learned the importance of discussing with people beyond one's field. In addition, I would like to thank Kenta Hotokezaka and Kento Masuda for their warm welcome during my stay at Princeton. The conversations with them helped me envision the future of my life. Furthermore, I would like to show my special thanks to Ryoma Murata for his encouragement and supports.

Additionally, I would like to show my gratitude to my thesis committee, Profs. Kipp Cannon, Ryohei Kawabe, Hideyuki Tagoshi, Toru Yamada, and Satoshi Yamamoto for their constructive comments and encouragements. Particularly, I am very grateful to Ryohei Kawabe for discussion on data analyses of interferometric observations in Chapter 4.

My gratitude definitely goes to all (ex-)members in Theoretical Astrophysical Group

(UTAP)/Research Center of Early Universe (RESCEU). I thank people in our exoplanet group, Kazuhiro Kanagawa, Yuta Nakagawa, Toshinori Hayashi, Shijie Wang, and Lu Yuting for discussions and sharing time in the weekly meeting. In addition, I would also like to show my special thanks to Sunmyon Chon, Shoya Kamiaka, Riouhei Nakatani, Ken Osato, and Taizo Okabe for giving me advices and sharing the precious time. I was also fortunate to enjoy the life within and beyond the research thanks to Yuta Nakagawa, Akinari Hamabada, Leo Tsukada, and Kojiro Kawana.

---

[1]http://www.astropy.org

Bibliography

ALMA Partnership et al., 2015, The Astrophysical Journal Letters, 808, L3

Agol E., Jansen T., Lacy B., Robinson T. D., Meadows V., 2015, The Astrophysical Journal, 812, 5

Aizawa M., Uehara S., Masuda K., Kawahara H., Suto Y., 2017, The Astronomical Journal, 153, 193

Akinsanmi B., Oshagh M., Santos N. C., Barros S. C. C., 2018, Astronomy & Astrophysics, 609, A21

Akiyama K., et al., 2017a, The Astronomical Journal, 153, 159

Akiyama K., et al., 2017b, The Astrophysical Journal, 838, 1

Andrews S. M., Wilner D. J., Hughes A. M., Qi C., Dullemond C. P., 2010, The Astrophysical Journal, 723, 1241

Ansdell M., et al., 2016, The Astrophysical Journal, 828, 46

Arnold L., Schneider J., 2004, Astronomy & Astrophysics, 420, 1153

Astropy Collaboration et al., 2013, Astronomy & Astrophysics, 558, A33

Astropy Collaboration et al., 2018, The Astronomical Journal, 156, 123

Barenfeld S. A., Carpenter J. M., Ricci L., Isella A., 2016, The Astrophysical Journal, 827, 142

Barnes J. W., Fortney J. J., 2004, The Astrophysical Journal, 616, 1193

Barnes J. W., Linscott E., Shporer A., 2011, The Astrophysical Journal Supplement Series, 197, 10

Belloche A., 2013, in Hennebelle P., Charbonnel C., eds, EAS Publications Series Vol. 62, EAS Publications Series. pp 25–66 (`arXiv:1305.0627`), doi:10.1051/eas/1362002

Bennett D. P., et al., 2014, The Astrophysical Journal, 785, 155

Brown T. M., Charbonneau D., Gilliland R. L., Noyes R. W., Burrows A., 2001, The Astrophysical Journal, 552, 699

Carter J. A., Winn J. N., 2010, The Astrophysical Journal, 709, 1219

Carter J. A., et al., 2012, Science, 337, 556

Caselli P., Benson P. J., Myers P. C., Tafalla M., 2002, The Astrophysical Journal, 572, 238

Chen C.-Y., Ostriker E. C., 2015, The Astrophysical Journal, 810, 126

Chen C.-Y., Ostriker E. C., 2018, The Astrophysical Journal, 865, 34

Chen X., Launhardt R., Henning T., 2007, The Astrophysical Journal, 669, 1058

Chen H. H.-H., et al., 2019, The Astrophysical Journal, 886, 119

Cieza L. A., et al., 2019, Monthly Notices of the Royal Astronomical Society, 482, 698

Corsaro E., et al., 2017, Nature Astronomy, 1, 0064

Cossou C., Raymond S. N., Hersant F., Pierens A., 2014, Astronomy & Astrophysics, 569, A56

Cowan N. B., et al., 2009, The Astrophysical Journal, 700, 915

Dawson R. I., Chiang E., 2014, Science, 346, 212

Dawson R. I., Johnson J. A., 2018, Annual Review of Astronomy and Astrophysics, 56, 175

Dawson R. I., Murray-Clay R. A., Johnson J. A., 2015, The Astrophysical Journal, 798, 66

Dib S., Hennebelle P., Pineda J. E., Csengeri T., Bontemps S., Audit E., Goodman A. A., 2010, The Astrophysical Journal, 723, 425

Dyudina U. A., Sackett P. D., Bayliss D. D. R., Seager S., Porco C. C., Throop H. B., Dones L., 2005, The Astrophysical Journal, 618, 973

Eisner J. A., et al., 2018, The Astrophysical Journal, 860, 77

Event Horizon Telescope Collaboration et al., 2019, The Astrophysical Journal Letters, 875, L4

Fan S., Li C., Li J.-Z., Bartlett S., Jiang J. H., Natraj V., Crisp D., Yung Y. L., 2019, The Astrophysical Journal Letters, 882, L1

Fleck R. C. J., Clark F. O., 1981, The Astrophysical Journal, 245, 898

Ford E. B., Seager S., Turner E. L., 2001, Nature, 412, 885

Foreman-Mackey D., Morton T. D., Hogg D. W., Agol E., Schölkopf B., 2016, The Astronomical Journal, 152, 206

Fujii Y., Kawahara H., 2012, The Astrophysical Journal, 755, 101

Fujii Y., Kawahara H., Suto Y., Taruya A., Fukuda S., Nakajima T., Turner E. L., 2010, The Astrophysical Journal, 715, 866

Fujii Y., Kawahara H., Suto Y., Fukuda S., Nakajima T., Livengood T. A., Turner E. L., 2011, The Astrophysical Journal, 738, 184

Fujii Y., Lustig-Yaeger J., Cowan N. B., 2017, The Astronomical Journal, 154, 189

Gaudi B. S., et al., 2008, Science, 319, 927

Goodman A. A., Benson P. J., Fuller G. A., Myers P. C., 1993, The Astrophysical Journal, 406, 528

Hansen P. C., 2010, Discrete inverse problems: insight and algorithms. Siam

Hedman M. M., 2015, The Astrophysical Journal Letters, 801, L33

Heising M. Z., Marcy G. W., Schlichting H. E., 2015, The Astrophysical Journal, 814, 81

Heller R., Rodenbeck K., Bruno G., 2019, Astronomy & Astrophysics, 624, A95

Heyer M. H., Brunt C. M., 2004, The Astrophysical Journal Letters, 615, L45

Honma M., Akiyama K., Uemura M., Ikeda S., 2014, Publications of the Astronomical Society of Japan, 66, 95

Hsu D. C., Ford E. B., Ragozzine D., Ashby K., 2019, The Astronomical Journal, 158, 109

Ikeda S., Tazaki F., Akiyama K., Hada K., Honma M., 2016, Publications of the Astronomical Society of Japan, 68, 45

Isella A., Carpenter J. M., Sargent A. I., 2009, The Astrophysical Journal, 701, 260

Jackson R. J., Jeffries R. D., 2010, Monthly Notices of the Royal Astronomical Society, 402, 1380

Jackson R. J., Deliyannis C. P., Jeffries R. D., 2018, Monthly Notices of the Royal Astronomical Society, 476, 3245

Jenkins J. M., et al., 2015, The Astronomical Journal, 150, 56

Kamiaka S., Benomar O., Suto Y., 2018, Monthly Notices of the Royal Astronomical Society, 479, 391

Kawahara H., 2016, The Astrophysical Journal, 822, 112

Kawahara H., Fujii Y., 2011, The Astrophysical Journal Letters, 739, L62

Kawahara H., Masuda K., 2019, The Astronomical Journal, 157, 218

Kipping D. M., 2009a, Monthly Notices of the Royal Astronomical Society, 392, 181

Kipping D. M., 2009b, Monthly Notices of the Royal Astronomical Society, 396, 1797

Kipping D. M., 2013, Monthly Notices of the Royal Astronomical Society, 435, 2152

Kipping D. M., Bakos G. Á., Buchhave L., Nesvorný D., Schmitt A., 2012, The Astrophysical Journal, 750, 115

Kolmogorov A., 1941a, Akademiia Nauk SSSR Doklady, 30, 301

Kolmogorov A. N., 1941b, Akademiia Nauk SSSR Doklady, 32, 16

Kovacs G., 2018, Astronomy & Astrophysics, 612, L2

Kreidberg L., Luger R., Bedell M., 2019, The Astrophysical Journal Letters, 877, L15

Kuramochi K., Akiyama K., Ikeda S., Tazaki F., Fish V. L., Pu H.-Y., Asada K., Honma M., 2018, The Astrophysical Journal, 858, 56

Kuznetsova A., Hartmann L., Heitsch F., 2019, The Astrophysical Journal, 876, 33

Larson R. B., 1981, Monthly Notices of the Royal Astronomical Society, 194, 809

Lecavelier des Etangs A., et al., 2017, Astronomy & Astrophysics, 603, A115

Lee E. J., Chiang E., 2016, The Astrophysical Journal, 817, 90

Lee E. J., Chiang E., Ormel C. W., 2014, The Astrophysical Journal, 797, 95

Li P. S., Norman M. L., Mac Low M.-M., Heitsch F., 2004, The Astrophysical Journal, 605, 800

Lissauer J. J., et al., 2011, Nature, 470, 53

Macintosh B., et al., 2014, Proceedings of the National Academy of Science, 111, 12661

Mandel K., Agol E., 2002, The Astrophysical Journal Letters, 580, L171

Markwardt C. B., 2009, Non-linear Least-squares Fitting in IDL with MPFIT. p. 251

Masuda K., 2014, The Astrophysical Journal, 783, 53

Masuda K., 2015, The Astrophysical Journal, 805, 28

Mayor M., Queloz D., 1995, Nature, 378, 355

McMullin J. P., Waters B., Schiebel D., Young W., Golap K., 2007, CASA Architecture and Applications. p. 127

Mosser B., Gehan C., Belkacem K., Samadi R., Michel E., Goupil M. J., 2018, Astronomy & Astrophysics, 618, A109

Mróz P., et al., 2017, Nature, 548, 183

Mullally F., Thompson S. E., Coughlin J. L., Burke C. J., Rowe J. F., 2018, The Astronomical Journal, 155, 210

Niemczura E., et al., 2015, Monthly Notices of the Royal Astronomical Society, 450, 2764

Ohashi N., Hayashi M., Ho P. T. P., Momose M., Tamura M., Hirano N., Sargent A. I., 1997, The Astrophysical Journal, 488, 317

Ohta Y., Taruya A., Suto Y., 2009, The Astrophysical Journal, 690, 1

Osborn H. P., et al., 2016, Monthly Notices of the Royal Astronomical Society, 457, 2273

Parviainen H., 2015, Monthly Notices of the Royal Astronomical Society, 450, 3233

Pérez L. M., et al., 2016, Science, 353, 1519

Pérez L. M., et al., 2018, The Astrophysical Journal Letters, 869, L50

Perryman M., Hartman J., Bakos G. Á., Lindegren L., 2014, The Astrophysical Journal, 797, 14

Pineda J. E., Zhao B., Schmiedeke A., Segura-Cox D. M., Caselli P., Myers P. C., Tobin J. J., Dunham M., 2019, The Astrophysical Journal, 882, 103

Piro A. L., Vissapragada S., 2019, arXiv e-prints, p. arXiv:1911.09673

Pirogov L., Zinchenko I., Caselli P., Johansson L. E. B., Myers P. C., 2003, Astronomy & Astrophysics, 405, 639

Protassov R., van Dyk D. A., Connors A., Kashyap V. L., Siemiginowska A., 2002, The Astrophysical Journal, 571, 545

Rafikov R. R., 2017, The Astrophysical Journal, 837, 163

Rappaport S., et al., 2012, The Astrophysical Journal, 752, 1

Raymond S. N., Cossou C., 2014, Monthly Notices of the Royal Astronomical Society, 440, L11

Rey-Raposo R., Read J. I., 2018, Monthly Notices of the Royal Astronomical Society, 481, L16

Robinson T. D., Meadows V. S., Crisp D., 2010, The Astrophysical Journal Letters, 721, L67

Sakai N., Hanawa T., Zhang Y., Higuchi A. E., Ohashi S., Oya Y., Yamamoto S., 2019, Nature, 565, 206

Sanchis-Ojeda R., Winn J. N., 2011, The Astrophysical Journal, 743, 61

Sanchis-Ojeda R., et al., 2013, The Astrophysical Journal, 775, 54

Santerne A., et al., 2019, arXiv e-prints, p. arXiv:1911.07355

Santos N. C., et al., 2015, Astronomy & Astrophysics, 583, A50

Schlichting H. E., Chang P., 2011, The Astrophysical Journal, 734, 117

Schmitt J. R., et al., 2014, The Astrophysical Journal, 795, 167

Schmitt J. R., Jenkins J. M., Fischer D. A., 2017, The Astronomical Journal, 153, 180

Simbulan C., Tamayo D., Petrovich C., Rein H., Murray N., 2017, Monthly Notices of the Royal Astronomical Society, 469, 3337

Simon M., Dutrey A., Guilloteau S., 2000, The Astrophysical Journal, 545, 1034

Sumi T., et al., 2011, Nature, 473, 349

Sumi T., et al., 2016, The Astrophysical Journal, 825, 112

Suzuki D., et al., 2016, The Astrophysical Journal, 833, 145

Tatematsu K., Kandori R., Umemoto T., Sekimoto Y., 2008, Publications of the Astronomical Society of Japan, 60, 407

Tatematsu K., Ohashi S., Sanhueza P., Nguyen Luong Q., Umemoto T., Mizuno N., 2016, Publications of the Astronomical Society of Japan, 68, 24

Teachey A., Kipping D. M., 2018, Science Advances, 4, eaav1784

Teachey A., Kipping D. M., Schmitt A. R., 2018, The Astronomical Journal, 155, 36

Thompson S. E., et al., 2018, The Astrophysical Journal Supplement Series, 235, 38

Tobin J. J., et al., 2011, The Astrophysical Journal, 740, 45

Uehara S., Kawahara H., Masuda K., Yamada S., Aizawa M., 2016, The Astrophysical Journal, 822, 2

Walker G. A. H., et al., 2007, The Astrophysical Journal, 659, 1611

Wang J., et al., 2015, The Astrophysical Journal, 815, 127

Weiss L. M., et al., 2013, The Astrophysical Journal, 768, 14

Williams J. P., Cieza L. A., 2011, Annual Review of Astronomy and Astrophysics, 49, 67

Wittenmyer R. A., Butler R. P., Wang L., Bergmann C., Salter G. S., Tinney C. G., Johnson J. A., 2016, Monthly Notices of the Royal Astronomical Society, 455, 1398

Wolszczan A., Frail D. A., 1992, Nature, 355, 145

Zhu W., Petrovich C., Wu Y., Dong S., Xie J., 2018, The Astrophysical Journal, 860, 101

Zuluaga J. I., Kipping D. M., Sucerquia M., Alvarado J. A., 2015, The Astrophysical Journal Letters, 803, L14